AD-A164 298 OPERATIONAL CHARACTERISTICS OF A HIGH VOLTAGE DENSE PLASMA FOCUS(U) NEW MEXICO UNIV ALBUQUERQUE DEPT OF CHEMICAL AND NUCLEAR ENGI D M WOODALL NOV 85 1/2

UNCLASSIFIED AFWL-TR-84-119 F29611-82-K-0075 F/G 20/9 NL

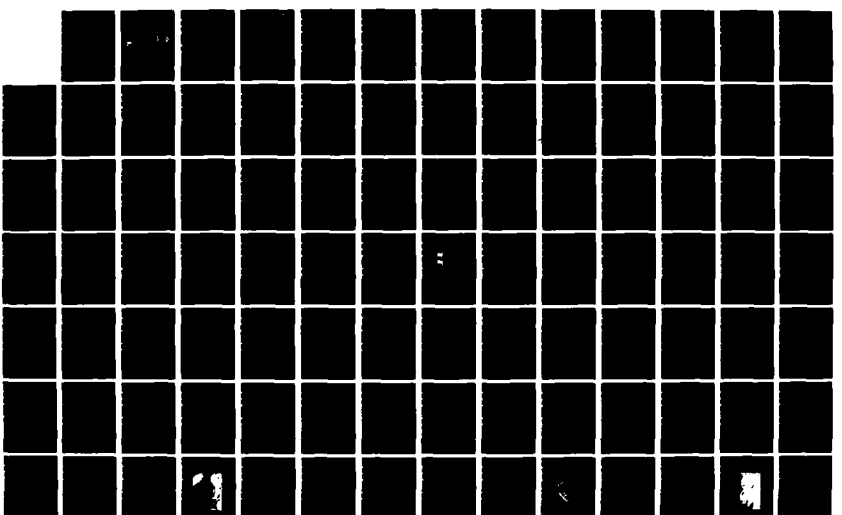

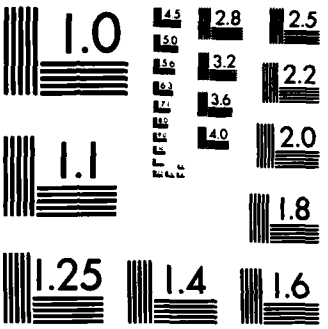


MICROCOPY RESOLUTION TEST CHART

NARDS-1963-A

AFWL-TR-
84-119

(2)



# OPERATIONAL CHARACTERISTICS OF A HIGH VOLTAGE DENSE PLASMA FOCUS

David M. Woodall

University of New Mexico
Dept of Chemical and Nuclear Engineering
Albuquerque, NM 87131



November 1985

Final Report





AIR FORCE WEAPONS LABORATORY
Air Force Systems Command
Kirtland Air Force Base, NM 87117-6008

This final report was prepared by the University of New Mexico, Albuquerque, New Mexico, under Contract F29601-82-K-0075, Job Order 88091719 with the Air Force Weapons Laboratory, Kirtland Air Force Base, New Mexico. First Lieutenant David J. Hall (AWPP) was the Laboratory Project Officer-in-Charge.



This report has been reviewed by the Public Affairs Office and is releasable to the National Technical Information Services (NTIS). At NTIS, it will be available to the general public, including foreign nations.

If your address has changed, if you wish to be removed from our mailing list, or if your organization no longer employs the addressee, please notify AFWL/AWPP, Kirtland AFB, NM 87117 to help us maintain a current mailing list.

This technical report has been reviewed and is approved for publication.

David J. Hall

DAVID J. HALL
First Lieutenant, USAF
Project Officer

FOR THE COMMANDER

William F. McCullough

WILLIAM F. MCCULLOUGH
Major, USAF
Chief, Plasma Physics Branch

William L. Baker

WILLIAM L. BAKER
Chief, Advanced Technology Division

---

DO NOT RETURN COPIES OF THIS REPORT UNLESS CONTRACTUAL OBLIGATIONS OR NOTICE ON A SPECIFIC DOCUMENT REQUIRES THAT IT BE RETURNED.

UNCLASSIFIED

SECURITY CLASSIFICATION OF THIS PAGE

AD-A164 298

## REPORT DOCUMENTATION PAGE

| | |
|---|---|
| 1a. REPORT SECURITY CLASSIFICATION: Unclassified | 1b. RESTRICTIVE MARKINGS |
| 2a. SECURITY CLASSIFICATION AUTHORITY | 3. DISTRIBUTION/AVAILABILITY OF REPORT: Approved for public release; distribution unlimited. |
| 2b. DECLASSIFICATION/DOWNGRADING SCHEDULE | |
| 4. PERFORMING ORGANIZATION REPORT NUMBER(S) | 5. MONITORING ORGANIZATION REPORT NUMBER(S): AFWL-TR-84-119 |
| 6a. NAME OF PERFORMING ORGANIZATION: University of New Mexico; 6b. OFFICE SYMBOL (If applicable) | 7a. NAME OF MONITORING ORGANIZATION: Air Force Weapons Laboratory |
| 6c. ADDRESS (City, State and ZIP Code): Dept of Chemical and Nuclear Engineering, Albuquerque, NM 87131 | 7b. ADDRESS (City, State and ZIP Code): Kirtland Air Force Base, NM 87117 |
| 8a. NAME OF FUNDING/SPONSORING ORGANIZATION; 8b. OFFICE SYMBOL (If applicable) | 9. PROCUREMENT INSTRUMENT IDENTIFICATION NUMBER: F29601-82-K-0075 |
| 8c. ADDRESS (City, State and ZIP Code) | 10. SOURCE OF FUNDING NOS. |

| PROGRAM ELEMENT NO. | PROJECT NO. | TASK NO. | WORK UNIT NO. |
|---|---|---|---|
| 62601F | 8809 | 17 | 19 |

11. TITLE (Include Security Classification): OPERATIONAL CHARACTERISTICS OF A HIGH VOLTAGE DENSE PLASMA FOCUS

12. PERSONAL AUTHOR(S): Woodall, David M.

| 13a. TYPE OF REPORT | 13b. TIME COVERED | 14. DATE OF REPORT (Yr., Mo., Day) | 15. PAGE COUNT |
|---|---|---|---|
| Final Report | FROM 7 May 82 TO 19 Apr 85 | 1985 November | 168 |

16. SUPPLEMENTARY NOTATION

from 19

| 17. COSATI CODES | | |
|---|---|---|
| FIELD | GROUP | SUB. GR. |
| 20 | 09 | |
| | | |

18. SUBJECT TERMS (Continue on reverse if necessary and identify by block number): Coaxial Plasma Discharge, Dense Plasma Focus (DPF), Pulsed Neutron Source

19. ABSTRACT (Continue on reverse if necessary and identify by block number)

A high voltage dense plasma focus powered by a single-stage Marx bank was designed, built and operated. The maximum bank parameters are: voltage--120 kV, energy--20 kJ, short-circuit current--600 kA. The bank impedance is ~200 mΩ. The plasma focus center electrode diameter is 1.27 cm. The outer electrode diameter is 10.16 cm. Rundown length is ~10 cm, corresponding to a bank quarter period of ~900 ns. Rundown L is ~50 mΩ.

The context of this work is established with a review of previous plasma focus theoretical, experimental and computational work and related topics. Theoretical motivation for high voltage operation is presented. The design, construction and operation of this device are discussed in detail. Results and analysis of measurements obtained are presented.

(over)

| 20. DISTRIBUTION/AVAILABILITY OF ABSTRACT | 21. ABSTRACT SECURITY CLASSIFICATION |
|---|---|
| UNCLASSIFIED/UNLIMITED ☒ SAME AS RPT. ☐ DTIC USERS ☐ | Unclassified |

| 22a. NAME OF RESPONSIBLE INDIVIDUAL | 22b. TELEPHONE NUMBER (Include Area Code) | 22c. OFFICE SYMBOL |
|---|---|---|
| Lt D. J. Hall | (505) 844-1851 | AWPP |

DD FORM 1473, 83 APR EDITION OF 1 JAN 73 IS OBSOLETE.

UNCLASSIFIED

SECURITY CLASSIFICATION OF THIS PAGE

19. ABSTRACT (Continued)

Device operation was investigated primarily at 80 kV (9 kJ), with a gas fill of ~1 torr $H_2$, plus 3-5 percent A. The following diagnostics were used: gun voltage and current measurements; filtered, time-resolved x-ray PIN measurements of the pinch region; time-integrated x-ray pinhole photographs of the pinch region; fast-frame visible light photographs of the sheath during rundown; and $\dot{B}$ probe measurements of the current sheath shortly before collapse.

TABLE OF CONTENTS


| Section | | Page |
|---|---|---|
| 1. | Introduction | 1 |
| | Brief Description of Plasma Focus Operation | 4 |
| | Brief History of the Plasma Focus | 12 |
| | Detailed Description of Plasma Focus Operation | 18 |
| | Objectives of High Voltage Operation | 52 |
| 2. | The UNM HVDPF--Design, Construction and Operation | 63 |
| | General Considerations | 63 |
| | System Component Description | 75 |
| | Short-Circuit Measurements | 100 |
| 3. | Experimental Studies Performed with the UNM HVDPF | 104 |
| | Gun Header Current and Voltage Measurements | 104 |
| | X-ray PIN Measurements | 112 |
| | $\dot{B}$ Probe Measurements | 126 |
| | Fast-Frame Visible Light Photographs | 128 |
| | X-ray Pinhole Photographs | 131 |
| 4. | Conclusions | 137 |
| | High Voltage Operation | 137 |
| | Short Rundown | 140 |
| | Small CE Diameter | 141 |
| Appendix A | | 146 |
| Appendix B | | 151 |
| References | | 153 |
| Glossary | | 157 |

FIGURES


| Figure | | Page |
|---|---|---|
| 1 | Basic Geometry of a Mather Geometry Plasma Focus Device . . . . . | 5 |
| 2 | Equivalent Circuit of a Typical Plasma Focus Experiment and Relevant Parameters . . . . . | 8 |
| 3a | Normalized Current as a Function of Normalized Time for Various Values of $\dot{L}/Z_o$. (From Ref. 85) . . . . | 13 |
| 3b | Peak Normalized Current as a Function of $\dot{L}/Z_o$ . . . | 13 |
| 4 | Topological Transformation of Linear Z-Pinch to DPF | 16 |
| 5 | Prebreakdown Geometry in Breakdown Region . . . . . | 20 |
| 6 | Prebreakdown Insulator Modification of Purely Radial Electric Field . . . . . | 21 |
| 7 | Typical Paschen Breakdown Curve (From Ref. 31) . . . | 23 |
| 8 | Decker's Paschen-like Curve for Plasma Focus Breakdown (From Ref. 12) . . . . . | 25 |
| 9 | Geometry for Simple Snowplow Velocity Derivation . | 34 |
| 10 | 2-D Snowplow Sheath Profile Development (From Ref. 39) . . . . . | 39 |
| 11 | Steady-state Fluid Sheath Structure (From Ref. 40) . . . . . | 40 |
| 12 | 2-D Plasma Fluid Code Sheath Structure (After Ref. 42) . . . . . | 42 |
| 13 | Bernard Scaling of Neutron Yield with Peak Current (From Ref. 51) . . . . . | 53 |
| 14 | $I_p$ as a Function of $V_o$. $\dot{L}$ = 40 mΩ, W = 20 kj, $\dot{I}_o = 1 \times 10^{12}$ A/s . . . . . | 56 |
| 15a | Typical DPF Load Impedance as a Function of Normalized Time . . . . . | 58 |
| 15b | Energy of Several Plasma Focus Devices versus Normalized Impedance . . . . . | 59 |

FIGURES (Continued)


| Figure | | Page |
|---|---|---|
| 16 | Comparison of Currents vs Time Obtained by MHD Calculations for Two Bank Voltages. Energy of bank--45 kJ. External inductance--25 nH. (After Ref. 11) . . . . . | 60 |
| 17 | Basic HVDPF Bank Circuit and System Design Specifications . . . . . | 64 |
| 18 | Inductance Expressions for Three Common Experimental Geometries . . . . . | 66 |
| 19 | Three Types of Magnetic Pressure . . . . . | 68 |
| 20 | Switch Header Power Flow Problem . . . . . | 71 |
| 21 | HVDPF Electrical Schematic . . . . . | 76 |
| 22 | Photograph of Complete HVDPF System . . . . . | 77 |
| 23 | Scyllac Capacitor Construction and Capacitor Power Connection . . . . . | 80 |
| 24 | Rail-Gap Switch Construction (Courtesy of Maxwell Labs) . . . . . | 83 |
| 25 | Rail-Gap Flashguard Arrangements (Courtesy of Maxwell Labs) . . . . . | 84 |
| 26 | Switch Header Design . . . . . | 85 |
| 27 | Photograph of Complete Switch Assembly . . . . . | 86 |
| 28 | Switch Biasing/Trigger Circuitry . . . . . | 88 |
| 29 | Gun Header Design . . . . . | 90 |
| 30 | Micro-Marx Electrical Schematic (From Ref. 53) . . | 94 |
| 31 | Typical Micro-Marx Output Pulse. Charge Voltage is ~ 25 kV . . . . . | 96 |
| 32 | Schematic of Vacuum System . . . . . | 99 |

FIGURES (Continued)


| Figure | | Page |
|---|---|---|
| 33 | Typical Short-circuit I and $\dot{I}$ Waveforms | 101 |
| 34 | Typical V, $\dot{I}$, I, X Waveforms | 106 |
| 35 | Quantities Used to Estimate Sheath Formation Energy | 108 |
| 36 | Idealized L(t) | 110 |
| 37 | Quantities Used to Evaluate Experimental $\dot{L}(t)$ | 113 |
| 38 | Si X-ray PIN Response | 114 |
| 39 | X-ray Absorption Coefficient of Aluminum | 115 |
| 40 | PIN Electrical Schematic | 116 |
| 41 | Correlation between Filtered PIN Signals and V and $\dot{I}$ Signals | 118 |
| 42 | Thermal Bremsstrahlung Spectra for Pure, Constant Density, Fully Ionized Plasma with No Recombination Radiation | 124 |
| 43 | PIN Response Ratios for 1 mil Al Filter and 5 mil Al Filter | 125 |
| 44 | Locations of $\dot{B}$ Probe Measurements | 129 |
| 45 | $\dot{B}$ Probe Measurement Obtained at 1 T $H_2$, 5% A, 80 kV | 130 |
| 46 | Reference Photograph for Fast-Frame Visible Light Photography of the Sheath. CE face is illuminated from the right by a flashlight | 132 |
| 47 | ns Exposure Photograph of 1 T $H_2$, 5% A, 80 kV Sheath | 133 |
| 48 | Typical X-ray Pinhole Photo of Pinch Region | 135 |
| 49 | High Spatial Resolution X-ray Pinhole Photo | 136 |
| 50 | Photographs of CE | 143 |

FIGURES (Continued)


| Figure | | Page |
|---|---|---|
| A-1 | Evolution of Breakdown by Townsend Avalanche (After Ref. 31) . . . . . | 147 |
| A-2a | Propagation of Anode-directed Streamer (From Ref. 161) . . . . . | 149 |
| A-2b | Propagation of Cathode-directed Streamer (From Ref. 161) . . . . . | 149 |

# 1. INTRODUCTION

## Overview

Since the discovery in the early sixties of the plasma focus mode of operation in a coaxial plasma discharge, the dense plasma focus (DPF) has maintained the interest of plasma researchers for several reasons (Ref. 1, 2 and 3).* It is the pulsed fusion reactor which holds the record for fusion neutrons produced per shot (Ref. 5). Despite this success, DPF fusion energy output is still far below that required for commercial fusion power production. The neutron production mechanisms are still uncertain and are under investigation. Increasingly refined probes are used to study the fast and complex, highly energetic processes involved. While such studies may ultimately permit scale-up of plasma focus devices to break-even levels, at present they provide knowledge about basic plasma physics in interesting domains of magnetically confined, high density, high temperature plasmas.

As mentioned, the DPF is an intense pulsed source of neutrons. It is also an intense pulsed source of x-rays, infrared and microwave radiation and high energy beams of electrons and ions. It is also a source of multiple-ionized plasma species. For these reasons the DPF is frequently used as a laboratory source for these radiations and energetic particle beams (Ref. 6, 7, 8 and 9).

The large impedance change which occurs during and after the focus has potential application as a fast-opening switch for inductive energy storage schemes (Ref. 10). Inductive storage is of interest because of the high energy density obtainable in a magnetic field compared to that of conventional capacitive energy storage. However, inductive storage places unique demands on an opening switch, in order to deliver the stored magnetic energy to a load. The DPF shows promise of satisfying such demands.

---

*A similar phenomenon was discovered slightly earlier by Fillipov et al. [44] with a device of similar geometry briefly described on page 18.

The main interest has been to design a capacitively powered DPF, with the capacitor bank charged to voltages of 80 kV and above. This is much higher than the 20-40 kV generally used, and has permitted the study of plasma focus under new operating conditions. This experimental device has operated at voltages that are the highest in the United States and second world-wide only to those achieved at Dusseldorf, Germany (Ref. 11, 12-17).

High voltage operation allows several advantages over lower voltage, devices: (1) For fixed bank energy, larger current (hence, larger neutron and other yields) is generally achieved at higher voltages. (2) For fixed bank energy, higher voltage allows higher bank impedance, reducing the effect on discharge current of the changes in plasma focus load impedance, generally a desirable result. (3) Decker believes that higher voltage operation increases the energy which goes into sheath formation, resulting in a higher quality sheath, hence, a higher quality focus. (4) For given bank energy, higher voltage allows lower bank capacitance and higher bank resonant frequency. The focus should occur near the circuit quarter period, when current is a maximum. For a fast system, less time is available for disruptive plasma instabilities to develop (although less time is also available for thermal equilibration). (5) For fast, high voltage banks, focussing occurs so quickly that the sheath never reaches the cylindrical wall of the outer electrode. This may reduce the evolution of plasma contaminating material from the inner surface of the outer electrode, hence, a cleaner plasma experiment is possible and the possibility of restrike is reduced.

In addition to effects due to higher voltage operation, there are those that are due to the use of a small center electrode diameter. This results in higher electric fields near the electrode before breakdown, which is believed to enhance sheath quality. In addition, a small center electrode diameter can result in larger magnetic fields and current densities near the electrode, which, due to the Lorentz force results in faster sheath lift-off. This reduces contamination of the sheath by insulator material in contact with the hot sheath. These

effects are advantageous but are to be weighed against damage to the center electrode caused by higher current densities before lift-off and degraded pinch dynamics at pinch time. Given these tradeoffs, we are at present inclined to increase center electrode diameter somewhat.

The plasma focus was constructed entirely at the University of New Mexico. The gun geometry is basically one used at Sandia National Laboratories, Albuquerque, New Mexico for many years. The power flow from the capacitor bank to the discharge chamber is based on the plasma focus devices (Ref. 1). A unique feature of this design is the use of a single-stage Marx generator for the power supply. The Marx generator consists of two oppositely charged (with respect to ground) capacitor banks placed in series by a single rail-gap switch.

The design of the device began in May of 1981. In September 1982, the power supply in preliminary form--with two capacitors, a short rail-gap switch and an inductive dummy load--was successfully tested up to voltages of 50 kV. Voltage and current waveforms were later obtained with a plasma focus load using a gas prefill of a few torr of hydrogen with small amounts of argon. Those measurements indicated that focussing was occurring, though erratically, with frequent multiple sheath formation.

This system was expanded to include additional capacitors in order to increase bank energy and pinch current. With this modified system, x-ray PIN measurements were attempted, primarily at 50 kV, the design limit of the short rail-gap switch which was being used at that time. Still, focussing was erratic, due presumably to low bank energy (3 kJ @ 50 kV) and power flow problems resulting from the use of the short rail-gap switch. A long rail-gap switch was installed in June of 1983, permitting higher voltage operation and improved power flow.

At the end of June 1983, the complete system in its final form--with a plasma focus load--was tested, initially at 50 kV. This was followed by voltage increases to 80 kV (9 kJ), achieved in July 1983. Since that time the device operation with the use of voltage and current probes and x-ray detectors has been investigated.

## Brief Description of Plasma Focus Operation

In this paragraph the basic theory of plasma focus operation is briefly discussed to provide familiarity with the terminology and concepts referred to later in the document. A more complete discussion of various topics in plasma focus operation is presented in the paragraph entitled Focus. Higher voltage operation is discussed in terms of current optimization in the Circuit Analysis paragraph.

## Breakdown and Lift-off

The dense plasma focus is basically a z-pinch created at the tip of the center electrode of a coaxial plasma accelerator (Fig. 1). The accelerator is initially filled with gas of a few torr pressure. For fusion experiments, $D_2$ is usually the fill gas. Other gases commonly used are $H_2$, He, A, Ne, Kr or mixtures thereof. A high voltage (10-200 kV) applied to the electrodes causes gas breakdown. Ideally, breakdown occurs axially along the insulator and quickly forms an azimuthally symmetric, highly conducting plasma sheath. The azimuthal magnetic field ($B_\theta$) due to current in the center electrode (CE), acts on the primarily axial current in the sheath to push the sheath out radially. This is the inverse pinch or lift-off stage. In conventional low voltage plasma focus devices, the sheath lifts off and starts to run down in $\lesssim 1$ μs. In high voltage devices this process occurs in $\lesssim 100$ ns.

## Rundown

As the sheath flares out from the insulator, it acquires a radial current component which interacts with $B_\theta$ to produce an axial force on the sheath. The sheath quickly reaches a nearly constant axial velocity ($\gtrsim 10$ cm/μs) much higher than the fill gas sound speed. The sheath is a supersonic shock which ionizes and sweeps up the gas in its path. The accretion of mass and ionization of gas generally lead to a constant sheath velocity. A snowplow model can be used to predict sheath motion from just after lift-off through rundown (Ref. 18). That model assumes that all the gas encountered by an infinitely thin, infinitely conducting sheath is completely ionized and retained by the

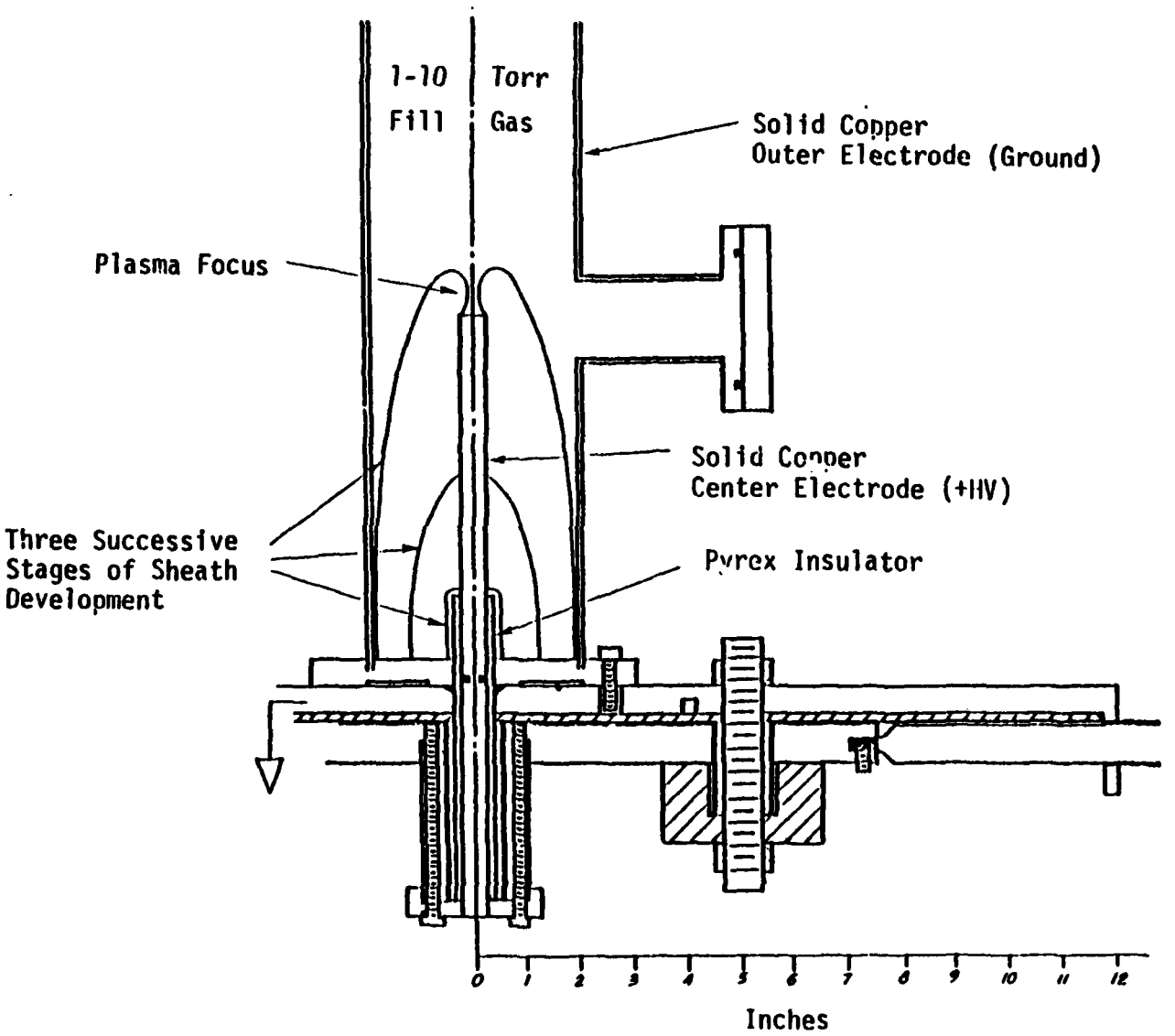


Figure 1. Basic Geometry of a Mather Geometry Plasma Focus Device.

sheath. Sheath thickness in conventional devices is $\gtrsim$ 1 cm. Decker reports sheath thickness of ~ 1 mm for the SPEED 1 high voltage device [15]. Conventional plasma focus sheath electron densities are $10^{17}/cm^3$ with temperatures of ~ 50 eV. The rundown phase lasts approximately for the bank quarter-period, which is typically 3-5 $\mu$s for conventional devices and 400-900 ns for high voltage devices.

Focus

When the sheath reaches the end of the CE, it has the shape indicated in Figure 1. This shape is due to the magnetic pressure normal to the surface of the sheath and the sheath's axial momentum. In the region of sheath constriction, the geometry is conducive to a radial implosion similar to that of a classical z-pinch. The current flowing in the sheath is z-directed, producing a $B_\theta$ which interacts with $J_z$ to accelerate the sheath radially inward. This is the dense plasma focus. When the pinch reaches minimum radius, there is radial pressure balance between the plasma's thermal pressure and the confining magnetic field. Such a configuration is MHD unstable and theoretically is quickly disrupted by instabilities. The focus, however, remains stable longer than predicted, probably due to the curvature of this type of pinch during implosion. The final pinch may be a few millimeters in diameter, ~ 1 cm in length, and may contain plasma at up to a few kiloelectronvolts temperatures with densities of up to $10^{19}/cm^3$. The pinch typically lasts ~ 100 ns before breaking up.

Neutron Production

When the fill gas is $D_2$, one or two large pulses of 2.45 MeV fusion neutrons may be produced after the focus attains maximum compression and MHD instability occurs. The record yield in a single shot is $10^{12}$ n. Experimentally, neutron yield is found to scale over a large range of device discharge current values as $Y_n = 1.2 \times 10^{10} I^{3.3}$, where I is MA in the device (hopefully in the pinch) at pinch time. The $I^4$ dependence can be heuristically derived from pressure balance, yielding the Bennett pinch relation. Note that the D-D reaction rate is proportional to $n_D^2$, where $n_D$ is deuteron number density. From

pressure balance in the pinch, we find that for a cylindrical, infinitely-conductive plasma column carrying an axial surrface current, the pressure, $p_{th}$, of the equilibrium plasma is balanced by the magnetic pressure, $p_m$, at the surface. That is, $p_m = B^2/8\pi = p_{th} = n_D kT$. Also, from Ampere's law, neglecting displacement current and plasma diamagnetism, $B \propto I$ and D-D neutron production goes as $I^4$. This assumes, as is usually observed, that the pinch volume, temperature and duration are more or less constant. This also assumes a thermonuclear production mechanism: deuterons in the tail of the distribution function of the thermalized plasma are magnetically confined in the column and have enough kinetic energy to overcome nuclear electrostatic repulsion and Bremsstrahlung losses. In fact, there are other possible neutron production mechanisms, i.e., nonthermal, nonisotropic deuteron distribution functions, and a mixture of these mechanisms is believed to obtain in a given device for given operating conditions. The most popular interpretations of DPF neutron production include thermonuclear, beam-target and beam-beam mechanisms. There is insufficient data to determine dominant neutron production mechanisms in this device.

Particle Beams and Beam X-Ray Production

Evidence for nonthermal processes is found in the fact that, along with neutrons, the DPF produces high-current ($\gtrsim$ 100 kA) beams of particles. For a typical device with positive polarity CE, particles produced include several megaelectronvolt electrons directed into the CE and several megaelectronvolt ions directed away from the CE. These results suggest that the common accelerating mechanism for such particles is a transient ($\gtrsim 10^7$ V/cm) electric field. It is believed by some scientists that the current and energy of the electron beam account for most of the x-ray emission produced by the plasma focus (Ref. 19) (though this is disputed by others [Ref. 20]). In this model the high energy electron beam strikes the CE (usually copper) producing x rays in the same way an x-ray tube does, with line radiation characteristic of the CE material. The alternative of a hollow CE allows such particles to be studied experimentally. The presence of an ion

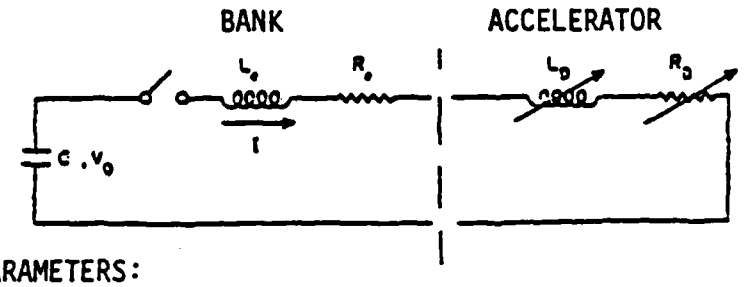


BANK PARAMETERS:

| | |
|---|---|
| C | Bank Capacitance |
| $V_o$ | Initial Voltage on C |
| $L_e$ | Inductance of System External to Volume of Plasma Accelerator |
| $R_e$ | Resistance of System External to Volume of Plasma Accelerator |
| $W = \frac{1}{2}CV_o^2$ | Bank Energy |
| $\frac{\tau}{4} = \frac{\pi}{2}(L_o C)^{1/2}$ | Bank Quarter Period (Risetime) |
| $Z_o = \left(\frac{L_o}{C}\right)^{1/2}$ | Bank Impedance (Source Impedance) |
| $I_{sc} = \frac{V_o}{Z_o}$ | Short-circuit Current |
| $\dot{I}_o = \frac{V_o}{L_o}$ | Initial Current Rise |

ACCELERATOR PARAMETERS:

| | |
|---|---|
| $L_D$ | Variable Inductance of Device--due to Electrical Behavior of Plasma |
| $R_D$ | Variable Resistance of Device--due to Electrical Behavior of Plasma |
| $\dot{L} = \frac{d}{dt} L_D$ | |
| $R_D + \dot{L}$ | Device Impedance (Load Impedance) |

SYSTEM PARAMETERS:

| | |
|---|---|
| $R = R_e + R_D$ | Total Resistance |
| $L = L_o + \int_0^t \dot{L} dt$ | Total Inductance |
| $L_o = L_e + L_D(t=0)$ | Initial System Inductance |

Figure 2. Equivalent Circuit of a Typical Plasma Focus Experiment and Relevant Parameters.

beam would seem to favor beam-target and/or beam-beam neutron production. However, neutron flux, anisotropy, energy and temporal emission behavior calculations do not always support this theory. The origin of such large E fields themselves is also uncertain. Early work on neutron production in linear z-pinches suggested that the large increase in inductance due to periodic radial constrictions of the sheath caused by the m - 0 instability could produce such E fields (Ref. 21). Recently, numerical calculations suggest that $m \geq 1$ instabilities in the pinch lead to the formation of current filaments and quasi-soliton wave packets in the plasma which could create these E fields [21]. In recent years the prevalence and significance of plasma turbulence in the vicinity of the sheath and the focus have received increasing scrutiny. Density fluctuations due to turbulence may also give rise to large accelerating fields.

Circuit Analysis

In most cases, the electrical energy applied to a DPF is initially stored in a capacitor bank, although inductive storage and magneto-implosive generators are also used. An equivalent circuit of a typical DPF experiment is shown in Figure 2, along with a list of relevant circuit parameters.

In the simplest analysis it is assumed that $R = 0$ and $L = L_o$. In this case there is an undamped LC circuit for which

$$I(t) = \frac{V_o}{Z_o} \sin\omega t = I_{sc} \sin\omega t \qquad (1)$$

$I_{sc}$ is the maximum current of the system in the absence of any load, and is obtained by equating maximum electrostatic energy to maximum magnetic energy:

$$\frac{1}{2} C V_o^2 = \frac{1}{2} L_o I_{sc}^2 \qquad (2)$$

Also, $\omega = (L_o C)^{-1/2}$, is the resonant frequency of the circuit, and $R_c = 2Z_o$ is the critical damping resistance, that value of resistance in an LCR circuit separating underdamped and overdamped behavior. Also

$Z_0 = (L_0/C)^{1/2}$. Maximum current will occur at $\tau/4$, which is the quarter-period. In this analysis one would maximize current by increasing $V_0$ and decreasing $Z_0$. Note, however, that a reasonably accurate analysis of DPF performance must include the effect of $\dot{L}$, since it may become quite large during inverse pinch and collapse. Even during rundown, where $\dot{L}$ is nearly constant, its value may be comparable to the bank impedance. Neglecting it would be a serious oversight since the effect is to reduce peak current. In the case where $\dot{L} \gtrsim Z_0$, the electrical behavior of the system is in fact dominated by $\dot{L}$. An analysis of energy transfer from the bank to the pinch must include $\dot{L}$ effects.

The $\dot{L}$ is the result of plasma sheath motion, i.e., the conversion of electrical energy into the primarily axial kinetic energy of the sheath. This energy cannot be simply converted back into electrical energy. As for resistive losses due to Joule heating, $\dot{L}$ gives rise to a dissipative term in the circuit equation. In fact, $\dot{L}$ has the units of resistance, and the analogy of $I\dot{L}$ with IR in an LCR circuit would be exact except that positive $\dot{L}$ also increases total system inductance with time. This amounts to storing magnetic energy in the volume behind the sheath. The $\dot{L}/z_0$ is an important parameter when including the effect of $\dot{L}$ damping on an L(t)C circuit.

A refinement of the previous analysis is to assume that $\dot{L}$ is a nonzero constant (as is the case for most DPFs during rundown). For DPFs, rundown $\dot{L}$ is often taken as

$$\dot{L} = 2\frac{nH}{cm}\left(\ln\frac{r_o}{r_i}\right) v_s\left(\frac{cm}{\mu s}\right) \quad m\Omega \tag{3}$$

Here $r_i$ and $r_o$ are the radii of the inner and outer electrodes, respectively, and $v_s$ is the axial sheath velocity, assumed to be constant.

The circuit equation is given by

$$IR + \frac{Q(t)}{C} = -\varepsilon = -\frac{d}{dt}\left(\int \bar{B} \cdot \partial\bar{A}\right) = -\frac{d}{dt}\,\phi \tag{4}$$

Ampere's law in cgs-Gaussian units is

$$\nabla \times \bar{H} = \frac{4\pi}{c}\,\bar{J} + \frac{1}{c}\,\frac{\partial \bar{D}}{\partial t} \tag{5}$$

For high conductivity, the displacement current can be neglected. Also neglecting plasma diamagnetism, $\mu = \mu_0$, and we find that $B \propto I$, which allows us to write $\phi = IL$. Hence the circuit equation takes the following form:

$$\frac{d}{dt}\,(IL) + IR + \frac{1}{C}\int_0^t Idt = V_0 \tag{6}$$

Assuming $\dot{L}$ is constant, this may be written as

$$(L_0 + \dot{L}t)\,\frac{dI}{dt} + I\dot{L} + IR + \frac{1}{C}\int_0^t Idt = V_0 \tag{7}$$

From the initial condition, $I(t = 0) = 0$, also note that

$$\dot{I}_0 = \frac{V_0}{L_0} \tag{8}$$

Equation 5 has been solved in Reference 22 and later in Reference 11. For $R \neq 0$, the solution for the current involves Bessel functions with noninteger indices. However, $R = 0$ is a good approximation and yields the following simple Bessel function solution:

$$I(t) = I_{sc}\,\frac{\alpha}{\omega'}\,\frac{J_1(\alpha)J_{-1}(\omega') - J_{-1}(\alpha)J_1(\omega')}{J_2(\alpha)J_{-1}(\alpha) - J_{-2}(\alpha)J_1(\alpha)} \tag{9}$$

where

$$\alpha = \frac{2Z_0}{\dot{L}} \quad \text{and} \quad \omega' = \left[\alpha\left(\alpha + \frac{4\pi t}{\tau}\right)\right]^{1/2}$$

Plots of $I(t)/I_{sc}$ are given in Figure 3a for several values of $\dot{L}/Z_0$. It is seen that for $\dot{L} \ll Z$, the load has little effect on the discharge current and the current waveform is essentially that of a simple LC circuit. At the other extreme, $\dot{L} \gg Z_0$, the load largely determines the current, tending, as $\dot{L}/Z_0 \to \infty$, to make the bank appear as a constant source. As $\dot{L}/Z_0$ increases, $I_p/I_{sc}$ decreases, as shown in Figure 3b where $I_p$ is the peak current. With increasing $\dot{L}/Z_0$, there is also a slight increase in the time at which maximum current occurs, though this shift is usually not experimentally observable.

This circuit analysis has included most of the important electrical aspects of plasma focus operation during the rundown phase, when $\dot{L}$ is nearly constant. Actual plasma focus operation is complicated by the large inductive changes which occur during inverse pinch and during the focus.

## Brief History of the Plasma Focus

### Comparison with the Linear Z-Pinch

The first attempts at controlled thermonuclear fusion (Ref. 22-24) in the late 1940s used simple linear z-pinches and toroidal z-pinches. The self-constriction of a plasma column carrying a z-directed current was known theoretically since 1934 (Ref. 28) in gaseous electronics and confirmed experimentally in 1951 (Ref. 29). It was natural to use this method with a deuterium gas fill to attempt controlled thermonuclear fusion.

Several problems were soon realized. First, the thermonuclear neutron yield calculated from measured pinch parameters was much lower than the experimentally measured value. Beam acceleration by E fields created in the breakup of the column was suggested as the dominant

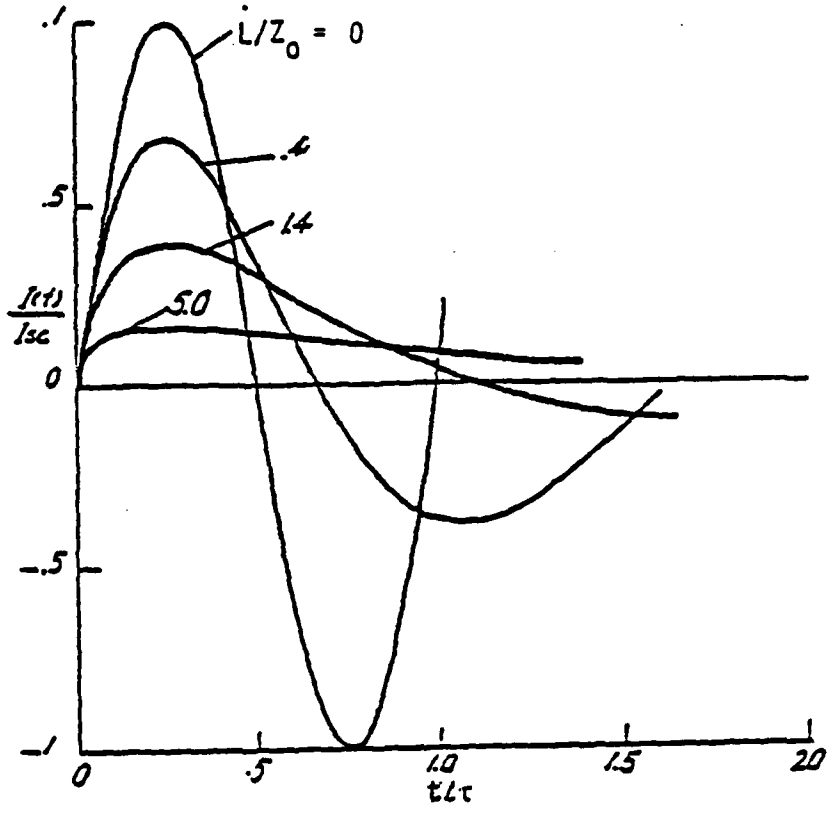


Figure 3a. Normalized Current as a Function of Normalized Time for Various Values of $\dot{L}/Z_0$. (From Ref. 85).

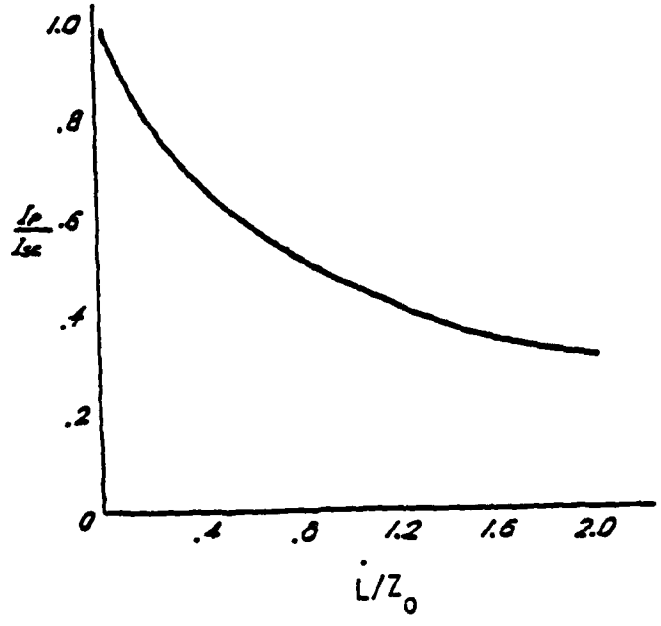


Figure 3b. Normalized Current.

neutron production mechanism. Since it was shown that beam neutron production cannot attain break-even, fusion power production by scaled-up linear z-pinches seemed doomed (Ref. 30).

There were also insulator problems. In a linear z-pinch the gas breaks down in the lowest inductance mode--along the insulator. The forming plasma sheath is in contact with the insulator--and its large surface area--until the sheath lifts off the insulator and begins its radially-inward implosion. The time before lift-off occurred was found to depend on the surface condition of the insulator. Adsorbed water vapor could greatly delay lift-off. Neutron yields were increased by a factor of 100 when quartz insulators were used instead of Pyrex [ 24 ]. The importance of plasma contamination by the insulator was thus established. Finally, during implosion the sheath continuously illuminates the insulator with ultraviolet (uv) and visible light. In higher current devices, this radiation may be very intense, causing the insulator to conduct and shunt pinch current, reducing pinch effectiveness. In addition to these problems, the linear z-pinch is prone to many instabilities, including $m = 0$, $m = 1$ and Rayleigh-Taylor.

For these and other reasons, CTF interest in the linear z-pinch waned and other magnetic confinement schemes were pursued, such as the theta pinch, toroidal pinch, etc.

In the late 50s and early 60s, interest developed in coaxial plasma accelerators, partly due to interest in entropy trapping fusion schemes (Ref. 31). One of the most famous of these accelerators was the Marshall plasma gun (Ref. 32). The electrode geometry is that of the Mather geometry plasma focus, although in Marshall's original design the insulator was flat against the back wall, filling the annulus between the center and outer electrodes. Also, in the Marshall gun, the gas is not prefilled. Gas is admitted from a plenum by a solenoid valve through ports in the CE. Timing of gas admission relative to application of high voltage to the electrodes can be varied. After breakdown, the sheath moves down the length of the accelerator in what has become known as the deflagration mode. This

mode is distinct from the snowplow mode in that sheath thickness is greater, sheath velocity is less,and gas pressure is usually much less. What is more important, no significant focussing occurs in the deflagration mode. This mode of plasma gun operation is still used in plasma injection applications. (More accurately, the deflagration mode will change to the DPF mode as the delay between gas admission and application of high voltage is increased. For static gas fill of sufficient pressure the DPF mode will be obtained.)

In the early sixties, Mather, experimenting with various ways of admitting gas and timing the application of high voltage to the electrodes of a Marshall-type gun, discovered the dense plasma focus mode of operation in a coaxial plasma accelerator. Its most remarkable features were: large neutron yield with deuterium prefill; a large pinch voltage due to the large $\dot{L}$ of the pinch; and the consequent reduction in current. A similar type of pinch was observed earlier in the so-called Filippov geometry [4], where electrode radii are much larger and rundown length is almost zero; the focus occurs during inverse pinch, i.e., before the sheath reaches the outer electrode.

As mentioned earlier, the plasma focus is a short z-pinch, but it differs from a linear z-pinch in some respects which makes it superior to the linear z-pinch. First, the plasma near the pinch touches only one electrode, the CE, thus reducing plasma cooling by electrode contact. As a curiosity, the linear z-pinch may be topologically transformed into a plasma focus as shown in Figure 4. From this figure it is seen that B-field lines are convex to the plasma in the linear z-pinch; hence this configuration is unstable. For the DPF, B-field lines are concave to the plasma during inverse pinch and rundown, providing stability during these phases of DPF operation.

Secondly, the sheath is formed on an insulator of much smaller surface area (in Mather geometry) than that of a linear z-pinch. This reduces plasma contamination. Plasma contamination is further reduced by shortened lift-off times due to the generally increased magnetic fields and current densities at the smaller CE radii of (Mather geometry) DPFs.

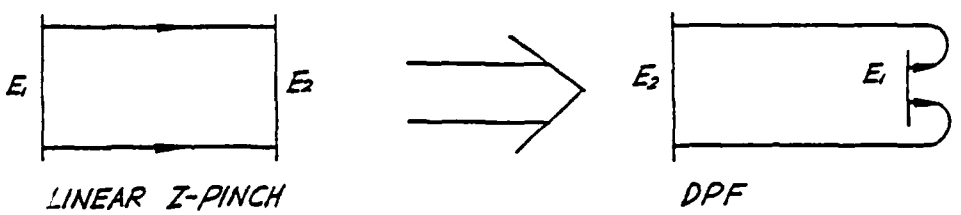


Figure 4. Topological Transformation of Linear Z-Pinch to PDF.

Thirdly, during rundown the insulator is irradiated obliquely by the sheath. And during pinch, when sheath luminosity peaks, the insulator is completely hidden from the pinch. These effects reduce enhancement of insulator conductivity by UV or other radiation.

Finally, the z-pinch produced by the plasma focus lasts longer than is predicted for a simple z-pinch. Presumably this is due to the way this particular z-pinch is formed.

Interest in the Plasma Focus

Much of the early funding of plasma focus research was aimed at developing the device as a simulator of nuclear burst neutrons and/or x- and $\gamma$-rays. This type of simulation has remained a large industry in this country and others for many years because testing systems in actual nuclear bursts is either very costly, as in an underground test, or impossible or extremely unpopular, in the case of atmospheric or exoatmospheric tests. Interest in the plasma focus was initially very high because of its weapons simulation potential. The highest per shot neutron yield in any CTF device--$10^{12}$ n--was obtained by a Los Alamos National Laboratory plasma focus. Also, the relative simplicity and low cost of building and operating a plasma focus, as compared with, say, building and operating a tokamak, immediately made the device very popular with plasma physicists world-wide. However, as defense interest (and funding) in the device waned, and the neutron production mechanisms remained obscure, the plasma focus seemed for a time best suited for low or medium energy experiments at universities or small research labs, with little or no serious interest in pursuing its breakeven CTF possibilities.

In recent years in Europe, however, there has been serious interest in developing the plasma focus as a fusion reactor. European facilities of 200 kJ-1 MJ now attain currents of up to 1.5 MA, though problems have been encountered with current leakage along the insulator, diverting current from the pinch. These problems are being actively addressed and plans considered for higher energy facilities. It is believed that experiments at ~ 30 MJ will be sufficient to explore the fusion reactor possibilities of this device.

Concurrent with the European revival of interest in the plasma focus has been the development of high voltage plasma focuses. Scientists were prompted to go to higher voltages by the higher currents obtainable for fixed bank energy. This avenue was not explored by earlier workers because higher voltage operation presents many technical problems not easily solved in the early days of the plasma focus. Also, this method has limitations for higher energy banks. To operate at higher energies with the benefits of high current efficiency and high bank impedance obtained at high voltage, one must go to excessively high operating voltages. Therefore, though present high voltage experiments are interesting and useful, their results mustbe applied judiciously to the design of higher energy devices.

Detailed Description of Plasma Focus Operation

In this paragraph the plasma focus operation is examined in more detail by discussing: breakdown; rundown; collapse and focus; neutron, x-ray and particle beam production; and miscellaneous topics. The paragraph summarizes the experimental, theoretical, and computational work performed to date on the plasma focus and related topics. This will provide context for the work presented in later sections. Where appropriate, original analysis and interpretation is included. It also serves as an introduction to the methods of analysis used in chapter 3 and supports the conclusions reached.

Breakdown and Lift-Off

The breakdown and lift-off process is not well understood, though it is known to determine the parameters of the current sheath and the dynamics of the subsequent focus. This discussion is broken into several topics. First, is a discussion of the prebreakdown period between theapplication of high-voltage and the onset of significant current flow in the discharge. During prebreakdown, a transition occurs from a purely electrostatic boundary value problem with no free charge in the gas to an electron transport problem within the gas leading to the conditions under which breakdown and sheath formation

occur. Then breakdown itself is discussed, noting its Paschen-like characteristics and the modifications made to ordinary gas breakdown theory by the introduction of an insulator. Incidental topics here are current starvationand diffuse versus low inductance breakdown. Finally, we make some remarks regarding sheath formation and lift-off.

Prebreakdown

In the prebreakdown process, a high voltage (10 to 200 kV) is applied to two electrodes separated by a solid insulator and by a low pressure (0.5-20 torr) gas. The applied voltage has a typical risetime of 50 to 100 ns. Before the gas conducts electricity, the geometry is that of a coaxial transmission line. The length of this line is typically 10 to 30 cm, so that electromagnetic wave transit times are subnanosecond. For the present considerations we may, therefore, assume a constant voltage on the CE at all times and that in the early part of the voltage rise, the field distribution is obtained by solving an electrostatic boundary value problem such as is shown in Figure 5. For a purely radial electrostatic field, the insulator will modify the field as indicated in Figure 6.

Soon electron transport along field lines begins. Electrons initially arise from background cosmic ray ionization of the fill gas and, when field strengths are high enough, ($\gtrsim$ 100 kV/cm), electrons are injected into the discharge volume by cathode field emission. Field emission will occur at surface singularities on the cathode, such as the whiskers prominent in the explosive emission process (Ref. 30) of high voltage cold cathodes, and particularly at the edge of the hole admitting the insulator and center electrode (Ref. 4).

Electron avalanching may occur if field strengths near the anode and gas pressures are right. Avalanching occurs when the electron mean free path $\lambda_e$, is roughly comparable to the distance an electron falls in the electric field to acquire enough energy for impact dissociation and ionization. (Because the dissociation energy is much less than the ionization energy, we include both terms when referring to ionization.) If the mean free path is too short, the electron will strike a neutral before it has enough energy to ionize it. If the mean free path is too

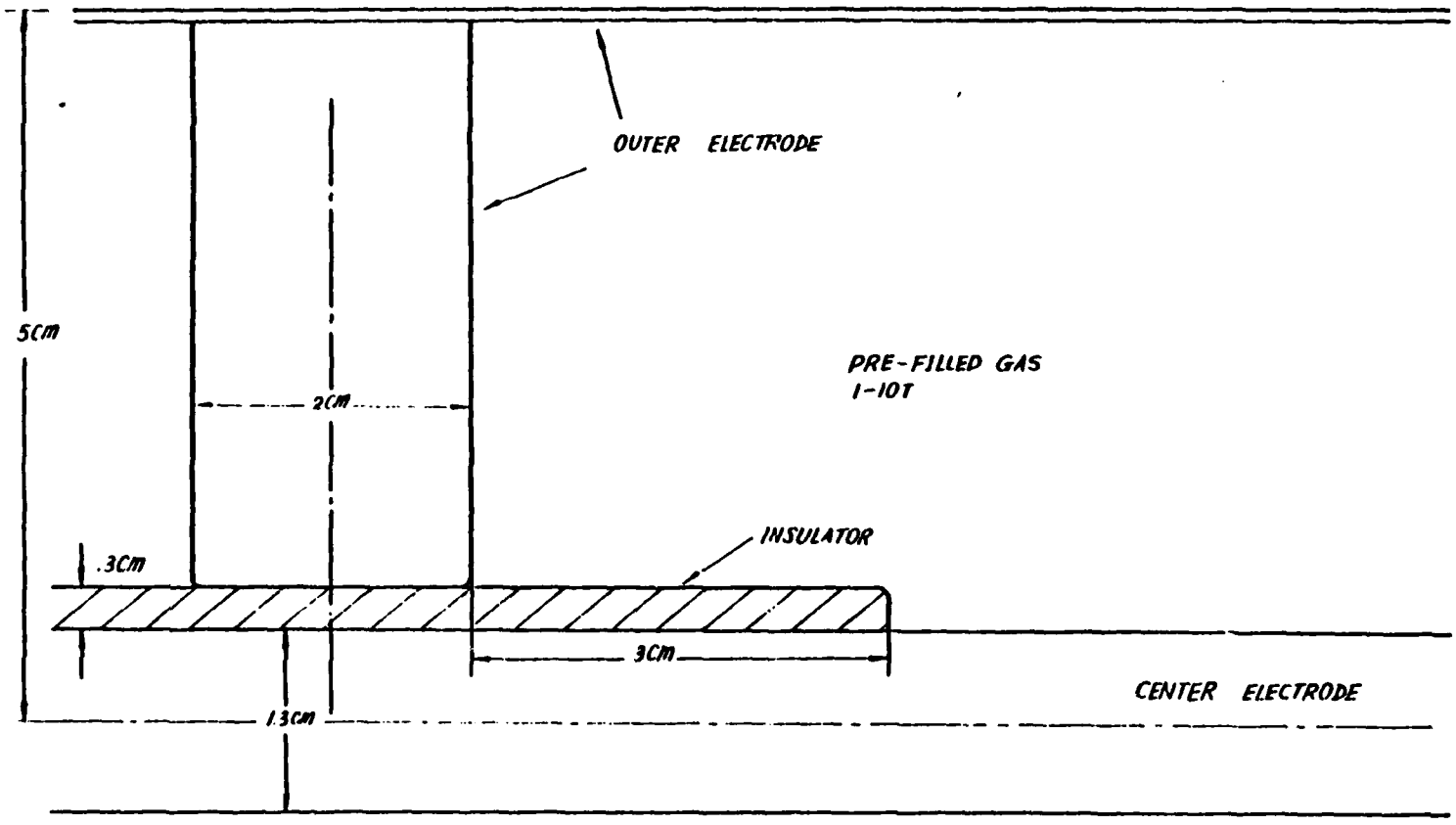


Figure 5. Pre-Breakdown Geometry in Breakdown Region.

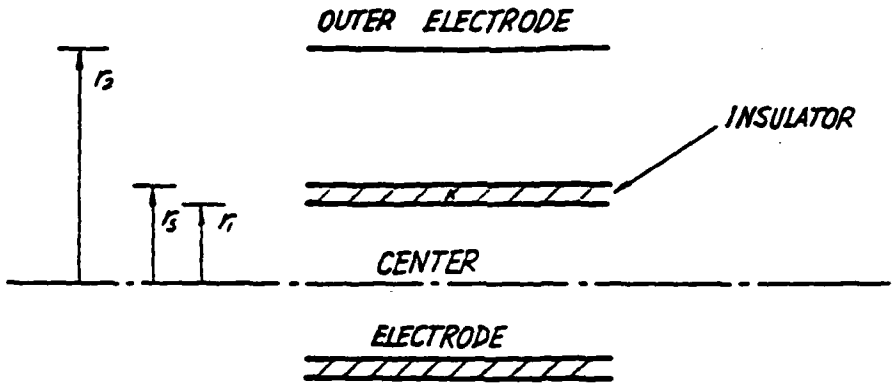


For a potential difference $V_0$ between the electrodes, and insulator relative dielectric constant $\kappa$, the radial electric field is

$$r_1 < r < r_s \qquad E_r = \frac{\alpha V_0}{\kappa r}$$

$$r_s < r < r_2 \qquad E_r = \frac{\alpha V_0}{r}$$

where

$$\alpha = \frac{1}{\ln \left[\left(\frac{r_s}{r_1}\right)^{1/\kappa} \frac{r_2}{r_s}\right]}$$

In our case,

$r_1 = \frac{1}{4}$ in = .635 cm

$r_s = \frac{3}{8}$ in = .9525 cm

$r_2$ = 2 in = 5.08 cm

$\kappa \sim 5$ (Pyrex)

$\alpha$ = .57

Note the slight influence of $\kappa$ on $\alpha$.

| $\kappa$ | 1 | 2 | 3 | 4 | 5 | 10 | 20 | $\infty$ |
|---|---|---|---|---|---|---|---|---|
| $\alpha$ | .48 | .53 | .55 | .56 | .57 | .58 | .59 | .60 |

Figure 6. Prebreakdown Insulator Modification of Purely Radial Electric Field.

long, electrons accelerated in the field will strike the anode before striking any neutrals and ionization will diminish. Since $\lambda_e \sim 1/n_n\sigma_i$, where $n_n$ is the density of neutrals and $\sigma_i$ is the ionization cross-section, these effects lead to a minimum in gas density, the Paschen minimum, at which breakdown, a possible end result of avalanching, occurs (for a DC applied field). This minimum is shown in Figure 7.

The ionization cross-section depends on electron velocity, fill gas type, and to some extent, on neutral velocities, i.e., gas temperature. The production of free electrons by avalanching or other processes is opposed by recombination and electron attachment. Electronegative gases, such as $SF_6$, tend to remove free electrons from the discharge volume. ($SF_6$ is commonly used for electrical insulation.)

In the case of positive CE DPF prebreakdown, proportional counter analysis is somewhat applicable because the geometry is similar and avalanching is important in both cases. Avalanching may enhance electron density near the insulator surface for the usual case of positive CE. Since electrons are the main current carriers in breakdown, the prebreakdown buildup of electron density near the insulator will greatly affect breakdown and sheath formation. It is believed that secondary electron emission will also occur at the insulator. This may also enhance electron density near the insulator.

Electrons will also be released from various surfaces by the photoelectric effect due to radiation emitted by avalanching and recombination. (This process may become important later in time when the sheath luminosity is large, causing the insulator to conduct.)

A surface charge density will develop on the insulator for positive CE. This charge density will tend to make the field purely axial and uniform on the insulator, facilitating axial breakdown. This effect has been inferred from linear z-pinch experiments in which radial collapse proceeds uniformly along the length of the discharge tube*. From snowplow theory this implies uniform axial E field along the tube.

---

*Mather, J. W., private communication.

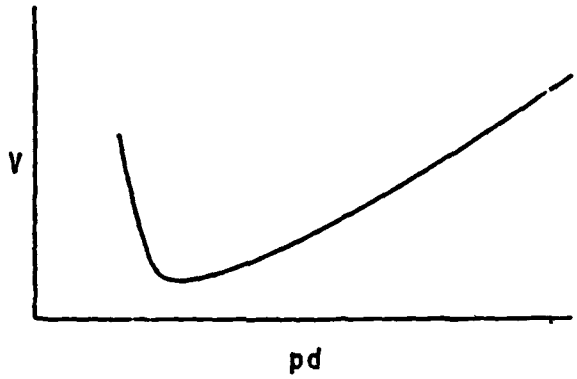


Figure 7. Typical Paschen Breakdown Curve (after Ref. 31).

All of these processes depend on: the risetime, polarity and amplitude of the applied voltage; the pressure and type of fill gas; the geometry of the two electrodes and insulator; and the material and surface preparation of the two electrodes and insulator.

A more detailed discussion of gas breakdown, including streamer formation, is included in Appendix A.

Current Starvation and Ionization Energy

As mentioned, the electron density near the insulator surface before breakdown may greatly affect breakdown and sheath formation. The proper operation of high voltage, high current switches such as spark gaps or ignitrons depends on a supply of current carriers--usually electrons--to initiate and sustain high-current discharges. If there are not enough current carriers, the switch may turn on erratically or extinguish, a victim of current starvation. A similar problem may occur in the breakdown and sheath formation phase of the plasma focus. This may be why low energy, low current discharges usually do not produce good focuses.

The use of hydrogen as a fill gas may lead to erratic or poor focussing because hydrogen has only one electron per atom to contribute to the discharge. (A similar problem is encountered with helium, which has two electrons per atom to contribute to the discharge but a very high ionization potential.) For this reason (and to mass-stabilize the sheath), a small percentage of argon--with 18 electrons per atom--is often added to a hydrogen prefill.

In calculating the energy required to ionize and impart a velocity of ~ 10 cm/$\mu$s to all the gas swept up by the snowplow, it is found that for typical prefill gases and pressures, the total ionization energy required may be a few kilojoules. Such considerations dictate the minimum size of the capacitor bank energy for a given experiment.

DPF Breakdown

Studies of breakdown for a HVDPF have been made at Dusseldorf, Germany (Ref. 12). A Paschen-like curve was developed, (Fig. 8),

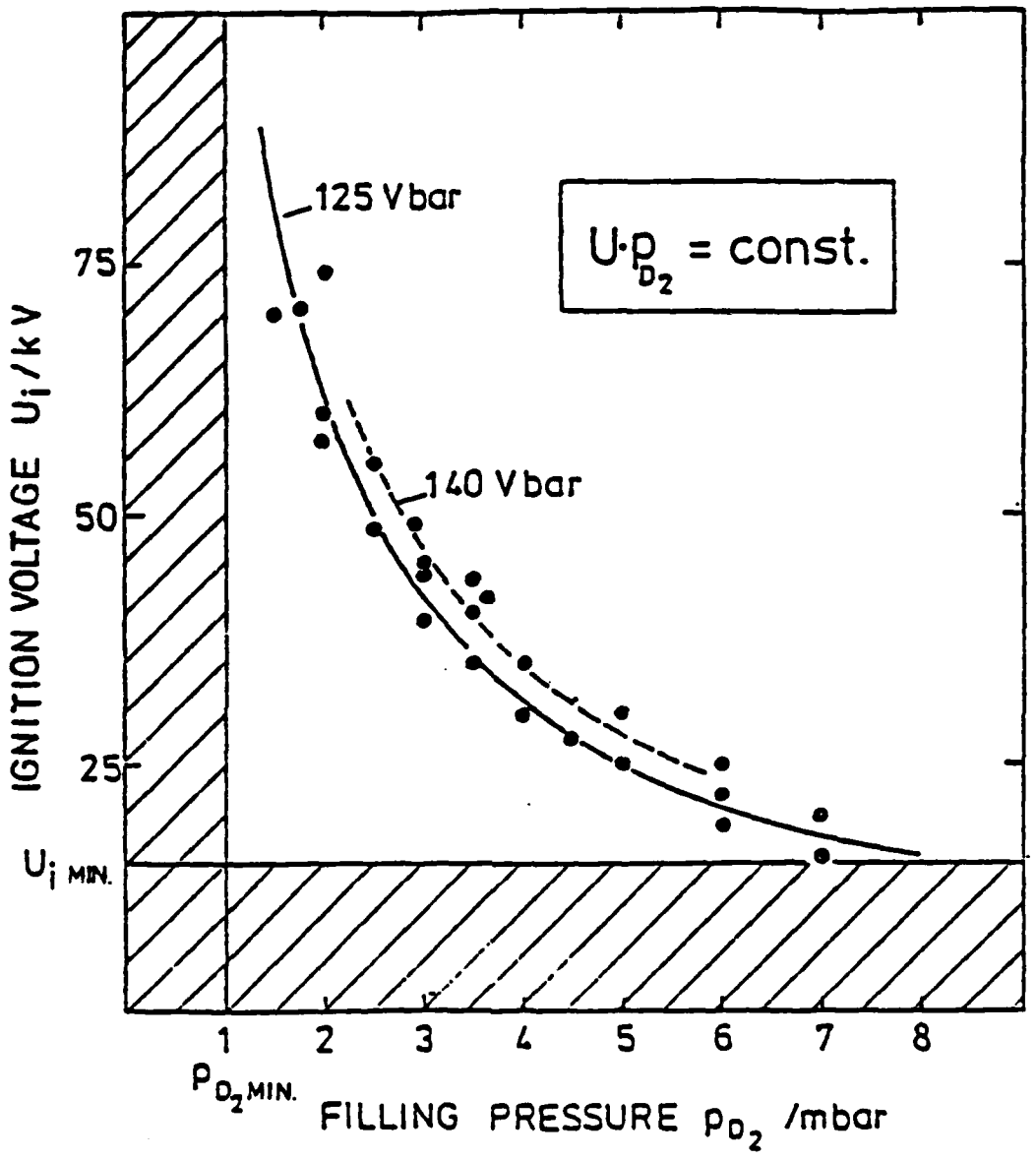


Figure 8. Decker's Paschen-like Curve for Plasma Focus Breakdown. (From Ref. 12).

consisting of ignition voltage versus fill pressure for deuterium. Ignition voltage is defined as that voltage at which dI/dt rises from zero, indicating significant current flow. This sort of measurement requires time correlation and resolution well under 10 ns. It has been noted that the ignition voltage is two orders of magnitude above the static Paschen-curve, presumably for an appropriate geometry. There is resemblance between this type of dynamic breakdown in gas along an insulator in a complicated geometry and the static breakdown just described in a gas for a planar (or other simple) geometry without an insulator. There are also significant differences between the two types of breakdown.

In the prebreakdown situation, even before surface-charge build-up, the insulator modifies the electrostatic field as shown in Figure 6. Surface-charge build-up is another matter, since during this time it is possible to deeply bury electrons in the surface of the insulator. This affects the surface field, as mentioned. Further, during breakdown, heating of the insulator surface may evolve these charges and increase the electron density near the insulator surface, leading possibly to restrike.

In any consideration of electron transport near the insulator, attention must be paid to the insulator's effect on electrons. Electrons may be trapped by the insulator or they may impact it with loss of energy and generation of secondary electrons.

When a breakdown path becomes hot enough, it will melt the insulator surface, and impurities on the insulator surface and insulator material itself will evolve into the developing plasma channel. This has been studied experimentally with the observation that the plasma channel evolves from a cylindrical shape into a more flattened shape which conforms to the insulator (Ref. 32). Also, the plasma channel becomes a more efficient radiator in the UV, due to high Z bremsstrahlung of impurity ions, as noted in UV laser pump experiments (Ref. 33 and 34). In plasma focus experiments, if the insulator is sufficiently contaminated by surface impurities (usually water vapor), the sheath

will fail to lift off. This is commonly observed in the first shots following installation of a new insulator or after long exposure of the vacuum vessel to air.

Experimental data of breakdown and lift-off are sadly lacking. Until the sheath is formed, electron density is generally too low to permit measurement via Schlieren or laser holography techniques. Additionally, time scales for this process are short, typically $\lesssim$ 10 ns. End-on visible light image converter pictures show the formation of many radially-spaced luminous channels during breakdown. Here there is the usual problemof believing that current flows where there is high luminosity.

There is a temptation to draw an analogy between multichanneling in a rail-gap switch and the formation of multiple axial plasma channels along the plasma focus insulator during breakdown. Such an analogy may be justified on the basis of multichanneling observed on dielectrics in surface discharge switches. If in fact the luminous channels are current channels, then insulator enhancement of multichanneling might be plausible. Multichanneling in such a geometry without an insulator would require a dV/dt very much higher than the few kV/ns typical of plasma focus devices.

The question remains open as to whether the luminous channels coalesce in later states of sheath development or retain their identity--even until focus. If these channels are current channels, then magnetic forces would tend to spread them out towards each other to form an azimuthally symmetric sheath. The formation of such a sheath is important in terms of the snowplow effectiveness of the sheath during the inverse pinch stage. That is, if the sheath is a collection of current filaments, rather than a single, azimuthally symmetric current sheet, gas may leak through the filaments and later provide current carriers for restrike. It is worth mentioning that the coalescence of adjacent current filaments into a single current sheet involves resistive field diffusion and magnetic reconnection. When the filaments first form, they are cool enough to permit rapid field diffusion. However, as current in them rises, they become good conductors

and magnetic fields cannot penetrate. Thus there is a trade-off between temperature-dependent conductivity and when currents are large enough to lead to filament coalescence.

The formation of the sheath is also a subject of much interest and speculation. It has been stated that in low voltage plasma focus devices, the long time required, ~ 1 μs, for the sheath to lift off the insulator and start to run down is due to the low $\dot{I}_0$ typical of low voltage devices. Such sheaths are the result of several presheaths which coalesce into a single sheath at ~ 1 μs. This is disputed.* In the high voltage devices, and the ones discussed here, the quarter period is well under a microsecond so that the sheath must form and lift off in a small fraction of that time if it is to run down the length of the center electrode within the quarter period. Decker believes that high voltage devices create a single sheath--no pre-sheaths--which have superior structure--are thin, highly conductive--and lift off the insulator and begin axial acceleration in $\lesssim$ 100 ns.

Diffuse versus Low L Breakdown

As discussed previously, it is common in pulse systems to predict that current will flow in the lowest inductance mode. Thus the breakdown path in a DPF would presumably be along the insulator. Some DPF investigators (Ref. 35) have found it necessary, however, to distinguish between this type of breakdown and another, high inductance, diffuse breakdown. High inductance breakdown is characterized by a diffuse current flow in a large volume between the two accelerator electrodes. This apparent violation of the low inductance mode prediction will be analyzed in subsequent paragraphs.

The low inductance mode prediction depends on risetime--L/R--in an LCR circuit in which the current path under consideration is purely inductive. But current paths, particularly in gases, can be quite resistive. In considering spark-gap closure, for example, the distinction is made between inductive risetime, $\tau_L$, and resistive risetime,

*Ibid

$\tau_R$. The inductive risetime is L/Z where L is channel inductance and Z is the impedance of the circuit driving the channel. Resistive risetime takes into account the time-dependent resistivity of the plasma channel, which depends on plasma channel temperature which is determined by how much energy is dissipated in the channel. Expressions exist (Ref. 36) for $\tau_R$ involving a number of parameters such as plasma channel length, initial gas pressure, etc.

The rail-gap switch is an example where inductive and resistive risetimes compete. The rail-gap switch consists of two parallel main electrode rails with a parallel, knife-edge trigger electrode between them, normally biased so that no field exists at the knife-edge. The lowest inductance mode breakdown here would be a continuous sheet of plasma between the two main electrodes. However, self-breakdown, which occurs when the hold-off voltage between the main electrodes is exceeded, occurs in a single, cylindrical plasma channel.

On a microscopic level, the appearance of an electron with sufficient energy to initiate an avalanche leading to streamer formation and breakdown is a statistical, localized process which precludes the uniform breakdown required for a plasma sheet between the main electrodes. Thus low inductance breakdown in rail-gap self-break is subject to the constraint imposed by the $\tau_R$ of plasma channel formation: except where streamers form, $\tau_R$ is infinite. The application of a fast-rising, high-amplitude pulse to the trigger blade initiates many localized streamers; thereby, reducing the number of infinite $\tau_R$ paths and more closely approximating a uniform breakdown. In the limit of an infinitely fast, high-amplitude trigger pulse, a plasma sheet between the main electrodes would be realized.

In plasma focus breakdown, one must also consider resistive and inductive risetimes. It is believed that low L breakdown occurs when fields and pressures are such that electron avalanching occurs in the vicinity of the anode, promoting very high, localized (electron) conductivity on such time scales that the resistive phase is negligible compared to the inductive phase. If avalanching does not occur, then the situation resembles a relatively brief glow discharge in which current is diffuse throughout much of the accelerator volume.

## Sheath Rundown

It has been observed that during rundown the sheath usually propagates with nearly constant velocity and profile, ionizing and sweeping up nearly all gas it encounters. Various simplified models have been developed for sheath rundown. The simplest are snowplow models in which the sheath is assumed to have zero thickness (a result of perfect conductivity) and to perfectly sweep up and entrain all gas it encounters. If the sheath is allowed to have finite thickness, some degree of structure is permitted, allowing temperature, pressure, density estimates and permitting magnetic diffusion into the sheath. The most sophisticated models of finite structure sheaths are 2-D MHD codes, which can, with some accuracy, model even the early stages of collapse. Some information can also be obtained by considering the shock nature of the sheath. At this point the various rundown models are described in order of sophistication. A few aspects of shock theory of sheath rundown are discussed in Appendix A.

## Validity of Snowplow Assumptions

Zero thickness snowplow models are conceptually appealing. The sheath is considered to be an infinitely thin, perfectly conducting, impenetrable wall which ionizes and extrains all gas that it encounters. There are aspects of this model which merit scrutiny. How effectively does the sheath actually ionize and sweep up gas in its path. In fact, an estimate (Ref. 7) of the density of (ionized) gas left behind the sheath indicates that it is a rather effective snowplow. This estimate was obtained by measuring the time delay between x-ray emission from the anode and the corresponding $\dot{I}$ signal. Then, assuming an average B field in the coaxial volume and complete ionization of residual gas, the propagation velocity suggests that $< 10^{-4}$ of the original mass density is left behind the snowplow. Consider physically why DPF sheaths are usually such good snowplows.

Consider a crude model of sheath structure during rundown. Because of the relative immobility of ions, electrons are the main

current carriers within the sheath. The $\bar{J} \times \bar{B}$ force will act on the electron current layer, pushing it mostly axially. Electrostatic attraction will drag the sheath ions along and both electrons and ions will have sheath axial velocity $v_s$. The sheath will be a double layer (Ref. 37). In addition to this velocity, $v_s$, electrons and ions will have thermal velocities, electric field drift velocities and various $\bar{E} \times \bar{B}$ drift velocities (besides $v_s$). But it can be shown that for typical sheath velocities, thicknesses and densities, neutral collisions with ions moving at $v_s$ lead to complete shock front ionization.

Typical sheath parameters are: $v_s \sim 10$ cm/$\mu$s sheath thickness ~ 1 cm, sheath density ~ $10^{17}$ cm$^{-3}$. The kinetic energy of a proton with velocity, $v_s$, is 52 eV, enough for impact ionization. Consider the mean free path of a hydrogen atom incident on the sheath: $\ell \sim 1/n_i \sigma_H$, where $n_i$ is the density of ions in the sheath and $\sigma_H$ is the cross-sectional area of a hydrogen atom ~ $8.8 \times 10^{-17}$ cm$^2$. With these numbers, $\ell \simeq 0.1$ cm, it can be seen that a neutral incident on such a sheath has a high probability of being ionized.

Though it has been shown that ion impact ionization is sufficient for complete shock front ionization, Reference 37 suggests that electrons at the front of the double layer account for shock front ionization. The kinetic energy of electrons moving at typical sheath velocities is a small fraction of an electronvolt; however, the electron temperature in the sheath is estimated to be 30 eV or so. Ion impact ionization would seem to dominate because the energy transfer is better for equal colliding masses.

Another estimate of the degree of shock heating can be obtained from the Rankine-Hugoniot shock jump relations. For the parameters of interest, one obtains a high degree of ionization.

Finally, the photoionization may be significant since there are experimental results showing that gas is highly ionized before the sheath arrives. We consider this possibility in detail in discussing sheath shock theory in Appendix II.

## 1-D Snowplow Theory

Snowplow theory was originally presented in Reference 18 to predict plasma behavior in an early Los Alamos toroidal z-pinch, the Perhapsatron. A simple example of applying the theory to a linear z-pinch may be found in Reference 45. This example applies directly to plasma focus devices in the region of the focus during collapse.

Consider a cylinder of gas of initial radius $r_o$, density $\rho_o$, length $\ell$, with current I flowing axially on its perfectly conducting surface--a classical z-pinch. The magnetic pressure at the cylinder's surface will be $p_m = B^2/2\mu_o$ (SI) Integrating the pressure over the cylinder's curved surface, A, we have a radially inward force acting on a mass $M(t) = \rho_o \pi \ell (r_o^2 - r^2)$, where r(t) is the cylinder radius at time t. Neglecting thermal pressure for the moment, Newton's second law gives

$$\frac{d}{dt}\left[M(t)\,\frac{dr}{dt}\right] = p_m A \tag{10}$$

And from Ampere's law, neglecting displacement current,

$$B_\theta = \frac{\mu_o}{2\pi}\,\frac{I}{r} \quad \text{(SI)} \tag{11}$$

Thus,

$$\rho_o \frac{d}{dt}\left[(r_o^2 - r^2)\,\frac{dr}{dt}\right] = 10^{-7}\,\frac{I^2}{r} \qquad \text{(SI)} \tag{12}$$

In the original analysis of Reference 18, the current flowing in the pinch was related to the voltage along the pinch (from one end of the torus to the other) by noting that the resistive voltage drop across a perfect conductor is zero; the voltage across the pinch is thus purely inductive and may be obtained from

$$V_i = -\frac{d}{dt}(IL) \tag{13}$$

Finally the voltage was assumed, somewhat arbitrarily, to be constant, resulting in a dimensionless equation for z-pinch compression.

Other choices can be made for the current in Equation 12, such as $I = I_0 + \alpha t$ or $I = I_0 \sin\omega t$. The choice depends on the phenomenon of interest and the experimental set-up. In any case, $\dot{L}_0/Z \ll 1$ simplifies the current waveform. For z-pinch compression during the entire first quarter cycle, with $\dot{L}/Z_0 \ll 1$, $I = I_0 \sin\omega t$ is a good choice. For z-pinch compression in the collapse phase of a plasma focus, I = constant, for $\dot{L}/Z_0 \ll 1$, or $I = I_0 + \alpha t$, otherwise, are good choices. The dimensionless equation given in Reference 35 for a purely linear z-pinch, with $I = dI/dt_0\ t (= V_0/L_0\ t)$ is

$$\frac{d}{d\tau}\left[(1 - x^2)\frac{dx}{d\tau}\right] = -\frac{\tau^2}{x} \tag{14}$$

where

$$x = \frac{r}{r_0}\ ,\ \tau = \frac{t}{t_1}\ ,\ \text{and}\ t_1 = \left(\frac{r_0 c}{\dot{I}_0}\right)^{1/2} \rho_0^{1/4} \tag{15}$$

In this equation $t_1$ is the time for compression. Initial conditions are $x(0) = 1$ and $dx/d\tau_0 = 0$.

The scaling laws contained in Equation 15 can be successfully applied to plasma focus rundown. There are two reasons for this. First, during rundown, $V_i$ = constant is found experimentally to be a fairly good approximation for most plasma focus operating regimes. The second reason has to do with the similarity of the equations of motion in the two cases.

Applying snowplow theory to the rundown phase of a plasma focus yields the following useful equation for sheath velocity,

$$v_s = \left(\frac{c^2E^2}{4\pi\rho_o}\right)^{1/4} \frac{cm}{s} \quad \text{(cgs-Gaussian)} \tag{16}$$

where E is the electric field at the center electrode and $\rho_o$ is the initial mass density of the fill gas.

This formula has been verified experimentally in Reference 7 for deuterium over a large range of pressures (~ 300 to 1400 $\mu$m @ $V_o$ = 16 kV) and bank voltages (~ 13 to 18 kV @ 725 $\mu$m). This equation is quite useful in predicting the effects of changing gas pressures or mixtures on the time of pinch, since it is desirable to have the pinch occur as near as possible to the time of maximum current.

An estimate for sheath velocity may also be obtained simply. Consider that part of the sheath next to the center electrode to be a disc of inner radius $r_i$, outer radius $r_s$, as shown in Figure 9.

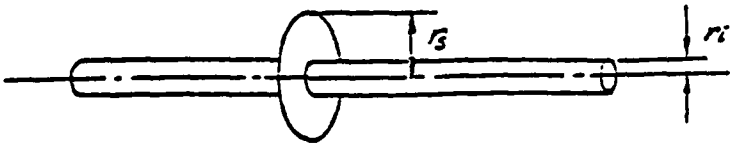


Figure 9. Geometry for Simple Snowplow Velocity Derivation.

Then we have

$$A = \pi(r_s^2 - r_i^2)$$

$$M = \rho_o A z$$

$$\frac{d}{dt}\left[M \frac{dz}{dt}\right] = \int_{r_i}^{r_s} p_m \, dA \tag{17}$$

Choose $r_s$ close to $r_i$ so that

$$\int_{r_i}^{r_s} p_m \, dA \to p_m^i \, A;$$

that is, the magnetic pressure is nearly uniform over the disc and may be obtained from $B_i$, the magnetic field at $r_i$.

Then we have

$$\rho_o A \frac{d}{dt}\left(z \frac{dz}{dt}\right) = p_m^i \, A \tag{18}$$

For constant velocity, $d^2z/dt^2 = 0$ and we have

$$\frac{dz}{dt} = v_s = \left(\frac{p_m^i}{\rho_o}\right)^{1/2} \tag{19}$$

Aside from a factor $\gamma^{1/2}$, this is in perfect analogy with the ordinary sound speed $c_s$:

$$c_s = \left(\frac{\gamma p_{th}}{\rho_o}\right)^{1/2} \tag{20}$$

where $p_{th} = nkT$ is thermal pressure.

(Coincidentally, Equation 20 is also that for an Alfven wave, a low frequency plasma wave propagating in a magnetized plasma with the propagation vector $\bar{k}$ perpendicular to the background magnetic field $\bar{B}_o$. The spatial orientation between $\bar{k}$ and $\bar{B}_o$ is preserved in our case but further resemblance is illusory because Alfven waves are defined for plasmas of uniform density and constant, uniform background field, $\bar{B}_o$.)

To obtain $v_s$ it is assumed that $d/dt\ v_s = 0$. Most measurements and calculations bear this out, but some indicate that z(t) more resembles a parabola than a straight line. Similar behavior is sometimes shown for L(t) during rundown.

This derivation assumes a disc normal to the accelerator axis (in fact, slight canting of the sheath in contact with the CE is sometimes observed), and B constant over the disc. However, due to $B \propto 1/r$, as $r_i$ decreases, $r_s$ will have to be closer to $r_i$ for the constant B assumption to be valid, and the sheath will be more bullet-shaped, decreasing axial mass accretion in the sheath and resulting in sheath acceleration near the center electrode. (Axial mass accretion is already decreased by centrifugal motion--due to electric fields, primarily inductive--of ions towards the OE, resulting in mass pileup at the OE, or through it in the case of a perforated or squirrel cage OE.) This departure from the usual cylindrical piston sheath shape also changes L calculations; Equation 1 has to be modified or replaced. One effect of $d/dt\ v_s \neq 0$ will be that sheath rundown times calculated from Equation 16 will be too long. Also, analysis assuming $\dot{L}$ constant during rundown will have to be modified. Two-dimensional snowplow theory offers improved modeling. Finally, if the sheath is accelerated, it is prone to the Rayleigh-Taylor instability.

2-D Snowplow Models

One-dimensional snowplow analysis as applied to rundown provides the voltage and pressure dependence of sheath velocity and $v_s(t)$, but little else. Two-dimensional snowplow models have been developed to provide time-dependent profiles of the sheath.

The first 2-D snowplow model, presented in Reference 38, was developed for a noncylindrical z-pinch designed to create a ball of plasma by starting off the sheath with indentations that would constrict the plasma during implosion, leaving a ball of plasma at the center. The model was later applied to model sheath profile development in a plasma focus.

The model is Lagrangian. The position of each point of the sheath is a function of the parameter $\lambda$. The position at time t of a point whose initial position is $\bar{R}(\lambda, t = 0)$ is given by $\bar{R}(\lambda,t)$. Sheath profile is then given by t = constant, and the trajectory of a particular point is given by $\lambda$ = constant. The mass of a sheath element given by $d\lambda$ is

$$dm = \rho \int_0^{\tau} 2\pi r \left| \frac{\partial \bar{R}}{\partial \lambda} \times \frac{\partial \bar{R}}{\partial t} \right| d\lambda \, dt \tag{21}$$

where $\rho$ is the fill gas mass density. The $\partial \bar{R}/\partial \tau_{\lambda}$ is the velocity of the point at $\lambda$.

The magnetic force on dm is

$$d\bar{f} = 2\pi r \left| \frac{\partial \bar{R}}{\partial \lambda} \right| d\lambda \, \frac{\mu_o}{2} j_s^2 \, \hat{n} \tag{22}$$

where $\hat{n}$ is a unit vector normal to the sheath, directed into the plasma and $j_s = I/2\pi r$ is the surface current density, with I the total current.

With the snowplow assumption, equating $d/dt(m\bar{v})$ to force (magnetic pressure over the area of the mass element, dm) we have for element $d\lambda$,

$$\frac{d}{dt} \left[ \frac{\partial \bar{R}}{\partial \lambda} \int_0^t r \left| \frac{\partial \bar{R}}{\partial \lambda} \times \frac{\partial R}{\partial t} \right| dt \right] = \frac{\mu_o}{8\pi^2 \rho} \left| \frac{\partial \bar{R}}{\partial t} \right| \frac{I^2}{r} \hat{n} \tag{23}$$

The current, I, may be specified from measurement, and the above equation solved numerically. Alternately, I may be calculated from the

circuit equation and a 2-D calculation of L(t) based on the sheath profile obtained from Equation 23. In this case the equation of motion and the circuit equation are coupled. Sheath profile evolution using the 2-D snowplow model of Reference 39 is shown in Figure 10.

Steady-State Fluid Models

The next step in sheath rundown modeling is to allow sheath structure. One example is a 2-D steady-state fluid model (Ref. 40). Here the fact that sheath velocity and profile are often nearly constant during rundown suggests the use of steady-state fluid equations. In a frame moving axially with the sheath velocity, equations are written for mass conservation, energy conservation and pressure balance at the interface between the sheath and the fill gas. The approximations are made that fill gas pressure is negligible compared to magnetic pressure at the sheath, fill gas enthalpy is negligible compared to $1/2\ v_s^2$, the enthalpy of gas in the layer is that of an ideal gas, and that sheath thickness at the center electrode is zero. With these assumptions and for $r > 1.2\ r_i$, analytical solutions for n and T are obtained, as shown in Figure 11. By neglecting the centrifugal term in the axial momentum conservation equation, analytical solutions are also obtained for sheath profile, particle velocity within the layer, mass areal density and layer thickness. Some of these results are also shown in Figure 11.

A similar approach is followed in Reference 41, though the solution of the resulting equations is done numerically and supported by experiment and a particle-in-cell computation.

2-D Plasma Fluid Codes

A representative 2-D DPF plasma fluid code is that written in Reference 42 for a fully ionized plasma with azimuthal symmetry. Similar, more recent, DPF computational work has been done in Reference 43. This type of code work is quite successful at predicting rundown behavior such as sheath velocity, but cannot model breakdown and lift-off or the final phases of collapse with much detail or accuracy. Also, luminosity and B sheath measurements indicate more complicated sheath structure than is shown in this computational work.

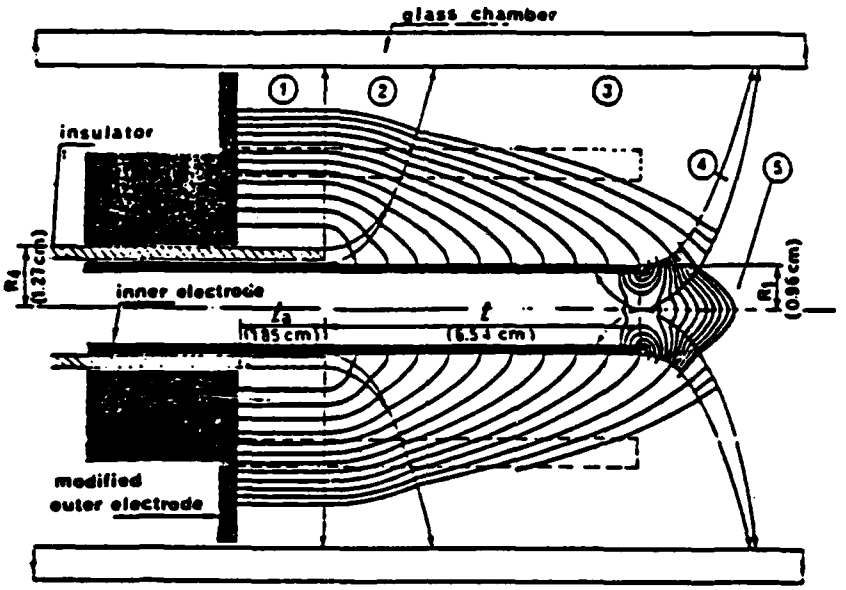


Figure 10. 2-D Snowplow Sheath Profile Development. (From Ref. 39).

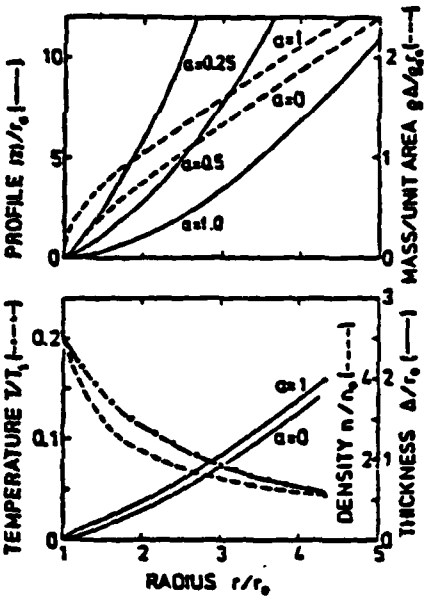


$$T_1 = \frac{p_m(r_o)}{n_o k}$$

$$a = \frac{p_m(r_o)}{\rho_o \mu^2}^{1/2}$$

$\Delta$ ~ sheath thickness

$p_m = p_o + \rho_o \mu^2 \cos^2$

$r_o$ ~ CE radius

$\rho_o$, $p_o$, $h_o$ ~ initial gas mass density, pressure, enthalpy

$\mu$ ~ sheath velocity

$n$ ~ particle number density

$k$ ~ Boltzmann constant

Figure 11. Steady-state Fluid Sheath Structure. (From Ref. 40).

This code is referred to as a two-fluid code. The usage is common but the term is misleading. It reflects common practice in MHD theory. Only one mass density is calculated and the conservation of mass and momentum equations use a single velocity, $\bar{v}$. This velocity is taken to be the ion velocity, approximately the center-of-mass velocity, and is also used in the ion thermal energy density equation. An electron velocity, $\bar{v}_e$, is calculated from the conduction current: $\bar{j} = ne(\bar{v} - \bar{v}_e)$, where n is the number density for either species (thus imposing quasi-neutrality). This velocity is used in the electron thermal energy density equation. Thus the model is single-fluid for mass and momentum calculations, but two-fluid for temperature, pressure, heat conductivity, heat flux and cyclotron frequency calculations.

In addition to solving the usual fluid equations of mass and momentum conservation, Faraday's law, Ampere's law (neglecting displacement current) and a generalized Ohm's law are also solved. Also, for each species, thermal energy densities, temperatures, pressures, heat conductivities, Hall parameters and heat fluxes are calculated.

The plasma within the computational space is coupled to an equivalent circuit of external capacitance and inductance; boundary and initial conditions are set and the calculation proceeds. Typical sheath structure results are shown in Figure 12.

Collapse and Focus

When the sheath reaches the end of the CE, its behavior is dominated by its own axial momentum and magnetic pressure. Axial momentum pushes it beyond the end of the CE. Magnetic pressure is normal to the sheath everywhere. These two effects produce the bulged, umbrella shape of collapse just after the sheath runs off the tip of the CE. This shape results in an (r,z) collapse. Final radial collapse velocities are typically ~ 50 cm/$\mu$s.

The collapse and pinch phases may be analyzed to some extent with linear z-pinch theory, though some differences between the focus collapse region and a classical linear z-pinch may be important. For

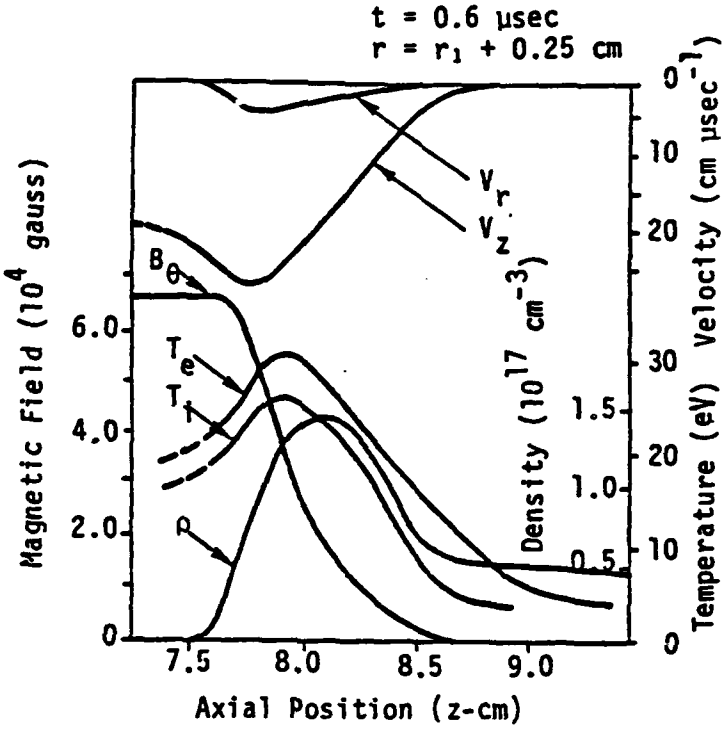


Figure 12. The 2-D Plasma Fluid Code Sheath Structure. (After Ref. 42.)

example, the curvature of the focus z-pinch results in (1) B field curvature and (2) a toothpaste squeezing of gas from either end of the pinch region. This B field curvature, which provides a $\bar{B} \times \nabla\bar{B}$ drift velocity, and the toothpaste mass flow have been suggested as mechanisms for the long immunity of the focus to disruption by the m = 0 instability (Ref. 7). With such differences in mind, some items of linear z-pinch theory are mentioned which are applicable to the focus z-pinch.

Linear z-pinch 1-D snowplow theory predicts radial bouncing of the sheath. The collapsing sheath is preceded by a shock which reflects on axis, heats the sheath and causes it to expand. The sheath then contracts and expands again, several times. This bouncing is observed experimentally in linear z-pinches, and some workers (Ref. 44) attribute focus $\dot{I}$ oscillations to bouncing. (While this is plausible, it is more likely that power cable reflection or resonant excitation of gun header structure is responsible. Such oscillations are evident in $\dot{I}$ and V waveforms (Ref. 11) They are attributed to gun header capacitance. With the power cable terminations limited oscillation is seen, though the sheath and compression dynamics may limit bouncing.) Though bouncing is theoretically predicted for classical z-pinches, no DPF computational work extends far enough in time beyond rundown calculations to show such behavior. In Reference 21, the calculation which begins with radial collapse, the pinched column undergoes expansion after attaining minimum radius. Such behavior may conceivably be interpreted as bouncing.

In snowplow linear z-pinch theory, resistivity due to a turbulent or cold sheath is neglected. With estimates of the time behavior of I and L during collapse it is possible to compute V = d/dt (IL) in order to obtain an estimate of the voltage at the gun header during pinch, if IR voltage drops are negligible. The current is usually measured directly. The inductance may be obtained from visible light photographs with the usual caution about interpretation of luminosity as current location. Lacking image-converter inductance estimates, one

may resort to snowplow theory or MHD-type calculations to provide such estimates.

It was found that the voltage spike normally associated with d/dt(IL) is too late in time to be due to collapse $\dot{L}$. It is suggested this V spike is due to IR drop, resulting from a large increase in resistivity caused by turbulent break-up of the pinch. It is also concluded that d/dt(IL) = 0, i.e., that magnetic flux is conserved during collapse. This cannot be true, of course, for significant plasma resistivity. This observation may be peculiar to high impedance banks or it may be that previous measurements have not had the temporal resolution to note this.

Linear z-pinch theory also predicts instability of the focus both during collapse and when maximum compression is attained. During collapse, the dynamic phase, the z-pinch is subject to the Rayleigh-Taylor instability. From linear theory, with a sharp plasma/magnetic field boundary, the growth rate for this instability is $\gamma = (ka)^{1/2}$ (Ref. 45, p. 249), where k is the wave number of the instability and a is the acceleration of the plasma/vacuum interface; shorter wavelengths have faster linear growth rates.

Rayleigh-Taylor analysis may be extended to include nonlinear effects* and a diffuse plasma/magnetic field boundary (Ref. 45, p. 48). Nonlinear analysis growth rates are wavelength- and time-dependent. For an exponentially decreasing plasma density of scale wave number K, linear theory gives a growth rate of $\gamma = [kKg/(k + K)]^{1/2}$.

During the static phase, when the column has a more or less constant radius, the focus is subject to various instabilities. In particular, the m = 0--sausage--instability is predicted to occur in a time $r_{min}/v_s$, where $r_{min}$ is the final collapse radius and $v_s$ is the ion sound speed. The m = 0 instability is unstable to all wavelengths.

---

*"A Model for the Saturation of the Hydro-Rayleigh-Taylor Instability," submitted for publication.

Typical m = 0 disruption times for the focus are on the order of a nanosecond. (More generally, hydromagnetic instabilities have growth rates about equal to the transit time of an ion traveling the distance of a wavelength of the perturbation. Thus short wavelength instabilities can grow quickly.) Since focuses typically last for ~ 100 ns, some stabilizing mechanism must be at work.

The m = 0 instability results from small perturbations in the column surface, presumably due to thermal fluctuations or pre-existing turbulence. A local contraction caused by such a perturbation results in locally increased magnetic pressure which enhances the contraction, increasing magnetic pressure and so on. The constriction squeezes plasma axially away from itself, causing bulging on either side of the constriction. This mass coupling flow with other constrictions leads to periodic spacing of the constrictions (Ref. 24).

Static pinch instabilities were first examined by Kruskal and Schwarzchild (Ref. 46) considering first-order perturbations of a sharp plasma-magnetic field interface. In this analysis an initial random noise level of perturbation of the column surface is written as a Fourier sum:

$$\sum_{m,k} A_{mk}\, e^{i(m\theta+kz)}$$

The growth of normal mode m,k is given by

$$\zeta = \zeta_0 e^{i(m\theta+kz)} e^{\omega t},$$

where $\omega(k)$ is given by the dispersion relation:

$$-\frac{\omega^2 r_0 \nu}{\alpha 2p}\,\frac{J_m(\alpha r_0)}{J'_m(\alpha r_0)} = 1 + \frac{m^2\, K_m(kr_0)}{kr_0\, K_m'(kr_0)} \qquad (24)$$

where $J_m$ and $K_m$ are Bessel functions, $r_o$ is pinch radius, $\nu$ is mass density, p is thermal pressure, $\gamma$ is the ratio of specific heats and $\alpha^2 = \omega^2\nu/\gamma p - k^2$.

It is commonly suggested that during collapse, ions are preferentially heated over electrons because the sheath moves as a whole; ion directed energy compared to electron directed energy will go as of the mass ratio. Charge separation will create a radial electric field which may enhance interspecies thermal equilibration. Assuming that collisions in the final phase of collapse transform directed energy into thermal energy, ultimate pinch temperature may be estimated and, thus, also thermal Bremsstrahlung spectrum. Thermal equilibration times between various species are, therefore, useful to know.

Some scientists measuring $T_e$ during collapse with laser scattering have found $T_e$ to be higher than $T_i$, suggesting an anomalous heating mechanism, such as a lower hybrid drift induced turbulence (Ref. 47). This evidence is taken as experimental justification for the inclusion of vorticity terms in computational work (Ref. 21). If turbulence dominates energy transfer during collapse, previous models providing temperture estimates may have to be revised or abandoned.

It is common in recent DPF literature to divide the focus process into several phases. First is the compression phase, during which the sheath collapses radially. The time of maximum compression occurs when the column attains minimum radius, ~ 1 mm, and maximum plasma density, ~ $10^{19}$ $cm^{-3}$. Some time later the m = 0 instability begins and the column later exhibits severe, periodic constriction and finally breaks up. Between maximum compression and m = 0 onset is the intermediate phase, of duration $\tau_{ip}$. During this time the column expands slightly and plasma density decreases slightly. Also during the intermediate phase, electrons and ions of the pinch plasma have time to exchange energy. The column may develop surface ripples, but it remains well confined. The intermediate phase is anomalously long; linear theory predicts breakup by the m = 0 instability within $\lesssim$ 10 ns, whereas $\tau_{ip}$ is 100 ns or more for high energy banks. The onset of the m = 0 instability signals the start of the late phase.

For higher energy devices, (100 kJ to 1 MJ) there is neutron production during the intermediate phase. Thermonuclear reactions account for only a small fraction of this neutron production, based on inferredor observed plasma densities and temperatures. The main neutron production mechanism is presumably due to acceleration of ions to high energies. Also, $\tau_{ip}$ is found to increase with pinch current: $\tau_{ip} \sim I_p^{3/2}$. And there is a current threshold, 500 kA, observed experimentally (Ref. 48) and predicted theoretically (Ref. 21), below which neutron production does not occur during the intermediate phase. These two items suggest that breakeven may be obtained by beam processes for pinch currents of ~ 20 MA, with $\tau_{ip}$ extrapolated to be 10 $\mu$s.

While some x rays and neutrons are produced by thermonuclear processes, there is evidence that beam-target and beam-beam interactions usually dominate, although this dominance is pressure-dependent. The most convincing pieces of evidence for beam interactions are the following: (1) For positive CE there appear high energy, high current electron pulses directed axially towards the CE and high energy, high-current ion pulses directed axially away from the CE. (2) X-ray production after focus breakup from the region of the CE tip is often characteristic of electron bombardment of the CE tip material. (3) Anisotropy of x ray and neutron production typical of beam processes is observed.

How such large accelerating fields arise to produce these beams remains somewhat speculative. Various models predict generation of electric fields to account for some aspects of neutron, x ray and particle beam measurements. The simplest and earliest theory suggested that the E fields are due to a large $\dot{L}$ created by m = 0 constriction of the column. A more recent theory has been offered (Ref. 21) based on computational results taking turbulence into account.

In the early days of plasma focus research, the sheath and focus were thought to have simple structure, to consist of well defined,

nonturbulent layers. This is probably unreasonable in view of the large magnetic Reynolds numbers typical of rundown and collapse. Large magnetic (or fluid) Reynolds numbers usually result in turbulent flow. In recent years, turbulence and other irregularities have been experimentally observed. Laser beams were scattered from the front of the sheath during rundown and from the region of the collapsing sheath (Ref. 49). Turbulence was observed in both cases. More recently, 100 ps exposure Schlieren photographs were obtained during collapse showing sheath rippling--clear evidence of instability, presumably the Rayleigh-Taylor--long before maximum compression. Finally, calculations of the decay time of electric fields generated by the m = 0 instability are much too short for the observed times of neutron production (presumably by beam processes). With evidence such as this in mind, turbulence was included via fluid and current vorticity terms, in a plasma fluid computational model to see if stochastic fields accelerating ions could account for observed neutron production. Fluid velocity is defined as $\bar{\zeta} = \nabla \times \bar{v}$, where $\bar{v}$ is fluid velocity. Current vorticity is $\bar{\zeta}_e = \nabla \times \bar{j}$. The degree of turbulence is determined by $\bar{\zeta}$, $\bar{\zeta}_e$ and the fluid and magnetic Reynolds numbers.

The computation begins at the start of compression, using initial values obtained from measurement of the Stuttgart POSEIDON plasma focus with parameters of 60 kV, 280 kJ (Ref. 21). The maximum pinch current at the start of compression is 2.1 MA, sheath temperature is 5 eV, sheath density is $10^{17}$ cm$^{-3}$ and sheath radius is 6.5 cm. (We point out that most measurements indicate a rundown sheath electron temperature of 30 to 50 eV.) At maximum compression, with vorticity terms giving 3rise to E and B fields, the density is $1.7 \times 10^{19}$ cm$^{-3}$, $T_i$ = 770 eV, $T_e$ = 2.2 keV, E = 24 kV/cm, B = .74 Mgauss, $r_{min}$ = 3.5 mm, $\zeta = 10^{10}$ s$^{-1}$.

In the intermediate phase, current filaments form. In these filaments the current density is much higher than in the surrounding plasma. Filamentation is probably due to m > 1 instabilities. Also a fluting instability occurs which is damped out just before m = 0 onset. And wave packets form into slowly decaying quasi-solitons which travel along the current filaments. In the intermediate phase, E

fields are ~ 300 kV/cm and B fields are ~ 5 Mgauss in the quasi-solitons, the current filaments and the surrounding plasma. The density and temperature in the quasi-solitons are higher--2 x $10^{19}$ $cm^{-3}$, 4.2 keV--than in the surrounding plasma--9 x $10^{15}$ $cm^{-3}$, 820 eV.

The m = 0 instability, which lasts ~ 10 to 20 ns, is damped by high vorticity. As the m = 0 instability dies off, turbulence packets--solitons--and vortices develop. Towards the end of the intermediate phase, $\zeta$ drops rapidly, the quasi-solitons disappear and current filamentation is smoothed out. The solitons move along the cylinder axis and combine. During this late phase, $\zeta$, E, B, T and density decrease in the surrounding plasma. In the solitons these quantities remain high enough for large neutron production, reaching peak values of 1.3 x $10^{20}$ $cm^{-3}$, 10.3 keV, 26 MV/cm, 114 Mgauss, 6.5 x $10^{9}$ $s^{-1}$. The solitons last for some 160 ns, then decay within 5 ns, bringing an end to field-accelerated ions.

This model accounts for the anomalous life-time of the intermediate phase and during the late phase. Further, from $\tau_{ip} \sim I_p^{3/2}$ it is seen that for lower current devices the intermediate phase is so short that neither quasi-solitons, current filamentation or neutron production occurs. Yet the late phase development of turbulence packet solitons can account for neutron production in both low and high current devices. Finally, it is seen that for higher current devices neutron production in the intermediate phase dominates that in the late phase and at the same time $\tau_{ip} \sim I_p^{3/2}$. The end result is that neutron yield scales as $I_p^4$ and a breakeven plasma focus device seems possible not on the basis of thermonuclear yield but on the basis of turbulence-derived neutron production.

X-ray Production

X-rays are usually emitted from the region of the focus and the CE face in usually one or two (sometimes more) bursts of $\leq$ 100 ns duration each. It is often possible to correlate these pulses, via I signals and image converters photos, with pinch compression or recompression thermal Bremsstrahlung. The later pulse(s) is (are) usually due to electrons accelerated into the CE by pinch break-up electric fields.

The total X-ray energy output of devices of $\lesssim$ 30 kJ is typically $\lesssim$ 10 J.

Pinch thermal Bremsstrahlung radiation is produced by the (more or less) thermalized electrons in the pinch column and may often be used as an electron temperature diagnostic. The electron beam radiation is sometimes typical of x-ray tube emission (Ref.19) with line radiation characteristic of the CE face material. From electron beam x-ray radiation, the character of the electron beam(s) may be determined. In higher energy devices, x-ray detectors viewing the focus only--not the CE face--sometimes show copper contamination of the focus (Ref. 50) (for copper CE face). This may complicate the determination of pinch electron temperature from continuum x-ray measurements. On the other hand, the presence of line radiation of highly-stripped high Z ions (either CE face ions or deliberately introduced contaminants) may provide temperature information, assuming the high z ions are in thermodynamic equilibrium with the ions of interest, usually deuterium ions. Finally, some x-ray emission may result from acceleration due to turbulence generated electric fields. Such fields are discussed in the paragraphs on Collapse and Focus.

In general, radiation from the focus proper consists of (1) bound-bound de-excitation radiation, (2) free-bound recombination radiation, and (3) free-free thermal Bremsstrahlung radiation. For low Z fill gases, ions are completely stripped and, with no copper or other contamination, line and recombination radiation are negligible. In this case, if electron self-collision rates are high enough for electron kinetic thermodynamic equilibrium to obtain during the pinch, electron temperature can be inferred from the bremsstrahlung spectrum.

Temperature Measurement from Thermal Bremsstrahlung

The most narrow definition of kinetic thermodynamic equilibrium in a fully-ionized plasma is that charged particles of species $\alpha$ obey a Maxwellian velocity distribution in some direction $\hat{i}$. We may then define a kinetic temperature, $T_\alpha^i$, which allows for the frequent

situation in plasma where electrons exchange little kinetic energy with ions, but each species separately maintains Maxwellian velocity distributions. This definition also permits directionality of transport properties often introduced by the presence of magnetic or electric fields in the plasma. The more familiar kinetic temperature is that of a molecular gas consisting of one particle species and complete space isotropy.

Kinetic thermodynamic equilibrium does not guarantee radiative thermodynamic equilibrium. A body of plasma with a given kinetic temperature typically does not radiate as a blackbody at that temperature. The requirement for radiative thermodynamic equilibrium is that the plasma be in equilibrium with its radiation field. This means that the optical depth in the plasma at wavelengths where the plasma radiates most strongly is much less than the scale length of the plasma. This is equivalent to saying that radiation emitted by some part of the plasma is absorbed by some other part. Assuming complete ionization (only free-free transitions), radiation is emitted from the plasma by the Bremsstrahlung of charged particles (electrons) moving with the velocity distribution determined by the plasma's kinetic temperature and subject to short- and long-range collisions (with primarily ions). Absorption is by inverse Bremsstrahlung. If a self-absorbing plasma is not in equilibrium with its radiation field, then parts of it will heat up or cool down, disturbing kinetic thermodynamic equilibrium. A plasma may be in equilibrium with its radiation field without being in radiative thermodynamic equilibrium with its surroundings. If the optical depth is much larger than the plasma scale length, no radiation will be absorbed by the plasma and its emission will be well described by the Bremsstrahlung spectrum characteristic of the kinetic temperature.

The Bremsstrahlung radiation power density, assuming complete plasma ionization, no plasma radiative self-absorption, is

$$P_r = 0.54 \times 10^{-30} Z^2 n_e^2 T_e^{1/2} \frac{J}{s\text{-}cm^3} \qquad (25)$$

For a hydrogenic plasma, $Z = 1$, $n_e = n_i$. Due to $Z^2$ dependence of $P_r$, small amounts of Z ions can greatly increase the radiated power density. Impurities are also important for radiation in a partially ionized plasma. Recombination radiation goes as $Z^4$ and line radiation goes as $Z^6$.

Objectives of High Voltage Operation

Plasma focus operation at high voltage has two main objectives. First, the important parameter in neutron scaling has been found for a wide range of device configurations, currents and energies to be discharge current during pinch. This scaling is shown in Figure 13 and is commonly referred to as Bernard scaling. The efficiency of a fusion reactor may be taken as fusion energy output energy input. For most DPF devices input energy is stored in a capacitor bank; a measure of plasma focus fusion energy efficiency is neutron output/capacitor bank energy. It is, therefore, of interest to maximize discharge current during pinch for given capacitor bank energy. For fixed bank energy it is generally found that higher voltage results in higher discharge current just before pinch. Higher voltage banks generally also have higher impedance, which reduces load effects on discharge current, thereby, maximizing current during pinch. Therefore, consider current optimization in these two regions of time. (It may seem at first that the means of maximizing current just before pinch and during pinch is the same because in both cases $\dot{L}/Z_o$ is to be reduced. However, the dependence of $I_{sc}$ on $Z_o$ and the complex electrical nature of collapse warrant at least the attempt to make this distinction.)

Secondly, it has been found that higher voltage plasma focuses create sheaths which differ from those created by lower voltage devices. The energy which goes into sheath formation is higher than that of lower voltage devices. Therefore, changes are expected in sheath thickness, temperature, conductivity and possible resulting changes in the focus--smaller dimensions, higher temperatures and shorter lifetimes. High voltage plasma focus operation may thus represent a new and interesting development in plasma focus operation.

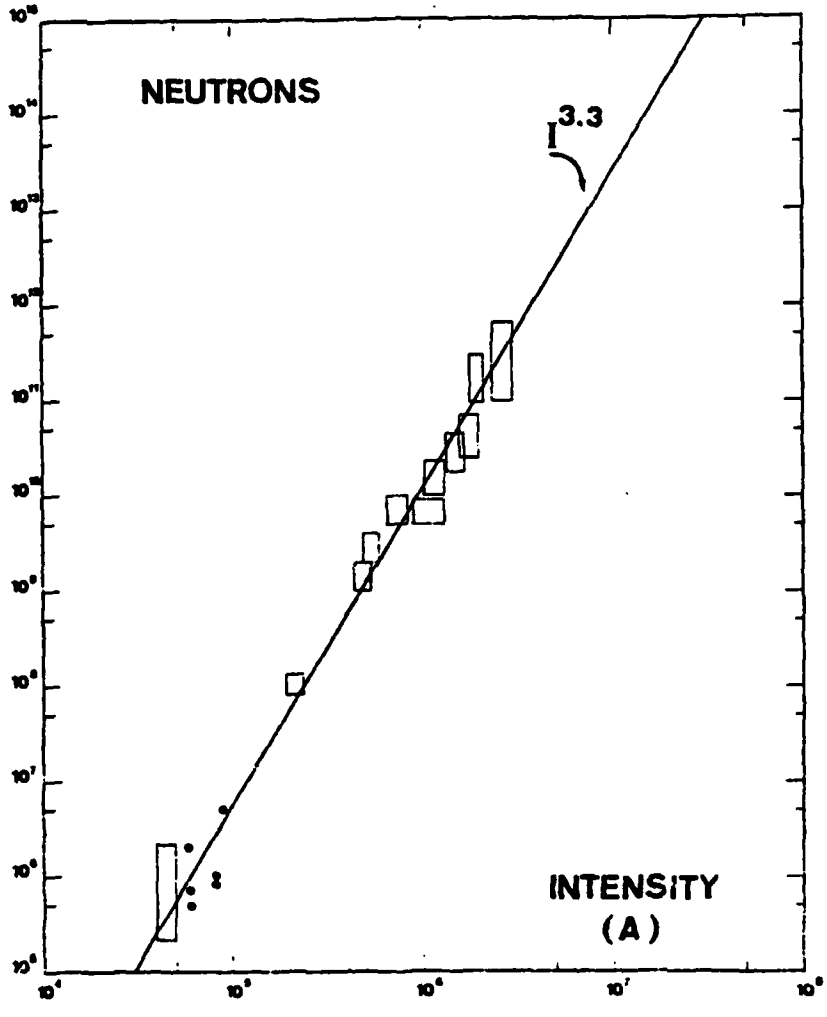


Figure 13. Bernard Scaling of Neutron Yield with Peak Current. (From Ref. 51).

## Current Optimization

### Maximizing Current Just before Pinch

The analysis of the plasma focus operation showed that $I_p/I_{sc}$ is a monotonically decreasing function of $\dot{L}/Z_o$, i.e.,

$$I_p = I_{sc} f\left(\frac{\dot{L}}{Z_o}\right) \tag{26}$$

where $f(\dot{L}/Z_o)$ is as indicated in Figure 36.

Also, $I_{sc} = \frac{V_o}{Z_o}$, so that

$$I_p = V_o \frac{f\left(\frac{\dot{L}}{Z_o}\right)}{Z_o} \tag{27}$$

It might be naively assumed that merely increasing $V_o$ would increase $I_p$. But note that neither $\dot{L}$ nor $Z_o$ is independent of $V_o$. The $\dot{L}$ is only weakly dependent on $V_o$. As found in snowplow theory, and verified experimentally, $v_s$ (which is proportional to $\dot{L}$ during rundown) goes as $V_o^{1/2}$ (more specifically as the square root of the voltage across the sheath). Experimentally, $v_s$ is found to lie in the 10 to 15 cm/μs range, with 20 cm/μs a practical upper limit, so that $\dot{L}$ during rundown is a weak function of $V_o$. (During collapse, however, $\dot{L}$ behaves quite differently.)

As $V_o$ is increased, path lengths in various parts of the system must be increased to avoid electrical breakdown. This increases both system $\dot{L}$ and $Z_o$. The dependence of $L_o$ on $V_o$ cannot be solved precisely; a simplifying assumption may be made about this dependence.

Decker has assumed that $V_0/L_0$ is approximately constant, which is to say that $\dot{I}_0$ is constant. A survey of $\dot{I}_0$ values for various plasma focus devices suggests that this is not a bad assumption. However, $\dot{I}_0$ reflects not merely physical law but also the cleverness of device designers.

To examine the dependence of $I_p$ on $V_0$, it is convenient to use defining relations in the plasma focus operation paragraph to rewrite Equation (27) as

$$I_p = \beta V_0 \, f(\beta \dot{L}) \tag{28}$$

where

$$\beta = \left(\frac{2W\dot{I}_0}{V_0}\right)^{1/2} \frac{1}{V_0}$$

For fusion energy efficiency comparison, W is fixed, and, as mentioned, $\dot{L}$ is nearly constant during rundown. Finally, with Decker's assumption, we set $\dot{I}_0$ constant. To determine $I_p(V_0)$, use values typical of the device: $\dot{L}$ = 40 mΩ, W = 20 kJ, $\dot{I}_0 = 1 \times 10^{12}$ A/s. These These values give the curve shown in Figure 14. This graph indicates that the optimum voltage for these values of W, $\dot{L}$, and $\dot{I}$ will be in the 60 to 70 kV range.

This analysis is at least heuristically useful, although the idea of constant $\dot{I}_0$ is doubtful. But the trend is clear: operation in the voltage ranges typical of conventional plasma focus devices--20 to 40 kV--results in poor current optimization before pinch time; higher voltages generally result in better current optimization before pinch time. But current optimization during the pinch must also be considered.

Minimizing Current Depression during Pinch

Aside from the difficulties mentioned, the analysis of plasma focus has the serious limitation of ignoring changes in current due to

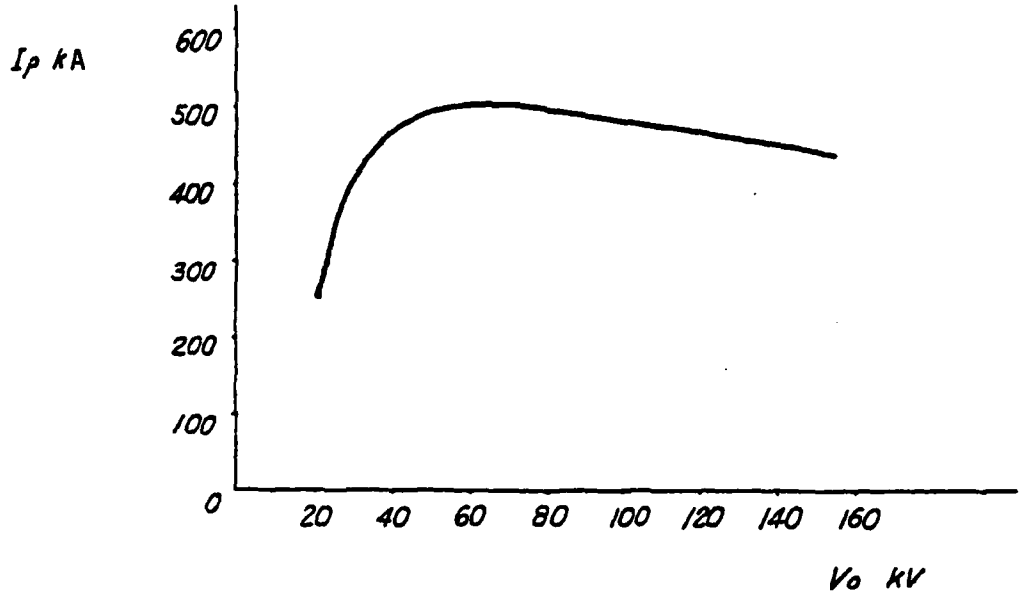


Figure 14. $I_p$ as a Function of $V_o$. $\dot{L}$ = 40 mΩ. W = 20 kj. $\dot{I}_o$ = 1 x $10^{12}$ A/s.

the large changes in inductance ($\geq$ several hundred m$\Omega$) which occur during collapse. There is also a large $\dot{L}$ associated with the inverse pinch. A high $Z_0$ bank will suffer less current depression at pinch time than a low $Z_0$ bank. Thus a larger fraction of $I_{sc}$ will occur during the pinch for a high $Z_0$ bank. Typical variation of $\dot{L}$ is shown in Figure 15a, along with bank impedance for our high $Z_0$, high $V_0$ bank. As can be seen from this graph, for conventional banks the load limits the current. For a high $Z_0$ bank, the current is largely independent of the load except during the earliest part of the inverse pinch stage and the final part of collapse. In Figure 15b are plotted impedances for several plasma focus banks.

High impedance is a natural consequence of high voltage operation. From $W = 1/2\ CV_0^2$, we see that for fixed energy, higher voltage reduces capacitance, which increases bank impedance.

It is desirable to have the large bank impedance realizable with a higher voltage bank. Yet there is a limitation to increasing bank impedance: $I_{sc}$ decreases with large $Z_0$. This effect is treated in the analysis of plasma focus for constant $\dot{L}$ but not for a variable $\dot{L}$ due to inverse pinch and collapse. Further, collapse is strongly coupled to the bank; using a prescribed, non-self-consistent L(t) to determine current depression is unreasonable: analytic solutions during collapse are inappropriate or nonexistent. Numerical MHD solutions are a possibility here because they can predict, with some accuracy, important plasma parameters, such as sheath density, temperature, thickness and conductivity from rundown to maximum compression, permitting reasonable current optimization. The MHD calculations for this device are not yet available, however, Figure 16 presents Decker's MHD calculations for high and low voltage plasma focus devices. Here $\dot{I}_0$ is not constant but total system inductance is. Again, the advantages of higher voltage operation are indicated at least qualitatively.

Usefulness of Current Optimization Theory

The theory of discharge current does provide some basis for higher voltage operation but is somewhat simplistic.

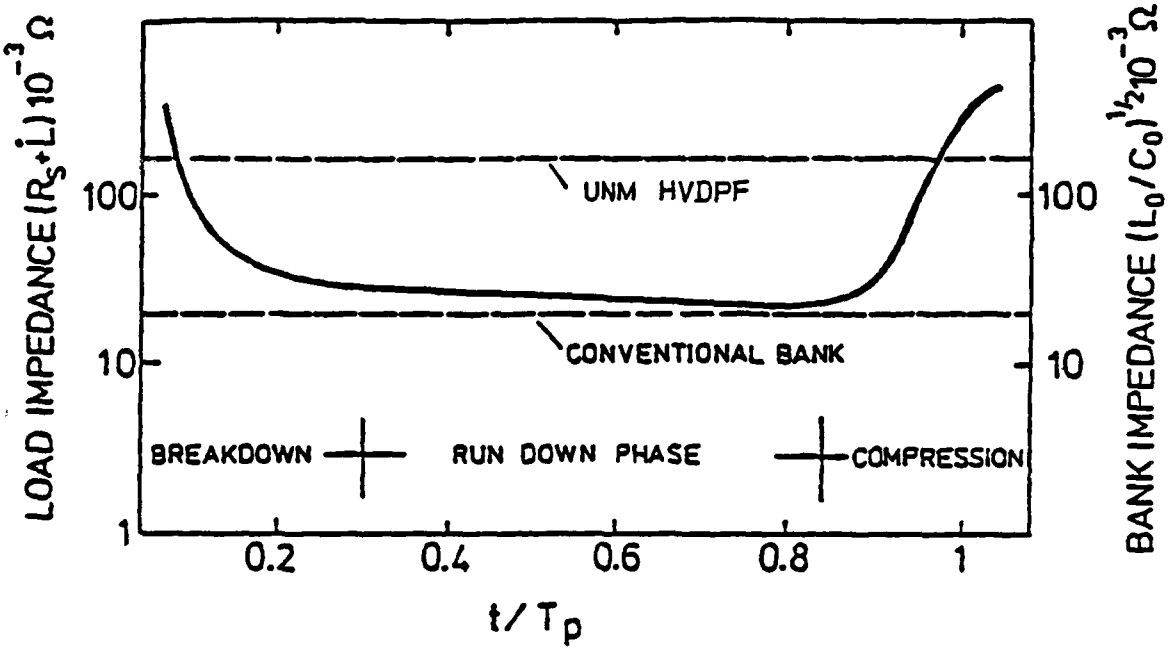


Figure 15a. Typical DPF Load Impedance as a Function of Normalized Time. (From Reference 12).

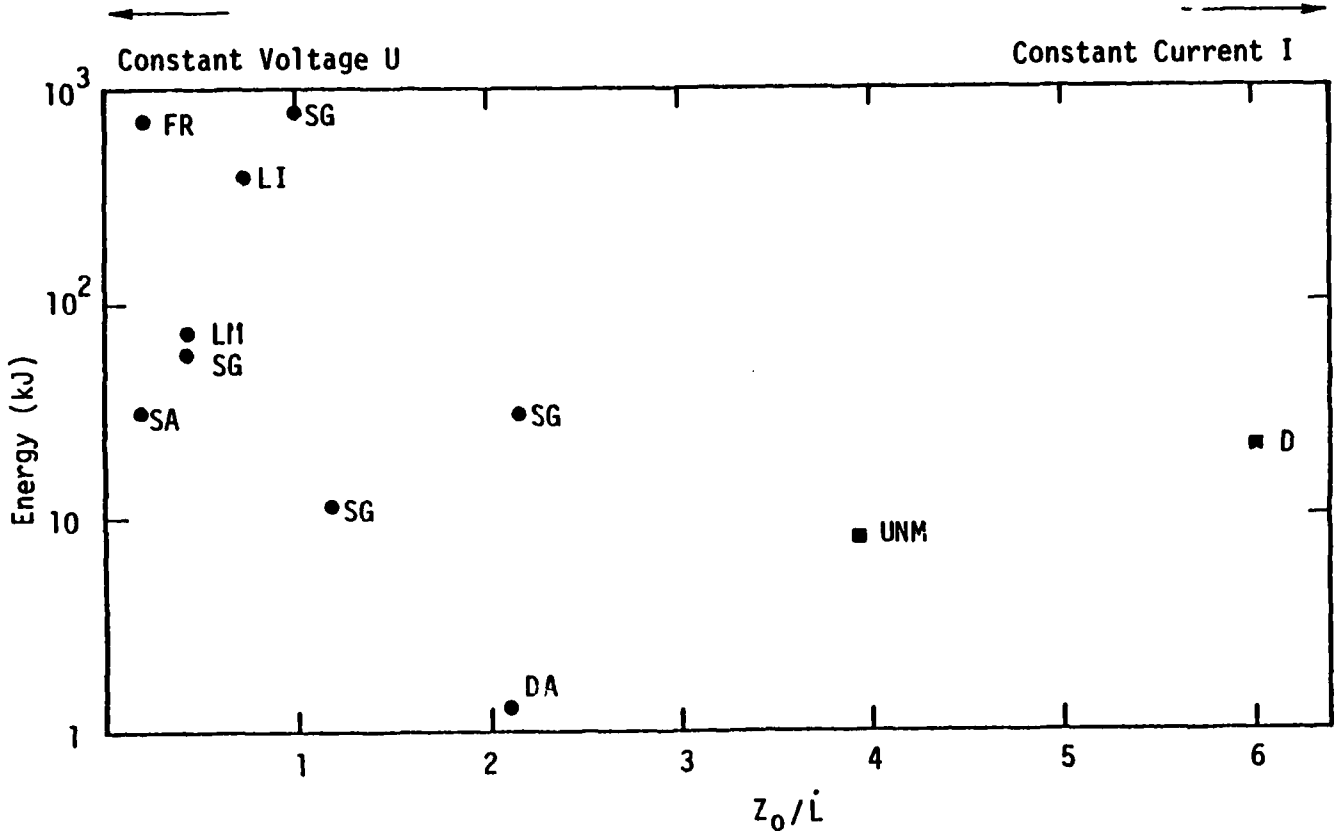


Figure 15b. Energy of Several Plasma Focus Devices versus Normalized Impedance.

(DA: Darmstadt, FR: Frascati, LI: Limeil, LM: Livermore, SA: Sandia, SG: Stuttgart, D: Dusseldorf, UNM: UNM). After reference 38.

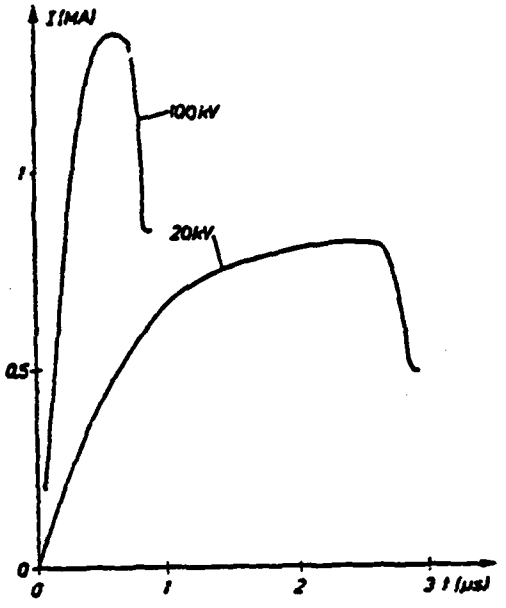


Figure 16. Comparison of Currents versus Time Obtained by MHD Calculations for Two Bank Voltages. Energy of bank--45 kJ. External inductance--25 nH. (After Ref. 11).

The validity of Bernard scaling for a variety of devices (both DPFs and linear z-pinches) is impressive and can justify the pursuit of current optimization for maximum neutron yield in regions of current where Bernard scaling applies or is expected to apply. But this simple law obscures the complex physics occurring in the focus. Further, the concept of current optimization requires clarification.

Based on Bernard scaling, one often tries to maximize total current in the device just before pinch. But this current is not always contained entirely in the pinch. In the case of insulator leakage current and/or restrike, current is diverted from the pinch. It is often suggested that current scaling should be based on current in the pinch only, though measurement of this current requires measurement of other possible current paths, such as leakage and restrike currents.

Aside from this problem--how is energy optimally used during pinch. The virtue of $Z_0 >> \dot{L}$ has been cited saying this minimizes load domination of current during pinch and this is beneficial; Decker discusses current stabilization of the pinch. But if the main interest is in fusion produced only by a thermal plasma (no beam interactions or turbulence considered), it is conceivable that maximum thermonuclear neutron yield will be obtained by an implosion of the plasma column with a prescribed current waveform. This is in analogy to the tailored laser pulses suggested for optimum neutron yield from deuterium-tritium pellets in inertial confinement fusion schemes. In this case, current stabilization may be a drawback.

There also is the question of energy transfer. During the pinch, energy is extracted from and through the volume of the accelerator behind the pinch, where magnetic energy is stored, and from the capacitor bank, where electrostatic energy is stored. The rate of energy transfer through the accelerator may be calculated by considering the region behind the pinch to be a coaxial transmission line comprised of the two electrodes and the (magnetized, low-density, at least partially-ionized) material between them. Indications are that energy

transfer from the capacitor bank is much slower than through the coaxial volume. If the situation is such that a short-lived pinch is produced, it may be that only energy extraction from the accelerator volume is important. In this case it would be beneficial to increase the inductance of that coaxial volume (hence, increasing L, in contrast to current optimization arguments) by increasing the rundown length and/or the ratio of elctrode radii.

All these details have been thought about but not always in depth because the pinch process is not sufficiently understood. It, therefore, seems unwarranted to spend too much effort on current optimization theory. The theory is mainly of heuristic and qualitative value. The clearest proof of current optimization at high voltage is to compare currents for devices of equal energy but different voltages. If neutron yield is of primary interest, one should compare neutron yields for two such devices. Most interesting, however, is to try to unmderstand plasma focus operation so that neutron yield may be enhanced by control fo the focus neutron production mechanisms.

## 2. THE UNM HVDPF--DESIGN, CONSTRUCTIOHN AND OPERATION

Given the advantages of high voltage plasma focus operation cited earlier in this report, it was decided to assemble six 60-kV, 1.85-μfd capacitors, obtained from the LANL Scyllac Theta Pinch Experiment, in a single-stage Marx configuration to power a 120-kV, 20-kJ plasma focus. The basic circuit of this configuration is shown in Figure 17, along with bank design characteristics. This design permits high-voltage plasma focus operation at a modest energy capable of significant--300 - 500 kA--pinch currents, with a possible view to operating at similar voltages but much higher bank energies available at nearby banks, once the modest energy system is thoroughly studied. At the Air Force Weapons Laboratory, the Shiva X-Ray Simulation Facility has two such 120 kV banks, one at 200 kJ, the second at 9 MJ. As mentioned previously, some sacrifice of the low energy, high voltage bank benefits of current optimization would occur in going to a higher energy bank at the same voltage.

The major considerations in the design, construction and operation of a plasma focus system are: inductance, corona and breakdown, magnetic pressure, power flow, electromagnetic noise and plasma purity. In the plasma focus paragraph the general importance of each of these areas is considered. Each system component is discussed, indicating where major considerations affected the choice, design or construction of each component. The results of short-circuit tests are also presented, which are logically the first tests to be performed when checking out a new pulse power system.

### General Considerations

#### Inductance

The general importance of minimizing system inductance to obtain maximum current is shown by equating electrostatic energy stored in the capacitor bank to magnetostatic energy stored in the inductance of the system.

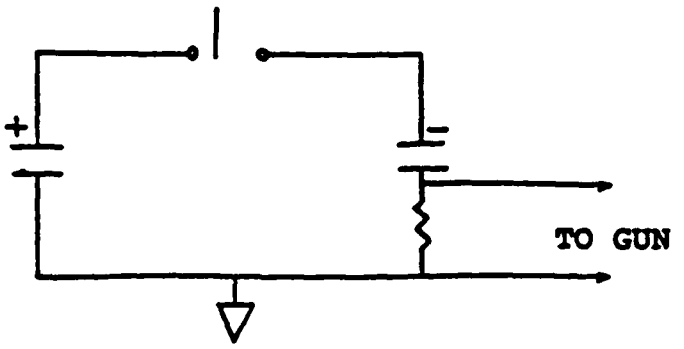


| | | |
|---|---|---|
| +Bank | 3 Scyllac Capacitors | 60 kV, 1.85 μfd ea |
| -Bank | 3 Scyllac Capacitors | 60 kV, 1.85 μfd ea |
| Switch | Maxwell Rail Gap | 40100 |
| Trigger | 8-Stage μMarx<br>120 kV, 20 ns Rise | LANL Design |

DESIGN SPECIFICATIONS

| | |
|---|---|
| Bank Energy | 20 kJ max |
| Bank Voltage | 120 kV max |
| Bank Rise Time | 850 ns |
| Initial Current Rise | $1.2 \times 10^{12}$ A/s max |
| Bank Impedance | 200 mΩ |
| Initial Inductance | 100 nH |
| Bank Capacitance | 2.77 μfd |
| Short-circuit Current | 600 kA max |

Figure 17. Basic HVDPF Bank Circuit and System Design Specifications.

$$\frac{1}{2} C V_o^2 = \frac{1}{2} L I_{sc}^2 \qquad (29)$$

This, of course, is a simplistic approach in view of the current optimization analysis, but it is generally a good current optimization rule to observe in the initial design stages. System inductance also influences initial current rise.

$$\dot{I}_o = \frac{V_o}{L_o} \qquad (30)$$

$\dot{I}_o$ is of interest in the early stages of sheath formation.

Generally, minimizing inductance means minimizing volumes, the two most common of interest being cylindrical and rectangular. Also of interest is the inductance of a cylindrical conductor over a plane return conductor. The inductances for these geometries are given in Figure 18.

Inductance may be reduced by placing inductive elements in parallel. This is part of the reason this system has so many cables in parallel. (This also reduces the current flowing in each cable and permits more uniform power flow, if desired, by proper cable distribution.) The rail-gap switch also exploits this principle. By placing many inductive plasma channels in parallel, the total inductance of the switch is reduced.

A final guiding principle involving inductance is that in a pulse system current will flow in the lowest inductance mode, if the resistances of various alternate paths are negligible. This follows from simple circuit theory--rise time in an LCR circuit goes as L/R. This principle is usually of great use in deciding where current will flow in a pulsed system.

Corona and Breakdown

Attempts to minimize inductance generally bring conductors at different potentials close together, increasing the risk of corona and

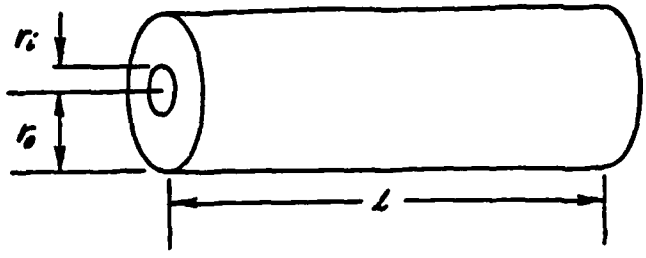


a. $L = 2\,\ell \ln \frac{r_o}{r_i}$ nH

$\ell \sim$ cm

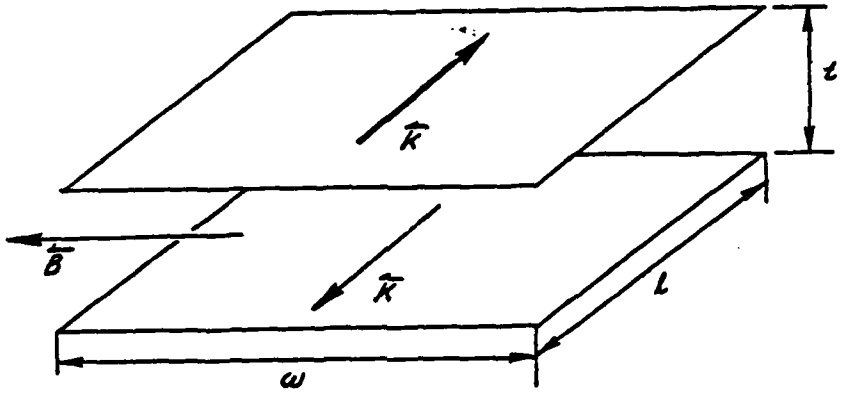


b. $L = 4\pi \frac{\ell t}{w}$ nH

$\ell$, t, w $\sim$ cm

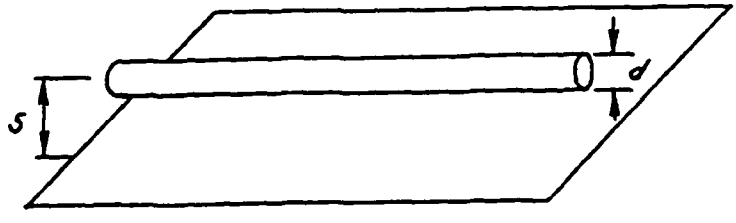


c. $L = 4 \cosh^{-1} \frac{2s}{d}$ $\frac{nH}{cm}$

Figure 18. Inductance Expressions for Three Common Experimental Geometries.

breakdown. The primary methods of preventing breakdown are (1) increasing breakdown lengths, (2) using insulators, and (3) electric flux control.

The first remedy is simple. If breakdown occurs between two points, increasing the length the spark must travel to initiate breakdown will reduce the probability of breakdown. This may be done by (1) moving the breakdown points further away from each other, or (2) placing material of high dielectric strength between the breakdown points, so the spark must find a longer path to initiate breakdown. Finally, breakdown is usually preceded for some time by corona, in which field strength near some conductor ionizes air--as evidenced by crackling, whizzing, frying sounds and purplish photo-de-excitation--but without sufficient ionization to lead to breakdown. Clearly, reduction of corona will reduce the likelihood of breakdown. Corona can be reduced by immersion in a high dielectric strength liquid (oil, freon, or pure water) or gas (dry air or $SF_6$) or by flux control, which is field reduction by eliminating physical singularities (points, edges) where electric fields are high. Flux control means breaking edges wherever high fields might occur. Edges with 1/8-in radius are typical broken edges. All of these methods are often used in various parts of a typical pulse power experiment. Inductance minimization often determines the choice of method.

Magnetic Pressure

Magnetic pressure is the pressure on a surface current of finite width due to a magnetic field, and is a form of the magnetic component of the Lorentz force. There are three types of magnetic pressure common in plasma experiments. (1) In the first type, the magnetic field producing the magnetic pressure is created by a current whose return isthe current the field acts upon. Two examples of this type of magnetic pressure are shown in Figure 19a. (2) Magnetic pressure also occurs when a time-varying magnetic field impinges upon a conductor. If the conductor's conductivity and the scale length of the incident B field are such that the magnetic diffusion time is long compared to the time scale of the field, the field will not penetrate the conductor.

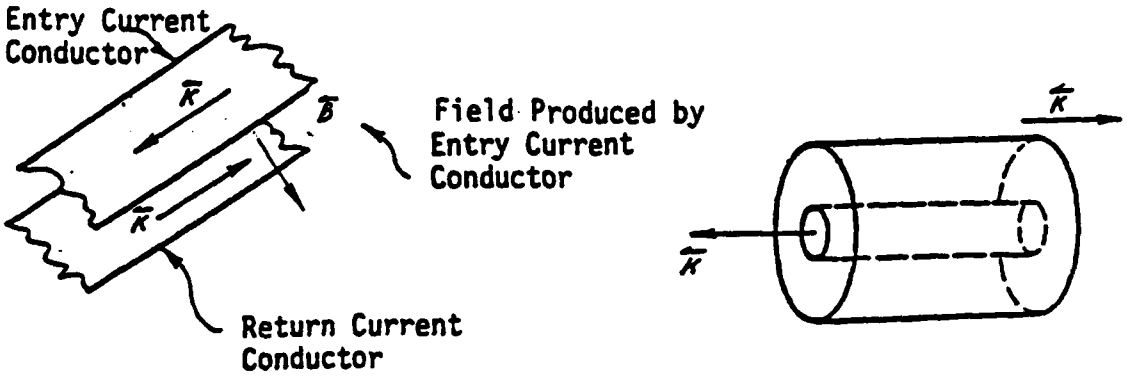


$\bar{K} \times \bar{B}$ on Return Conductor Tries To Move It Away from Entry Conductor .

(i) Strip Line Geometry (ii) Coaxial Geometry

(a) Type 1 Magnetic Pressure. Field of Entry Current Acts on Return Current.

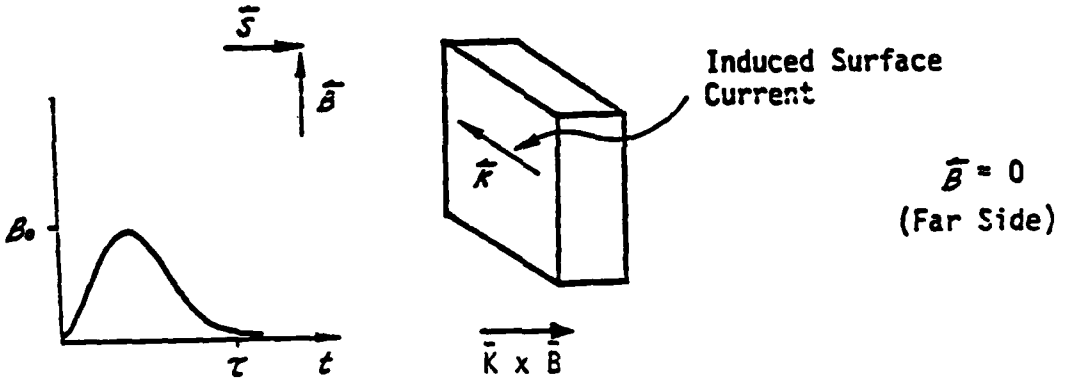


(b) Type 2 Magnetic Pressure. $\bar{B}$ Pulse Impinges on Conductor.

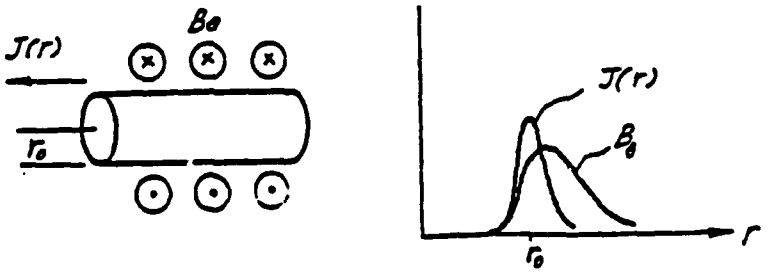


(c) Type 3 Magnetic Pressure. Self Pinch Magnetic Pressure.

Figure 19. Three Types of Magnetic Pressure.

Equivalently, by Faraday's law, a current is induced on the conductor's surface which cancels the field on the far side of the conductor. In this case, the magnetic field produces a pressure on the current it induces. This type of magnetic pressure is shown in Figure 19b. (3) Finally, magnetic pressure may result from interaction of the field produced by a current with that same current. This is the case in both z- and theta-pinches. Magnetic pressure is a particularly useful concept for these examples because it may be equated to the magnetic field energy density--$B^2/8\pi$. The equilibrium z-pinch radius may be determined by equating magnetic pressure at the surface of the magnetically-confined plasma column to the thermal pressure inside the column (Fig. 19c).

In the case of a metallic conductor, currents are electron currents and the magnetic pressure on the electrons is transferred to the bulk of the metal by collisions. Deformation of metal in this manner iscalled magneforming and is a recognized industrial metal forming technique. If the conductor is a plasma, the plasma may be formed (subjectto various instabilities) by magnetic pressure. Here electrons are usually the main current carriers, with ions being dragged along by electrostatic separation.

In a plasma focus, large impulsive magnetic pressures occur due to the large currents involved, typically several hundred kiloamperes. Conductors of current entry and return in close proximity are often subjected to pressures that make it hard to hold the conductors in fixed positions. This may lead to breakage, particularly of the insulator around the CE, which is in the vicinity of high current-carrying conductors. Another example of magnetic pressure in a plasma focus is that due to the current on the surface of the center electrode which produces a compression force on that electrode. Due to the small diameter of the surface current of the pinch itself, ~ 1 mm, magnetic fields in this region may approach a megagauss, equivalent to a pressure of $4 \times 10^4$ atm. Since the focus is in contact at one end with the end of the CE, the CE may be subjected to this pressure for 100 ns

or so. This is like hammering a nail into the end of the CE and, coupled with other impulses such as toothpaste squeezing, ablation and electron beam bombardment, contributes to an indentation in the CE tip.

Magnetic pressure always acts to increase inductance. There are many examples of this. During rundown, magnetic pressure pushes the sheath down the accelerator to increase inductance. (This is also true of the electromagnetic rail-gun.) During pinch, the radial constriction resulting from magnetic pressure dramatically increases inductance. Also, in the rail-gap switch the tendency is for the plasma channels to blow away from the ground plate, due to magnetic pressure. This effect has been used to actuate a magnetic switch which crowbars a capacitor automatically when current (magnetic pressure) exceeds a certain value (Ref. 52).

Power Flow

The phenomena of interest in a plasma focus occur on such short time scales, typically tens of nanoseconds or less, that the propagation of energy through, for example, coaxial cables, depends critically on transmission line and other power flow path lengths. The speed of light is about 30 cm/ns. Transmission line power flow velocities are usually a sizeable fraction of this speed. Some attention must therefore be paid to uniformity of cable lengths and to the flow of power in the vicinity of the switch and to the plasma focus itself; application of power through various cables must be simultaneous within about 10 ns for proper sheath formation. In this case, the use of a single switch creates a fan-in/fan-out problem which may result in current asymmetry at the gun header during breakdown.

An exaggerated example of this type of problem is indicated in Figure 20. All current must flow through the switch, so current arriving and leaving the switch header at either point 1 or point 3 must travel farther to get through the switch than current at point 2. The end current paths are more inductive than the center current paths. Consequently, the rise times of current paths at the ends will be longer. The net effects will be asymmetrical power flow and increased

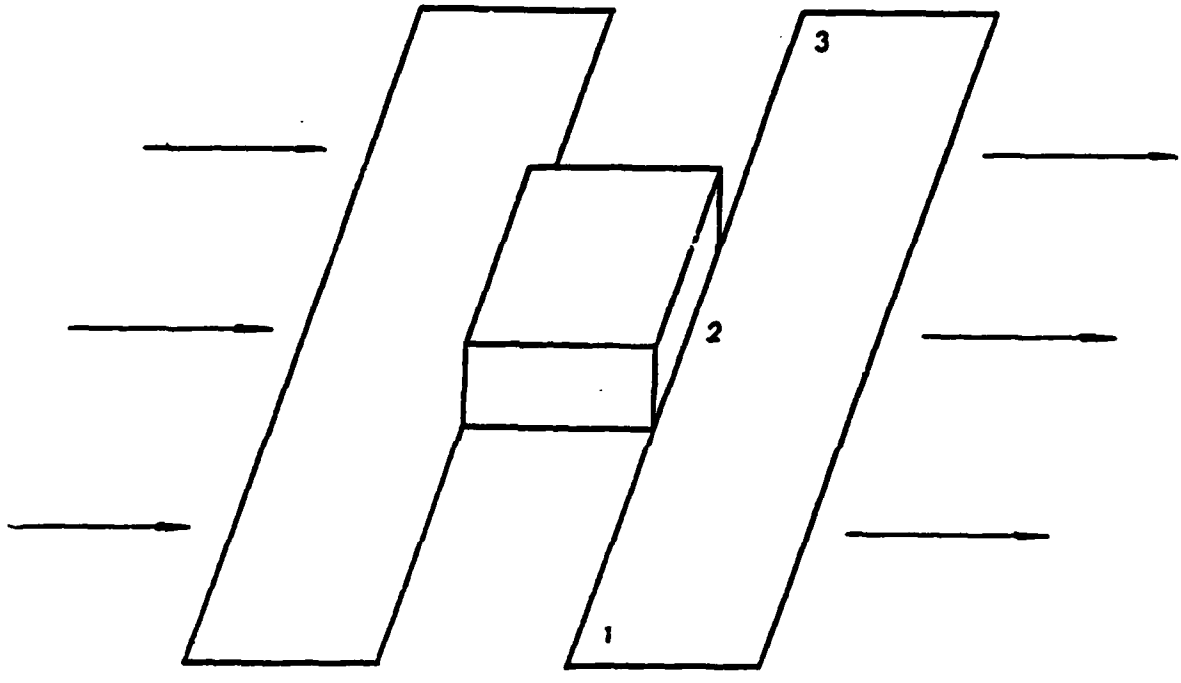


Figure 20. Switch Header Power Flow Problem.

system inductance. If a capacitor bank was on the left and a load on the right, capacitors tied to the center would be preferentially discharged on short time scales. Similarly, that part of the load tied to the center would be preferentially charged on short time scales.

Current leaving the switch header at the right goes to cables arranged in a radial feed to the discharge vessel. This cable arrangement results in azimuthal asymmetry in current feed to thesheath. This may result in poor sheath formation.

Electromagnetic (EM) Noise

A common problem in a plasma focus experiment, or any pulse-power experiment, is to extract and record meaningful electrical data from various probes, despite an environment of high-amplitude, fast-rising electromagnetic pulses. Since physical interpretation depends critically on data quality, solution of this problem is essential.

EM Noise Generation

The EM noise generated by the system may be broken down into three areas--switching noise, contact noise and cable reflections. Consider each of these areas in turn.

Switching Noise

In this case, proper operation of the rail-gap switch requires a high-amplitude, fast-rising trigger pulse. This pulse, the pulse which fires this trigger, the pulse produced by the rail-gap when it turns on, and the pulse produced by the breakdown of gas in the plasma gun all contribute to a harsh electromagnetic background.

Contact Noise

This is noise generated by arcing which occurs between two pieces of metal in poor electrical contact. This is called incipient sparking and may produce high frequency noise. Poor contact may be due to insufficient contact pressure or to dirty contact surfaces, resulting in carbonation of the dirt, further arcing and sometimes erosion of metal surfaces. Also, any contact with aluminum is a problem because the contact is usually initially with the thin aluminum oxide layer which forms on aluminum on exposure to air. This dielectric layer may

hold off several hundred volts and must be penetrated, either mechanically or electrically.

Cable Reflections

Any signal propagated on a cable whose termination differs from the cable impedance will be partially reflected. This contributes to noise in the signal, in the case of a signal cable, and to general EM noise, in the case of a power feed or trigger cable.

EM Noise Suppression

Contact and cable reflection noise may be suppressed by assuring good contacts and proper cable terminations. The EM noise can be avoided by using fiber optics to transmit probe signals through plastic cables almost impervious to external EM fields. Another solution is to make probe signals large, in order to increase the signal to noise ratio. This is feasible for some probes, such as $\dot{I}$ and V probes. However for a $\dot{B}$ probe, increasing voltage sensitivity will degrade frequency response or increase probe susceptibility to noise. Additionally, since signal cables are often close together between the experiment and recording equipment, a cable carrying a low voltage probe signal may pick up part of a high voltage probe signal carried on a nearby cable.

The most common method of noise suppresssion is to electromagnetically shield with conducting metals. This method relies on skin depth. When an EM pulse impinges on a conductor, Faraday's law requires that currents be set up on the surface of the conductor which restrict penetration into the conductor. The depth of penetration is the skin depth, which is frequency and conductivity dependent: $\delta \propto (\sigma\omega)^{-1/2}$. Coaxial cables are a common example of this type of shielding. If they are inadequate because of the EM environment, it is common to place them within a metal conduit or to use triaxial cable to provide another EM shield.

Another common example of EM shielding is the Faraday cage or screen room. A screen room is essential for shielding recording equipment, such as oscilloscopes, from the harsh EM environment of a pulse

power experiment. In this case, the screen room consists of two nearly closed metal shells, one inside the other, for improved EM shielding.

Electromagnetic shielding is also common in magnetic probes, such as $\dot{I}$ or $\dot{B}$ probes. Here shielding often consists of a wrap of metal foil such as copper or aluminum around the probe, with a slot in the foil to permit penetration of the local magnetic field to be measured.

Another noise suppression technique is to eliminate ground loops. A ground loop is a closed conducting path tied to ground at some point. Often, part of the loop is the outer braid of a coaxial cable. Loops are antennas that can pick up EM noise. Loops may be eliminated by paying attention to cable connections or they may be broken by inductive isolation with transformers.

Finally, noise may be suppressed by filtering. A good example is evident in the screen room. The ac power into the screen room is filtered by low-pass filters to minimize EM noise entry into the screen room. Similarly, power lines to supplies or other equipment connected to the experiment may be tied to ground, contributing to ground loops and noise. The use of low-pass filters here is also advisable.

Plasma Purity

Small amounts of impurities can greatly affect plasma focus behavior. Arch enemies of successful, reproducible plasma focus operation are (1) water vapor absorbed on vacuum vessel walls, electrode surfaces and the insulator, (2) electronegative gases admitted through vacuum airleaks, and (3) hydrocarbons such as remain on vacuum vessel or electrode surfaces due to improper cleaning, plasma vaporization of hydrocarbon material in the vacuum chamber such as Plexiglas, or due to improperly trapped diffusion pumps operating with hydrocarbon-based oils.

High-Z impurities can greatly increase radiation losses. Electronegative impurities tend to quench the plasma in its formation stages by absorbing electrons. The macroscopic effects of impurities are as follows. The first few shots of a plasma focus with a new insulator or after the vacuum system has been exposed to atmospheric air usually do

not focus, as evidenced by voltage waveforms (where thed/dt (IL) of sheath rundown produces a characteristic voltage shape). Such failures are thought to be due to water vapor on the insulator surface which prevents sheath lift-off. Such shots are accompanied by pressure rises, indicating the release of surface-bound material into the vacuum vessel. Subsequent shots in which pressure remains steady may often be accompanied by successful focussing. A characteristic of air leakage is that the reproducibility of the focus decreases with time for a single filling, or focus fails after a time to occur at all, as more and more air contaminates the plasma gas. In the case of a highly hydrocarbon-contaminated system, focussing will not occur at all and examination of the vacuum vessel and electrode surfaces will reveal a dirty, carbon-blackened system that often will also smell bad.

Plasma purity is maintained by (1) a good, $\leq 10^{-6}$ torr, tight, cryogenically trapped vacuum system (or one that does not use oil--such as one using a turbomolecular, ion- or cryopump), (2) very careful cleaning of all vacuum vessel and, particularly, electrode surfaces and (3) elimination of hydrocarbon-based materials such as Plexiglas from any part of the system in possible contact with plasma. A cryogenic trap above a diffusion pump or forepump will reduce creep of hydrocarbon oil into the discharge chamber. A low-base pressure insures that the fill gas is not contaminated by impurity gases left in the chamber before the gas fill. A few tenths of a micrometer is a sufficient base pressure provided there are no air leaks to contaminate the fill gas between gas fillings; a very tight system is most important.

## System Component Description

In this paragraph the major system components are discussed: 17/14 cables,energy storage capacitors, the rail-gap switch and its header, the gun header, gun header current and voltage monitors, the discharge vessel, the Micro-Marx trigger generator, the screen room, the charge/dump box and the vacuum and gas flow system. A good idea of the relationships between most of these components is given in the electrical schematic of Figure 21. Figure 22 is a photograph of the complete system.

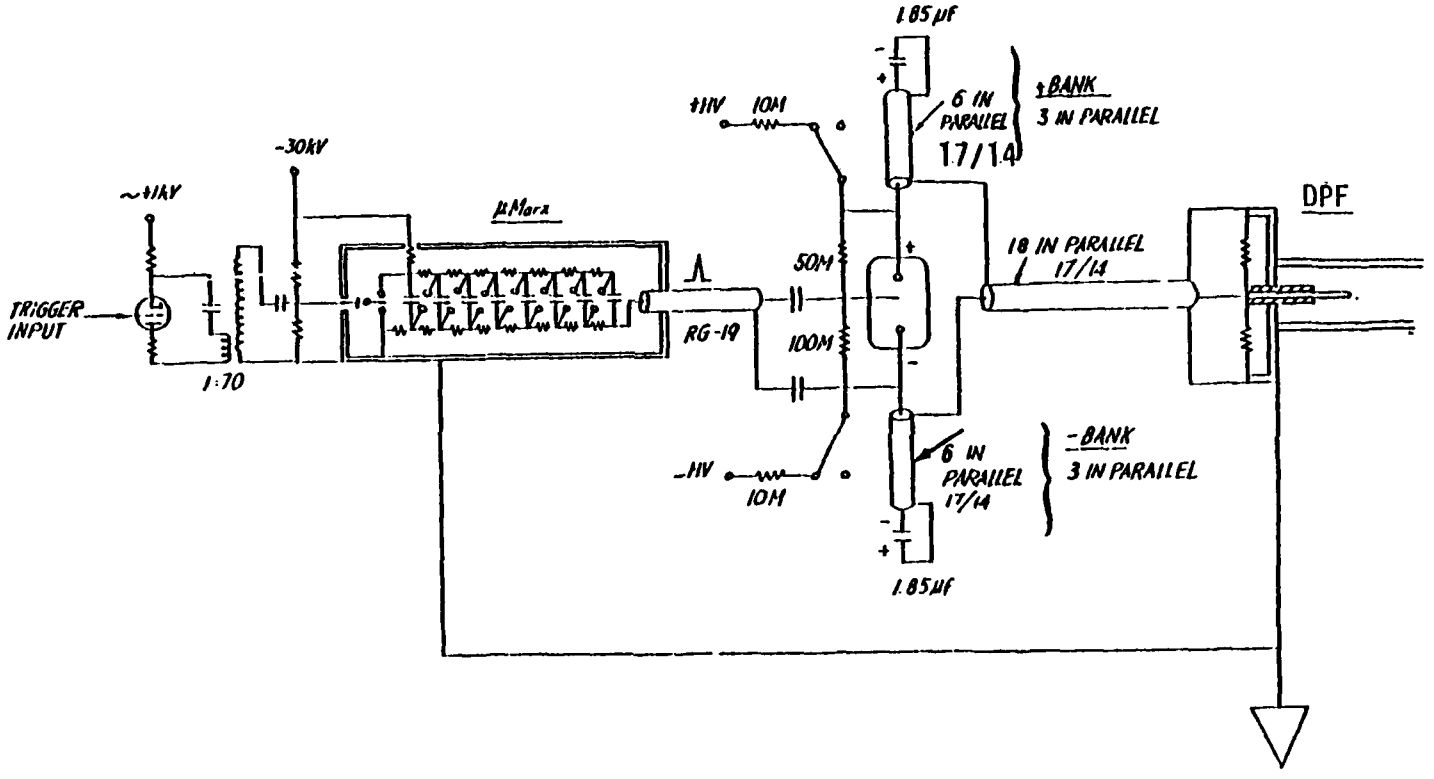


Figure 21. HVDPF Electrical Schematic.

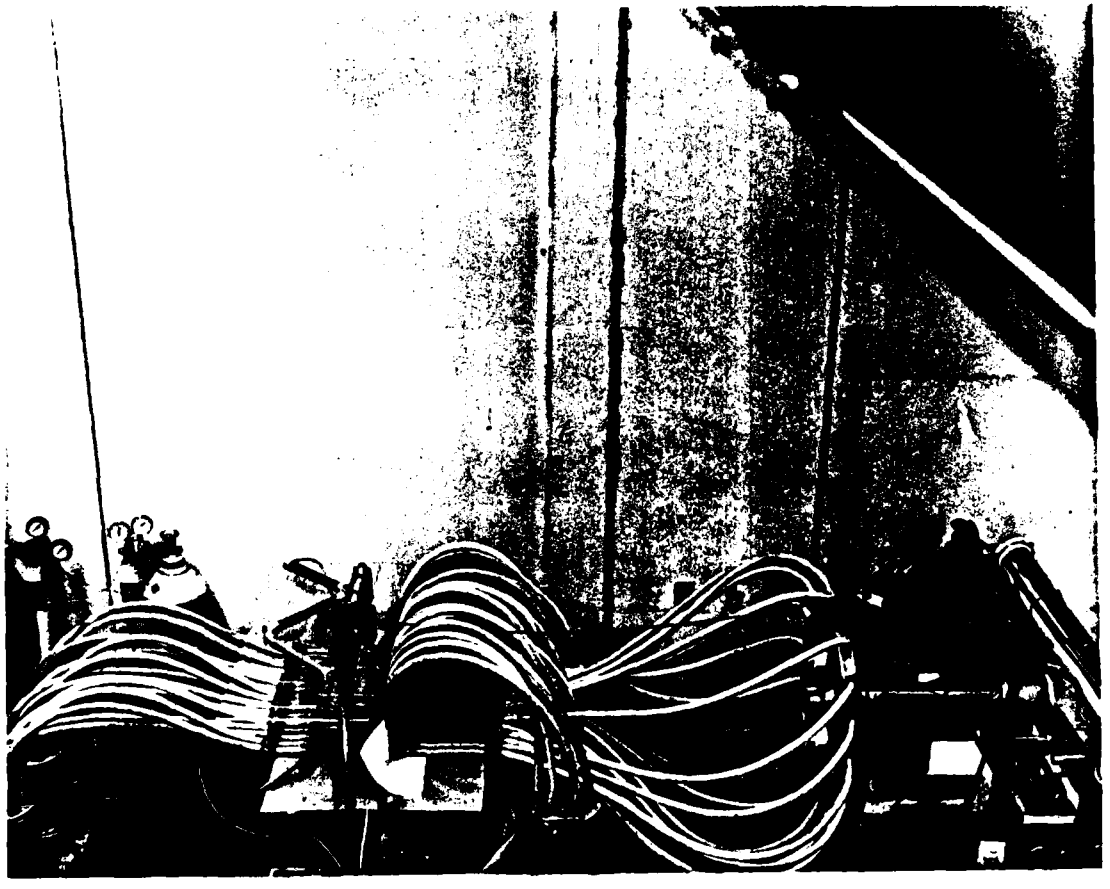

Figure 22. Photograph of Complete HVDPF System.

## 17/14 Cables

Cables were chosen for power flow between the capacitors and the switch and from the switch to the gun header because cables permit more flexibility than strip lines, though strip lines are typically less inductive. Paralleling of cables, however, can reduce inductance to acceptable values. Cables were also chosen because they were available from the Los Alamos National Laboratories (LANL) and they provided easy connections to Scyllac capacitors, following, roughly, the arrangement used in the Scyllac experiment. The cable used is the 17/14 cable used in LANL theta-pinch experiments. This cable is a hybrid between RG17 and RG14 cables and is designed for low inductance, ~ 40 nH/ft, and high voltage. Scyllac 17/14 cables have been pulse tested at 120 kV and are, therefore, suitable for power flow from both of our capacitor banks and from the switch to the gun header.

In using cables there is a problem of connecting cable inner braids to other system components. The outer braid connection is simple because small diameter hose clamps clamping the outer braid to copper couplings provide good, simple electrical contact. For inner braid connections, it was decided to soft-solder a 3/8-in-dia brass rod to the inner braid. This permitted setscrew contact of the brass rod within connection holes. In oil-immersed situations, no attention was paid to bare braid wires at the soldered braid/rod junction. However, in open air situations, these sharp points are open invitations to corona and breakdown. For that application, 1/16-in wall shrink tubing was used to cover as much exposed metal at the junction as possible.

## Energy Storage Capacitors

The Scyllac capacitors have intrinsic inductance which cannot be changed without redesign. However, the net inductance may be reduced by placing capacitors in parallel. Of course, this requires an inductive connection for each added capacitor so the total inductive situation must be carefully evaluated.

Connections to capacitors were made as simply as possible while minimizing inductance and breakdown problems and making good electrical

contact. Figure 23 shows both the construction of these capacitors and a cross section of the cable connections to the capacitors, with rough inductance calculations included.

To prevent breakdown and to simplify cable connections, it was decided to use the Scyllac switch housing cans already installed on the capacitors. Initially these cans admitted six 17/14 power cables to each capacitor and contained oil-immersed, pressurized dry air switches. The switches were removed but the cable outer braid connections (hose clamp on copper coupling) on the top of the can and oil immersion of the cable inner braid connections to the capacitor center electrode were retained. This required machining and installing a mushroom-shaped piece of aluminum with a center hole permitting a bolt directly to the capacitor inner connector. The rounded top edge of the mushroom (Fig. 23b) is for electric flux control. The mushroom has six holes for brass cable plugs, with setscrews for good contact between the plugs and the mushroom. Also for good contact, a ~ 20-mil ledge was machined on the bottom of the mushroom in contact with the capacitor inner connector. Transformer oil covered the mushroom and cable plugs to a level several inches above the top of the mushroom.

This method of connecting to the capacitors is somewhat inductive. The geometry is roughly cylindrical: the can is the return current conductor and the six inner braids of the cables are the inner conductor. From Equation 29, it can be seen that inductance is minimized if the radius of the six cables is close to the can radius. This was attempted, within mechanical constraints. The inductance estimates in Figure 23b indicate inductance in the cable region of the capacitor connection. The contribution to total system inductance by the capacitors and their cable connections is indicated in Table 1.

Rail-gap Switch and Switch Header

The purpose of the switch is to place the positive and negative capacitor banks in series across the plasma focus load. The switch must be able to hold off 120 kV indefinitely, and it must turn on in ~ 10 ns, be able to pass ~ 500 kA and have low inductance. The

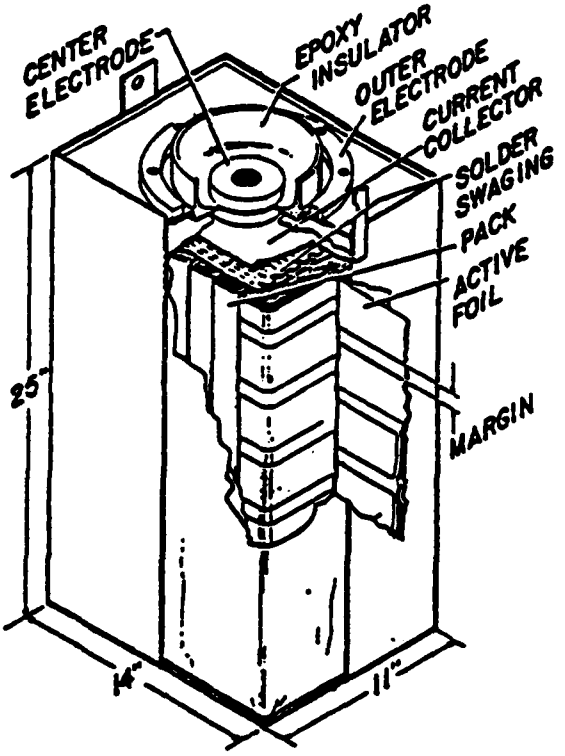


a. Capacitor Construction

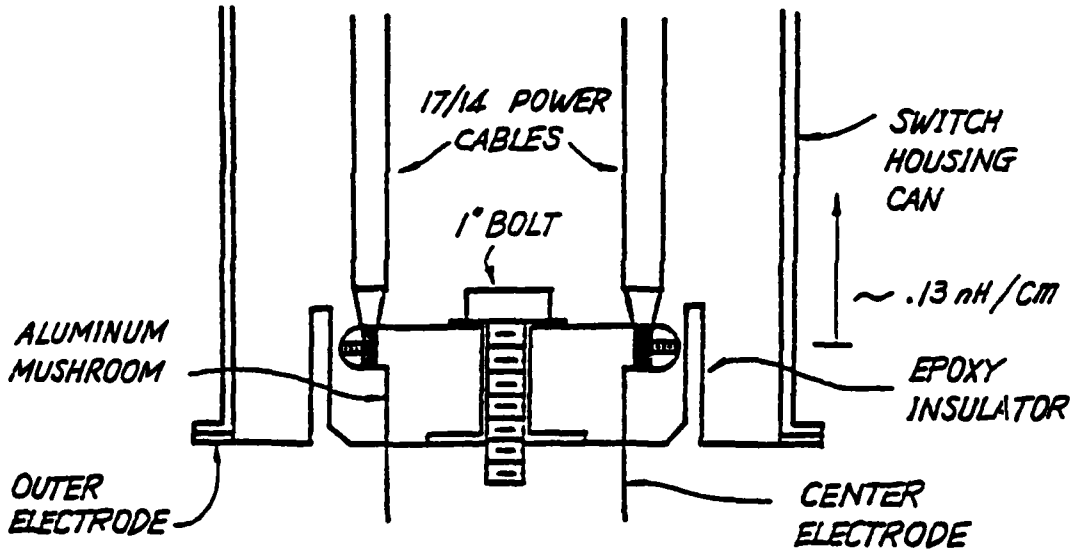


b. Capacitor Power Connection

Figure 23. Scyllac Capacitor Construction and Capacitor Power Connection.

TABLE I. INDUCTANCE ESTIMATES FOR MAJOR SYSTEM COMPONENTS

| Components | nH |
|---|---|
| 37 nH per energy storage capacitor up to top of capacitor | 25 |
| 17/14 cable--40 nH/ft | |
| 3 1/2 ft per cable from capacitor to rail-gap switch, 36 cables | 16 |
| 4 2/3 ft per cable from rail-gap switch to gun header, 18 cables | 10 |
| Rail-gap switch with good multichanneling | 38 |
| Gun header | 11 |
| External inductance $L_e$ | 100 |

Maxwell 40100 rail-gap switch was found to meet or exceed these requirements and so was chosen for this experiment. Figure 24 shows the basic parts of this switch.

The basic idea of the rail-gap switch is that it takes a finite time for a high-current-carrying plasma channel to form in a spark gap. If the gap is in the form of two parallel rails, with a knife-edge trigger blade between the rails, a trigger pulse of sufficient amplitude and rise time will initiate many streamers along the length of the rails. Many of these streamers will develop into high-current-carrying plasma channels more or less simultaneously. (If the pulse rise time is too slow, one channel will close and take all the current before another channel can grow to maturity.) Thus, the rail-gap switch consists of many spark gaps in parallel. The inductance of the total switch is L/n, where L is the single channel inductance and n is the number of channels. If there is good multichanneling, the channels approximate a sheet of conducting plasma and the planar geometry of Figure 18b is appropriate. In addition to reducing inductance, each channel in a multichanneled switch carries 1/n of the total switch current, thus reducing electrode wear.

The switch assembly, including switch and switch header, must accommodate 18 cables from each capacitor bank and 18 cables to the gun header. The switch assembly must permit no breakdown while the capacitors are charged or charging. Also, inductance of the switch assembly must be minimized.

Maxwell recommends that in applications above 50 kV, polycarbonate flashguards be epoxied to the switch to prevent flashover between the two main switch electrodes, either around a side of the switch or under it. These flashguards are pieces of 1/8-in Lexan, a vertical (perpendicular) piece or a horizontal (parallel) piece. The two basic flashguard arrangements are shown in Figure 25. A hybrid of these arrangements was chosen (Fig. 26 and 27). A thickness of 1/8-in Lexan is sufficient to hold off 120 kV but thin enough to keep switch inductance, determined by the distance of the switch above the return

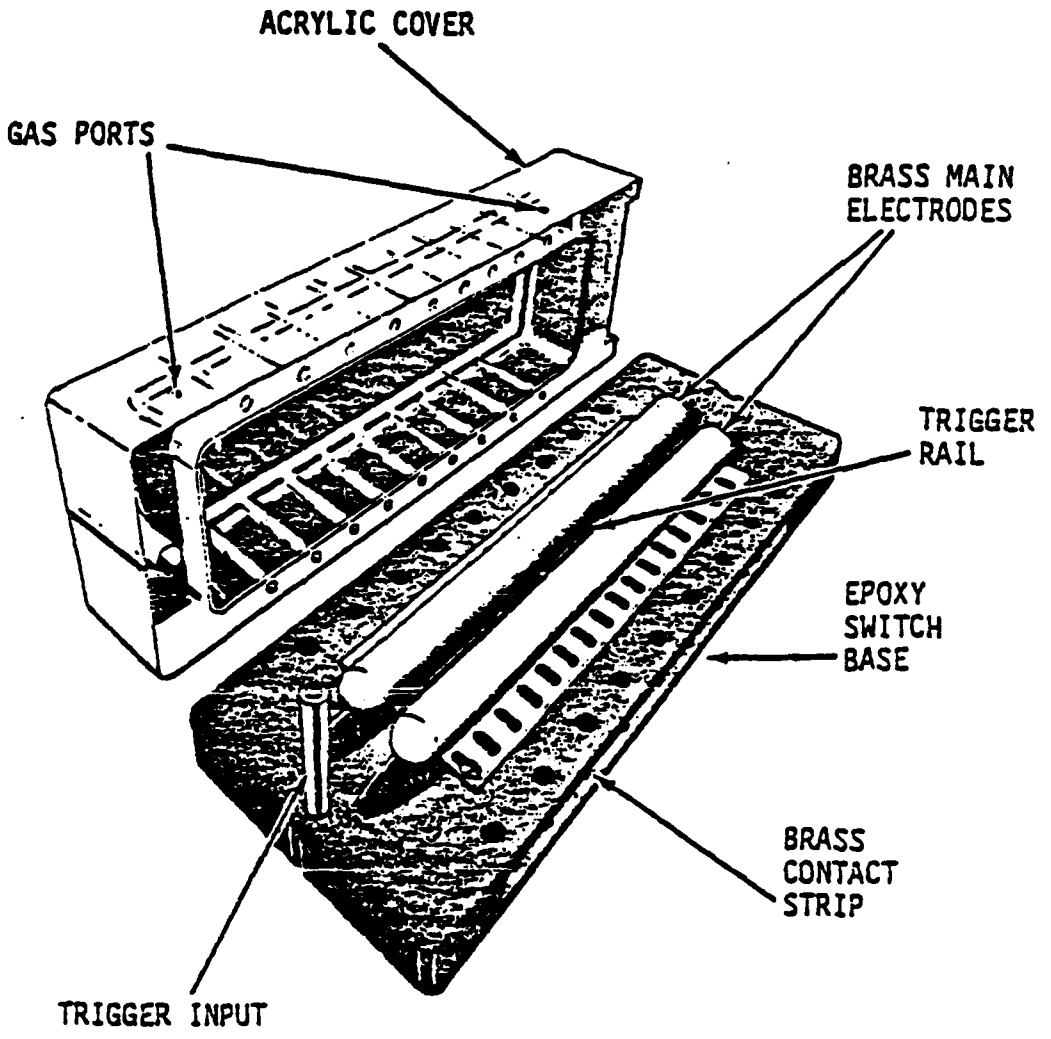


Figure 24. Rail-Gap Switch Construction. (Courtesy of Maxwell Laboratory).

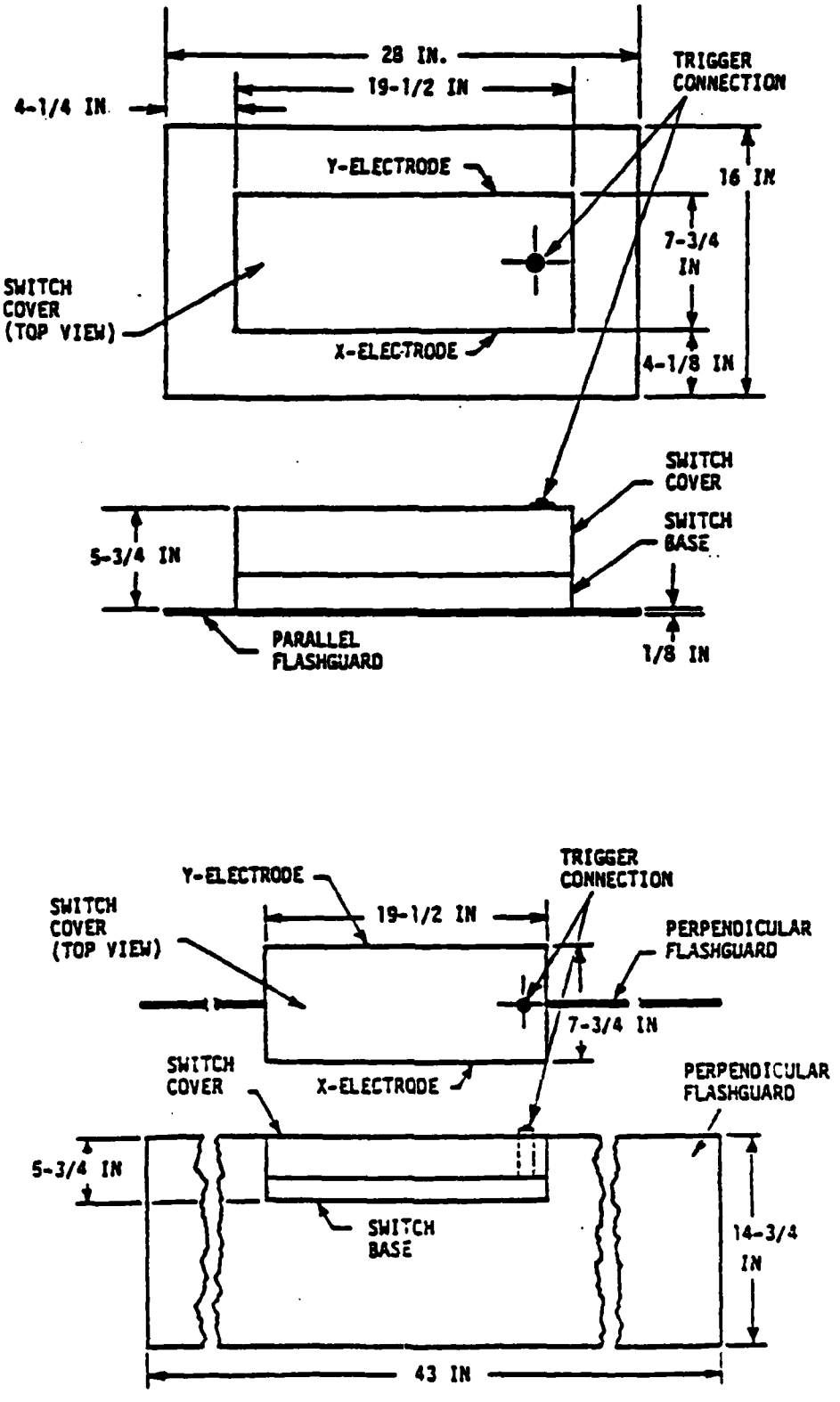


Figure 25. Rail-Gap Flashguard Arrangements. (Courtesy of Maxwell Laboratory).

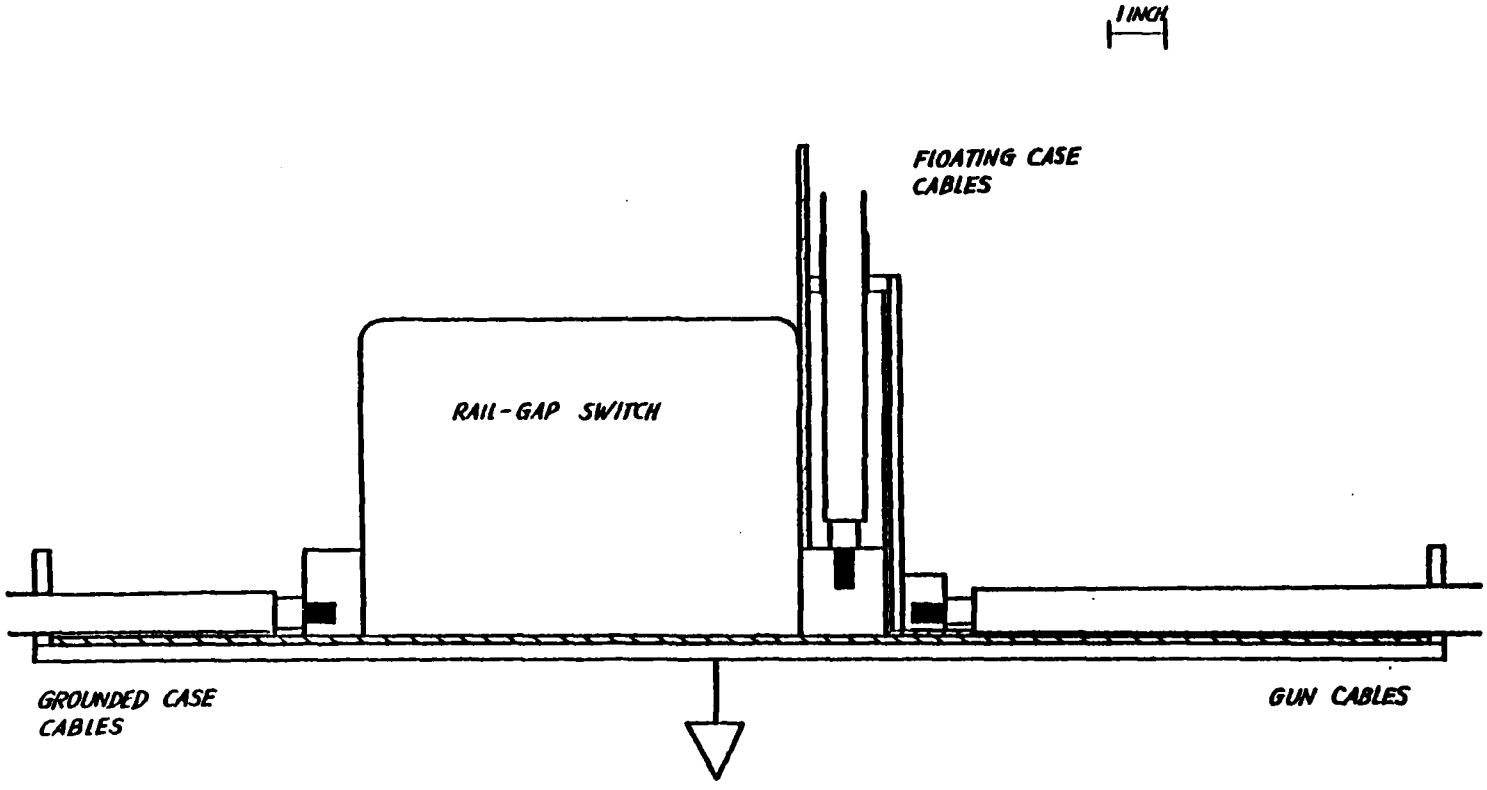


Figure 26. Switch Header Design.

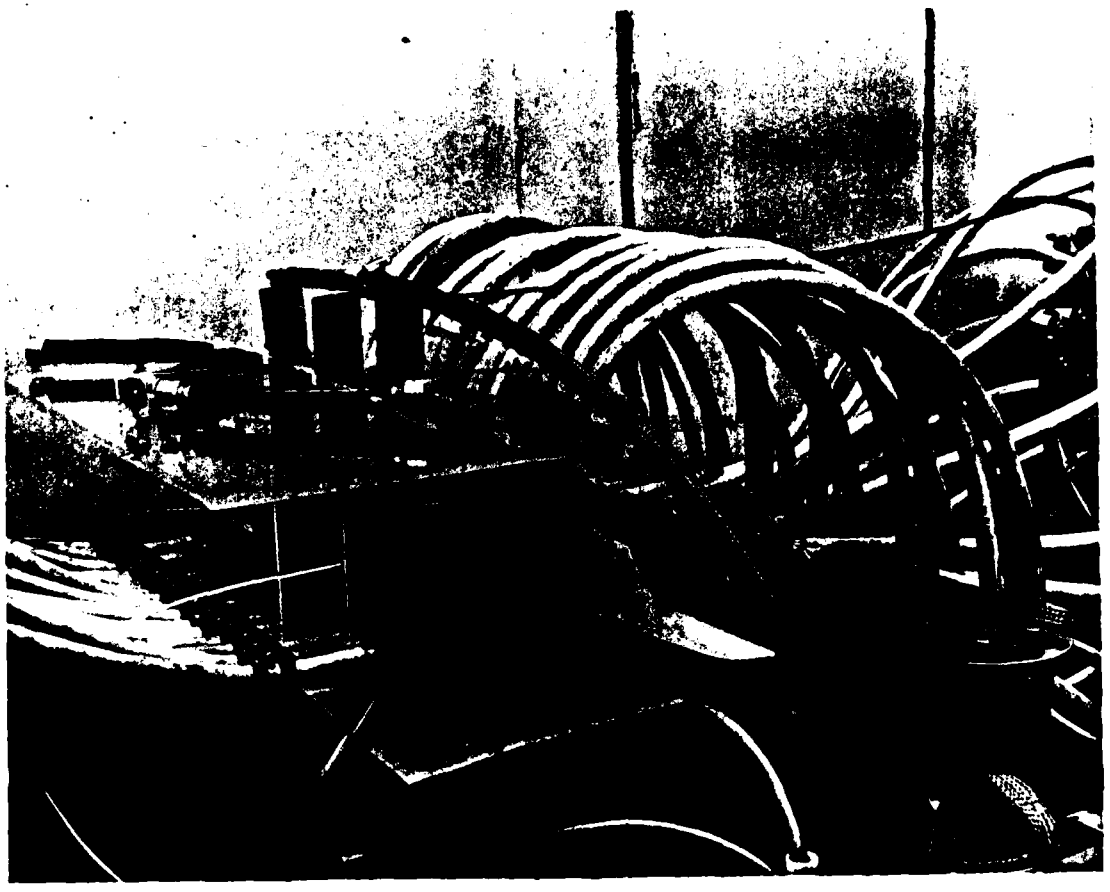

Figure 27. Photograph of Complete Switch Assembly.

current brass plate, to a minimum (Fig. 18b). The vertical part of the flashguard fits into a groove machined into the switch and its cover. With the vertical flashguard in place, silicone vacuum grease is injected into the groove in the switch cover to further prevent flashover.

It was decided to use brass bars for the transition between the switch and the cable plugs for each of the banks and for the gun header cable plug connection. Two bars were bolted directly to the switch electrode strips with small rectangular ledges machined into the bar faces for improved electrical contact. Needless to say, the bolts to the switch are well torqued, also for good electrical contact.

It was decided that 10 cm was sufficient to hold off 60 kV between a capacitor bank plug bar and the associated coupling bar. The plug bar for the gun cables is at ground until the Marx erects, at which time it rises to the potential of the erected bank. This pulsed situation is less stringent than a dc hold-off situation. In this region, 25 cm was allowed for hold-off. The basic layout of the switch assembly is shown in Figure 26. As mentioned earlier, the use of a single switch introduces a fan problem evident in Figure 27.

As usual, to reduce corona and breakdown all relevant edges were radiused. This included all edges on the brass bars and exposed edges on the three copper coupling bars.

To further assure good contact and good mechanical strength, all copper couplings were hard-soldered to the coupling bars. Coupling bars were then bolted and soft-soldered to the brass ground plate. The assembly for the gun header plug bar was also bolted and soft-soldered.

The biasing/trigger assembly for the switch presented the usual problems of inductance minimization and corona/flashover prevention. The electrical schematic of the biasing/trigger assembly is shown in Figure 28. Inductance minimization is important here because pulse rise time, required for proper switch multichanneling, goes as L/Z, where Z is the impedance of the circuit driving the discharge. A strip line was used for the outer braid connection from the trigger cable to the switch. Also, sheets of acrylic permitted close proximity of

AD-A164 298 OPERATIONAL CHARACTERISTICS OF A HIGH VOLTAGE DENSE PLASMA FOCUS(U) NEW MEXICO UNIV ALBUQUERQUE DEPT OF CHEMICAL AND NUCLEAR ENGI D M WOODALL NOV 85 2/2

UNCLASSIFIED AFWL-TR-84-119 F29611-82-K-0075 F/G 20/9 NL

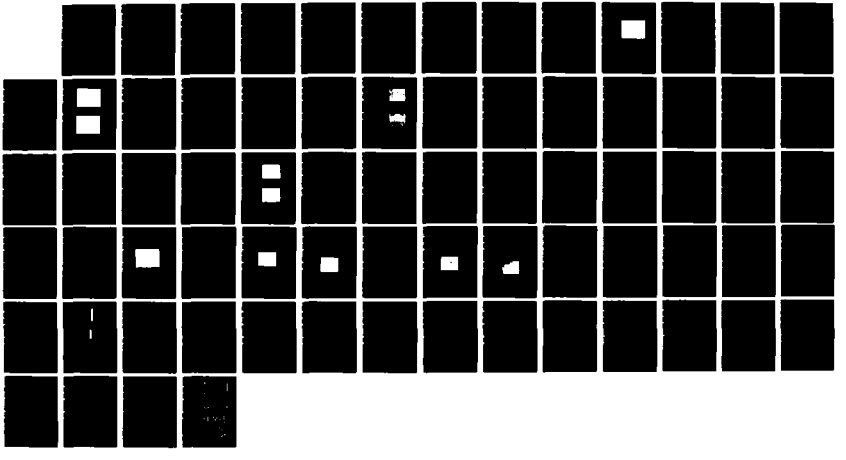

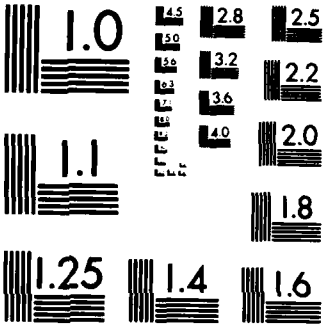


MICROCOPY RESOLUTION TEST CHART

NARDS 1963-A

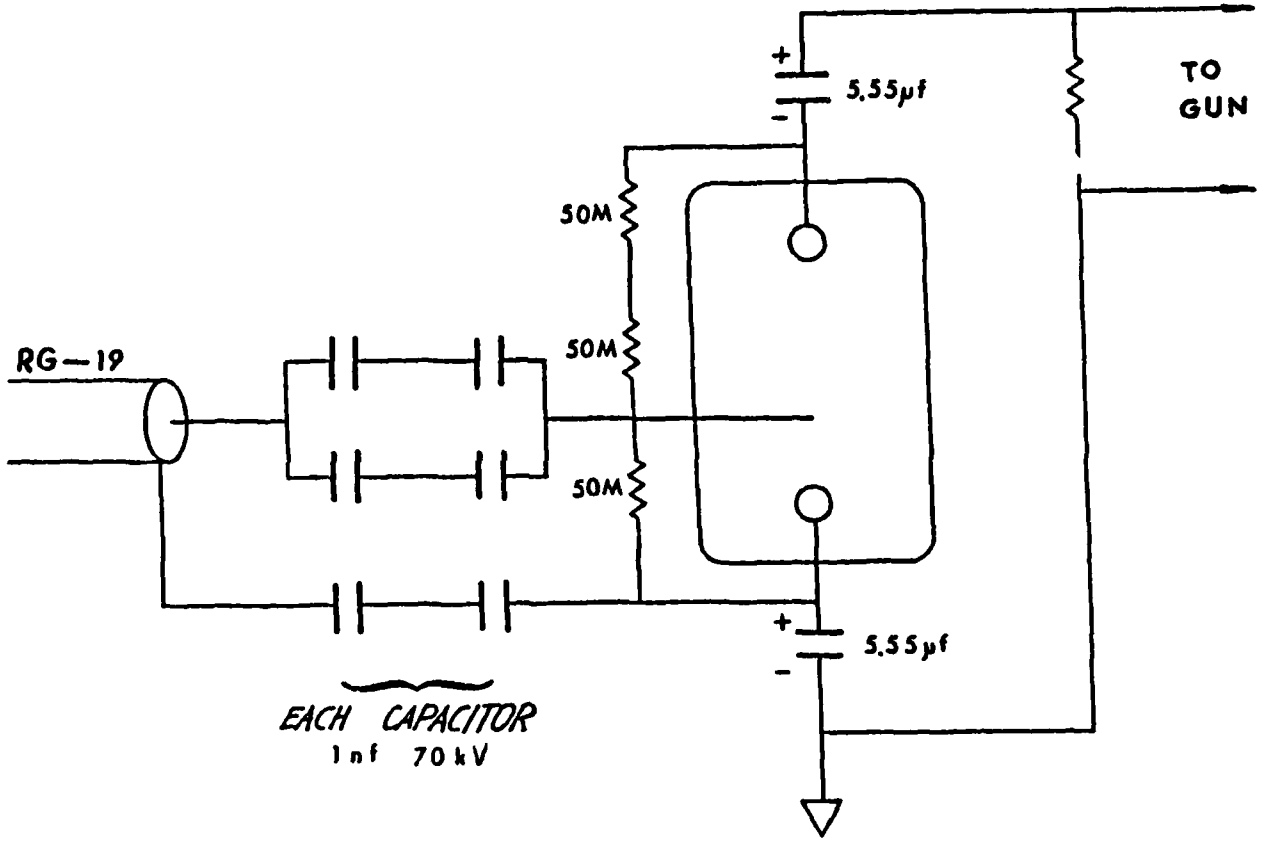


Figure 28. Switch Biasing/Trigger Circuitry.

components of this assembly, thus minimizing inductance. Finally, the RG19 cable carrying the trigger from the Micro-Marx to the rail-gap trigger blade was terminated in the cable impedance, 50 Ω, to eliminate cable reflections. The termination consisted of 12 2-W carbon composition resistors in series, placed inside a 1/16-in Tygon tube to prevent breakdown. This assembly was placed close to the cable insulation around the solid inner conductor to reduce the inductance of the termination in order to keep it as nearly purely resistive as possible.

Gun Header and Discharge Vessel

The gun header is shown, with part of the discharge vessel attached, in Figure 29. The gun header required the most thought in design. It had to hold off pulsed 120 kV between the ground plate and the anode plate and between the ground plate and any of the metal in electrical contact with the anode plate. The gun header also had to withstand the large magnetic pressures produced in routine operation. Further, in the event of asymmetrical power flow, due, for instance, to spoke formation, the assembly had to withstand even larger, asymmetric magnetic pressures. If the arrangement were such that magnetic pressure could alter the parallel relationship between the anode and ground plates, the glass insulator would probably crack. This is an undesirable result, in itself, but it also would lead to current paths that would produce magneforming of header pieces requiring remachining. This actually occurred on one shot when insufficient attention to assembly resulted in mechanical stress on the insulator, aggravated by asymmetrical magnetic pressure.

Also, the connection between the discharge vessel and the ground plate had to provide good electrical contact and accommodate the vacuum/air interface between the Pyrex insulator and the back plate of the discharge vessel. In addition to these constraints, inductance minimization was also required.

To satisfy the requirement of rigid parallel geometry between anode and ground plates, four 3/4-in-dia nylon bolts were used to sandwich these two plates together (with a 1/8-in thick sheet of insulating

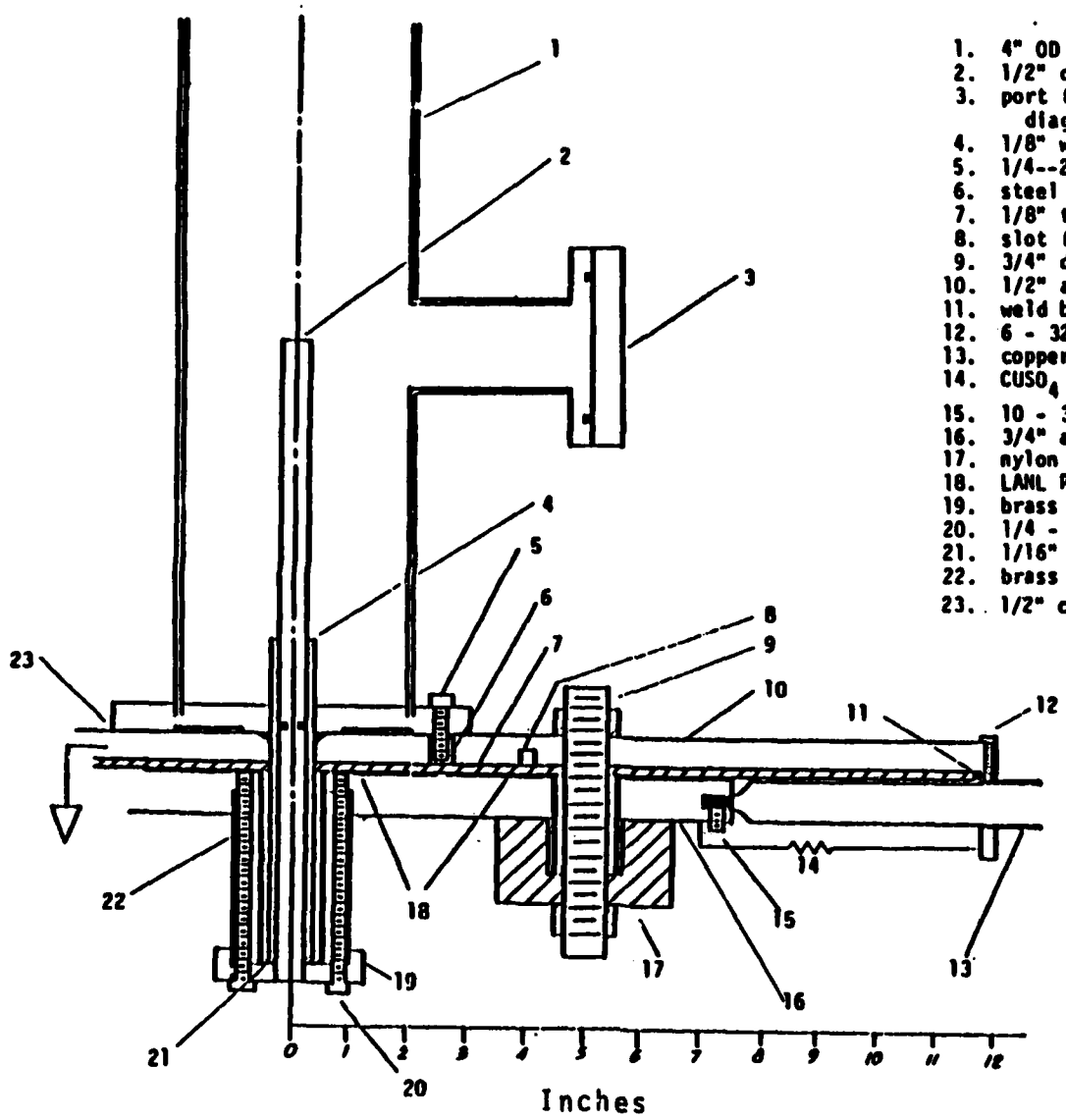


1. 4" OD .095" wall, type M copper tube
2. 1/2" dia. copper rod
3. port for X-ray, image converter diagnostics, spectroscopy
4. 1/8" wall Pyrex insulator
5. 1/4--20(8)
6. steel Keensert
7. 1/8" thick poly sheet
8. slot for Rogowski coil
9. 3/4" dia. nylon bolt (4)
10. 1/2" aluminum ground plate
11. weld bead
12. 6 - 32 (18)
13. copper coupling (18)
14. $CUSO_4$ termination resistor (18)
15. 10 - 32 (18)
16. 3/4" aluminum anode plate
17. nylon bolt spacer
18. LANL poly hats--499 Det. 17
19. brass anode cap
20. 1/4 - 20 (8)
21. 1/16" poly washer
22. brass anode connecting ring
23. 1/2" copper plate

Figure 29. Gun Header Design.

polyethylene between). This resulted in holes in both anode and ground plates and possible breakdown through the holes in the polyethylene sheet. For this reason, polyethylene hats were used to hide the hole edges in the anode plate from those in the ground plate. As a further precaution, the hole edges were radiused. Nylon bolt spacers were also used on the anode plate to increase breakdown path lengths through the bolt holes.

The center hole presented special problems because the anode cap has a direct path to the center hole in the ground plate. Two remedies were initially tried: to move the anode cap back from the anode plate (thus increasing inductance) and to use a central polyhat. After several hundred shots in the 80 kV range, this method failed, resulting in an air discharge around the outside of the Pyrex insulator, from the anode cap to the ground plate center hole edge. At this point the anode cap was moved still further back from the ground plate, the top of the central polyhat was extended, a polywrap was inserted within the central polyhat, and a 1/16-in polywasher was placed on the inside of the anode cap. To date, this method has proved effective against further failure.

The present arrangement for the vacuum/air interface between the Pyrex insulator and the backplate of the discharge vessel was chosen after difficulty was experienced with an O-ring seal within the backplate of the discharge vessel.

Good electrical contact between the ground plate and the backplate of the discharge vessel was accomplished with two concentric ledges. The large radius ledge was cut some 20 mils under the inner radius ledge to assure good contact between the ground plate and the inner radius ledge.

The usual copper coupling connection to the cable outer braids was used but with brass couplings. It was deemed difficult, expensive, and/or impossible to weld or solder brass to aluminum in order to provide the necessary good electrical contact. For these reasons a thermal expansion method was used.

Additionally, the contact between the ground ring and the ground plate was improved by a weld bead on the inside of the ring (where current flows). The inside edge of the ground ring was also radiused.

A final detail was to reduce electromagnetic noise by matching cable terminations at the gun header. Here the object is to reduce cable reflections without dissipating much energy in the termination resistors. It was decided that a resistance of two or three times the cable impedance was appropriate. Also, the resistors used must not be damaged by the energy dissipated in them and they should have a geometry that does not produce high electric fields and encourage breakdown. We chose aqueous solution copper sulphate resistors with ~ 50 Ω resistance, about twice that of the 17/14 impedance. The copper sulphate solution was sealed with plastic tie-wraps into Tygon tubing with well-radiused copper end plugs providing electrical contact with the solution.

Gun Header Current Monitor

Total $\dot{I}$ in the discharge vessel is measured by an electrostatically shielded Rogowski coil placed in a groove on the side of the ground plate facing the anode plate. This placement is indicated in Figure 29. The Rogowski coil measures $\dot{I}$ directly, which is integrated to give I by an RC circuit with a time constant of 20 μs. The sensitivity of the Rogowski coil may be calculated from its radial cross-sectional area, its mean radius and the number of loops in the coil. The calculated sensitivity is $6.6 \times 10^{-10}$ V/(A•s). Insulation on the coil wire makes the loop area somewhat uncertain, as does variation in B field magnitude across the loop. The coil was therefore calibrated in short-circuit tests and found to be $5.4 \times 10^{-10}$ V/(A•s). The integrated current signal was also calibrated at this time. During the short-circuit tests, the high frequency response of the Rogowski coil was found to be very good. The $\dot{I}$ rose from zero to $\dot{I}_0$ in under 20 ns. This is possibly a limit of switch turn-on rather than the Rogowski response, as was suggested by tests with a DPF load in which extremely fast $\dot{I}$ rise times (< 10 ns) were observed.

Gun Header Voltage Monitor

Voltage measurement at the gun header was accomplished with a resistive voltage divider consisting of a string of 12 430-Ω, 2-W TRW resistors placed inside Tygon tubing to prevent breakdown. The high frequency response of this string is good due to the small time constant of the RC circuit comprised of the string and stray capacitance to ground. Also, inductance is minimized by keeping the (relatively) large inductance paths between resistors small and by placing the string as close to the header as possible. Application of a fast-rising (~ 10 to 20 ns to peak amplitude) battery box pulse at the resistor string showed no noticeable loss of rise time, through cables and attenuators, at the scope. Calibration was accomplished by dc measurement of the attenuation of an applied battery voltage.

Micro-Marx Trigger Generator

The Micro-Marx provides the trigger pulse for the rail-gap switch. The Micro-Marx was designed at LANL. Tho LANL provided schematics, some components, and much useful advice about building and using this device. An electrical schematic is shown in Figure 30.

The Micro-Marx consists of an 8-stage Marx generator. Each stage consists of a 2400-pf barium titanate capacitor, spark gap and charging resistors. With each stage charged to 30 kV, the erected voltage is 240 kV with $9_J$ total energy. The device is described in detail in Reference 103. It erects quickly, ~ 20 ns, because the spark gaps are in line and can see each other. When one gap breaks down, it illuminates the other gaps with ionizing radiation which ensures rapid breakdown of the other gaps. The UV irradiation of gaps in this manner is a common method of making gaps turn on quickly.

One disadvantage of this particular design is that the impedance of the generator is twice that of the RG19 output cable. This halves the erected pulse amplitude, however, if the output cable is unterminated, cable reflection there will double the pulse to its original amplitude. Note that if the noise generated by these cable reflections is undesirable (as it proved to be) then the cable must be properly

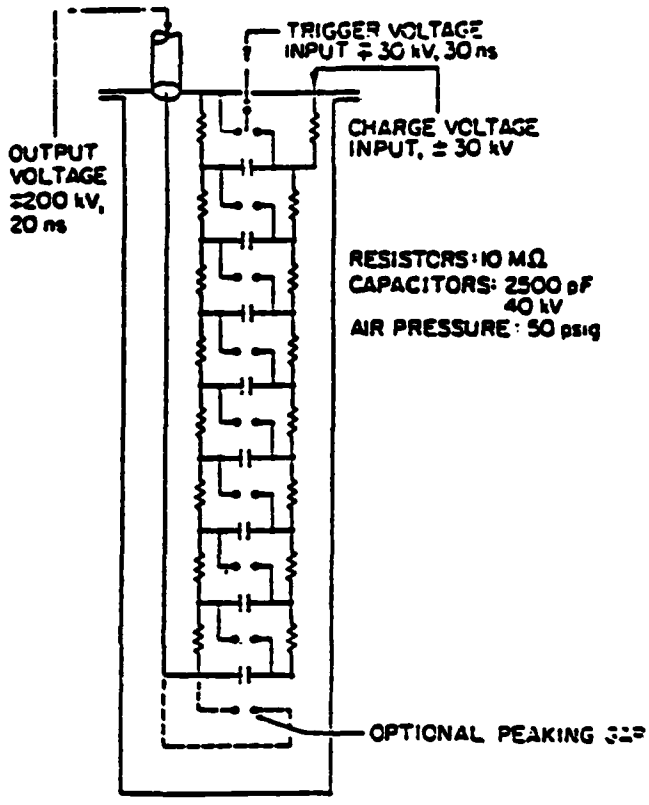


Figure 30. Micro-Marx Electrical Schematic. (From Ref.53).

terminated. This leads to a pulse amplitude and rise time which are less than those cited in Reference 53, which assumes an unterminated cable. The reduced pulse amplitude and rise time result in poorer rail-gap multichanneling. A typical terminated Micro-Marx output waveform is shown in Figure 31. The pulse amplitude is ~ 120 kV with ~ 6 kV/ns rise.

The high internal impedance (~ 100 Ω) of this design is due to rather large internal inductance (~ 1 μH). The device is inductive because of the fairly large radius, roughly helical path the current takes through the capacitors and gaps. Veradyne sells a $3000-$4000 version of the Micro-Marx with much lower internal inductance and, consequently, higher rise time and pulse amplitude into the output cable. The pulse rise time can also be improved by using a peaking gap on the output of the Micro-Marx.

Screen Room

The screen room is an essential system component. It is a difficult structure to build correctly because of possible EM noise leakage at the various seams, particularly at the door, and feedthroughs for power, signal and trigger cables.

Ideally, one can purchase a high quality commercial screen room. An adequate screen room would have cost $10,000 or more, so it was decided to build one instead, using galvanized sheet for the lower half and galvanized screen for the upper half to permit convective cooling of oscilloscopes.

The screen room was insulated from the concrete floor of the lab with a sheet of polyethylene on top of a sheet of plywood. This was done because concrete is somewhat conductive and contact with it would create a ground loop.

Essential in screen room construction is that the inner shield contact the outer shield at only one point. Two-point contact creates a loop on which currents can circulate, possibly injecting EM noise inside the screen room. Also required is a single, high-quality ground contact to the screen room. This was finally accomplished by drilling

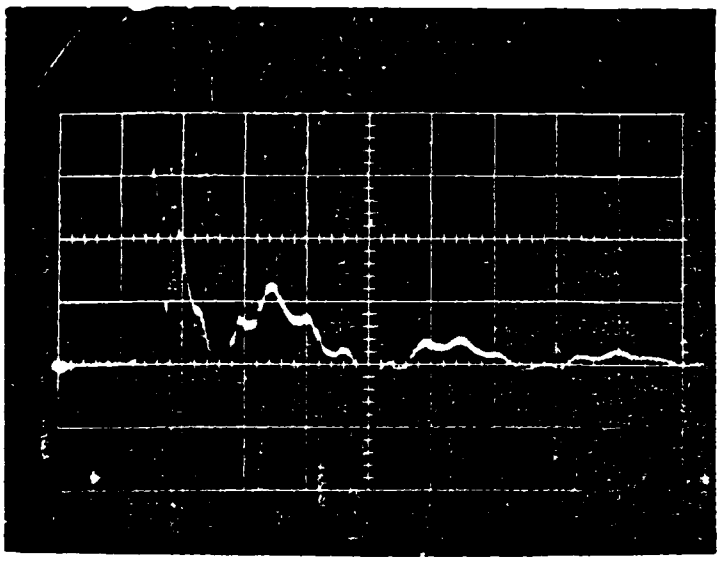


Figure 31. Typical Micro-Marx Output Pulse.
Charge Voltage is ∿25 kV.

a hole through the concrete laboratory floor to permit good, direct contact with the earth.

The building of an electromagnetically tight, double-shielded door is by no means trivial. Buying a screen room is almost worth the difficulty of building a good door. Contact between the door and each shell is accomplished with phosphor-bronze fingerstock.

Charge/Dump Box

Charging and dumping capacitor banks require switching between these two functions and resistors to limit current, in the case of charging, and to absorb energy stored in the capacitor banks, in the case of dumping. Antenna relays were chosen for switching. The maximum current of the power supplies is 5 ma. With a maximum voltage of 60 kV, this determines the value of the current-limiting resistor and gives a rough estimate of the maximum power it must dissipate. High voltage carbon film resistors were used for charging.

The requirement for the dump resistor is that it not be damaged when 10 kJ is dumped into it. Copper sulphate resistors were used because water has a high specific heat and copper sulphate resistors are easy to construct. These were designed so that their temperature rise would not exceed 30°C above room ambient after absorbing 10 kJ. This prevents boiling in the resistor liquid.

Finally, it is desirable to monitor the voltage on each capacitor bank to determine when they are fully charged, dumped or still at some lethal voltage. Negligible current should be drawn from the charging current by the monitor but enough current must be diverted to deflect a current meter. A kilovoltmeter was designed using a 100 $\mu$A full-scale ammeter in series with a 1 G$\Omega$ resistor.

Because charging, dumping and monitoring take place at high voltages, and the components required often have sharp edges, the entire assembly was submersed in oil in a Plexiglas charge/dump box. This also relaxed the power dissipation requirements of the charge resistors. Wires were brought out of the box for monitors, relay control, power supply feeds, capacitor bank feeds and ground.

Vacuum and Gas Flow System

This system component must maintain plasma purity by providing a good vacuum base pressure before the prefill gas is admitted to the discharge vessel. It must also provide the means of admitting small, precisely controlled quantities of gas to the discharge vessel.

The vacuum system is shown schematically in Figure 32. It is basically a standard Veeco vacuum station. It includes a 4-in-dia diffusion pump, with liquid nitrogen trap, producing pressures of ~1 x $10^{7}$ torr when the system is clean, all seals are in good condition and system out-gassing is complete. More realistically, base pressures in the 3-10 x $10^{-6}$ torr range are typical of operation.

A pressure of $10^{-5}$ torr is 5 to 6 orders of magnitude below typical fill gas pressures and so would seem to guarantee plasma purity to one part in $10^{5}$ or $10^{6}$. This is well beyond the purity of typical gas supply cylinders. In fact, ultrahigh purity gas cylinders are generally only pure to one part in $10^{4}$, at best. The effectiveness of this base pressure is deceptive, however, for two reasons. First, as soon as the valve shutting off the discharge vessel from the pumping system is closed, the pressure will rise to 1-2 x $10^{-4}$ torr due to system outgassing and leaks. Secondly, the leak rate of air into the system depends on the pressure within the discharge vessel and will drastically decrease as soon as a few torr of gas is admitted to it. Gas contamination thus depends partly on how quickly the discharge vessel valve is closed and how soon after and at what pressure the fill gas is admitted.

The gas flow system requires valves that are leak-tight when shut and when open will admit small (to pressures of ~ 10 μm - 10 torr), controllable amounts of gas. Also, the system must be able to accurately monitor these pressures as the gas is admitted.

For calibration purposes, a McLeod gauge is attached to the system. It is the ultimate pressure gauge in the region of $\leq$ 1 to 500 μm. However, because of its mode of operation, it is not possible to use this gauge to measure gas pressure changes as the discharge vessel

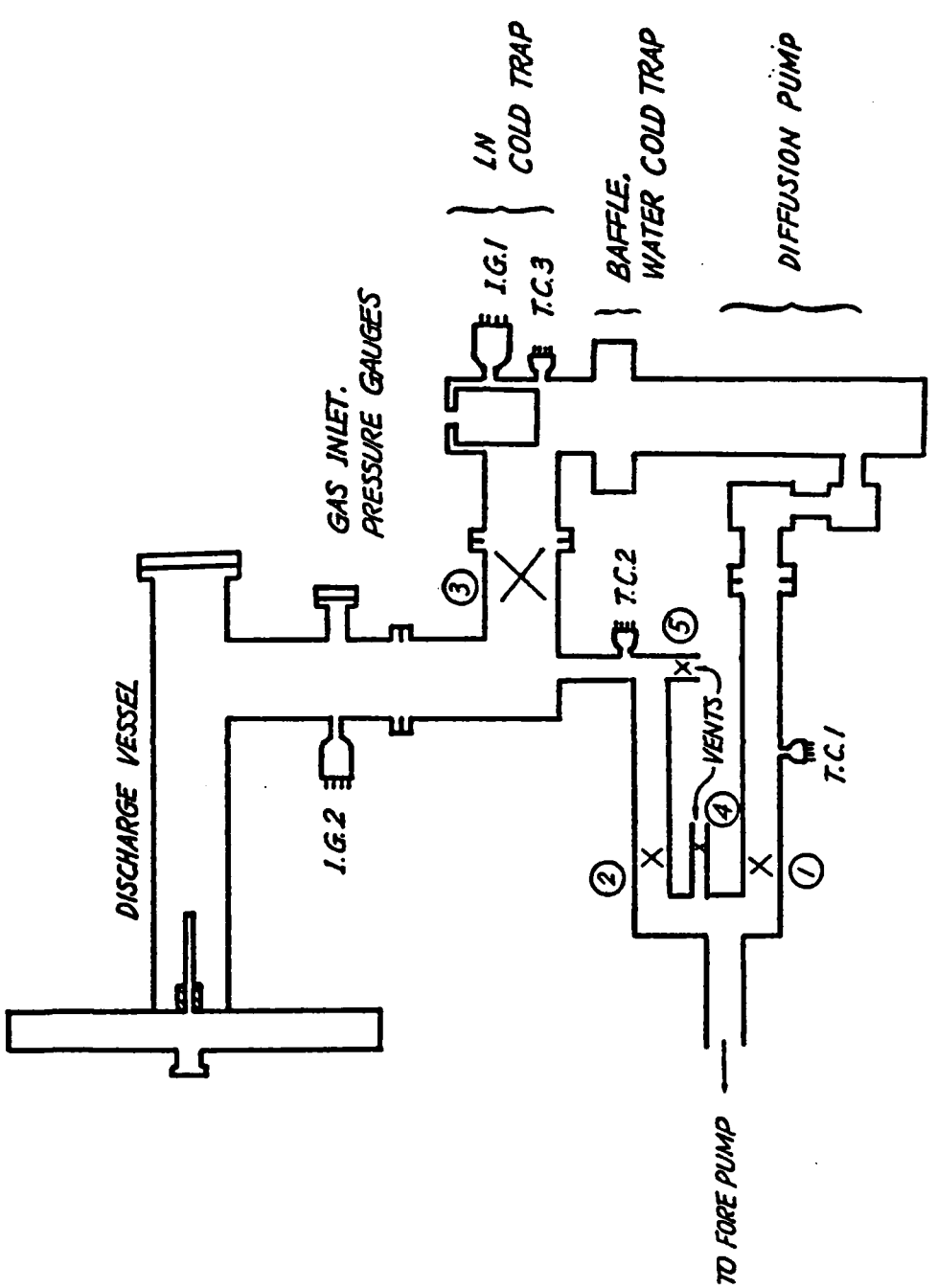


Figure 32. Schematic of Vacuum System.

is prefilled. Instead, we have used a Convectron thermocouple gauge which measures gas thermal conductivity and infers pressure. This method is gas-type dependent and not reliable because heat conduction and radiation to the thermocouple are easily affected by contaminants absorbed on the thermocouple surface. This somewhat inaccurate gauge will be replaced with a Wallace-Tiernan diaphragm gauge.

The valves used in this system are standard Veeco bellows valves with squashed 1/4-in copper pipe connected between them and the gas cylinder lines to restrict flow. From a leak standpoint these valves are excellent; initially ordinary nonbellows type needle valves were used, which were found to leak badly. The control available is not quite adequate, however. It is hoped to replace this arrangement with a combination of a high quality shut-off valve in series with a bellows needle valve for each gas.

Short-Circuit Measurements

Short-circuit tests are used to check out the system without a load. The current monitor can then be calibrated, firing characteristics of the switch can be examined, and total system inductance and resistance without a load can be measured.

We made these short-circuit tests by replacing the discharge vessel with a cylinder of brass with a threaded central hole. A special CE was threaded into this hole, shorting out the load. With this short-circuit arrangement, the initial system inductance, excluding the 2 to 4 nH of the 3 to 5 cm breakdown length within the gun, can be calculated from the system capacitance and the short-circuit ring time.

The bank voltages in the short-circuit tests were 40 and 50 kV. The gap spacing for the rail-gap switch was that specified by Maxwell for 50 to 100 kV operation. At this setting, a gas pressure was not specified for 40 kV, so the gas pressure specified for 50 kV was used. The calculated system inductance was different at the two voltages, presumably due to changes in switch behavior. Typical short-circuit waveforms are shown in Figure 33.

50kV

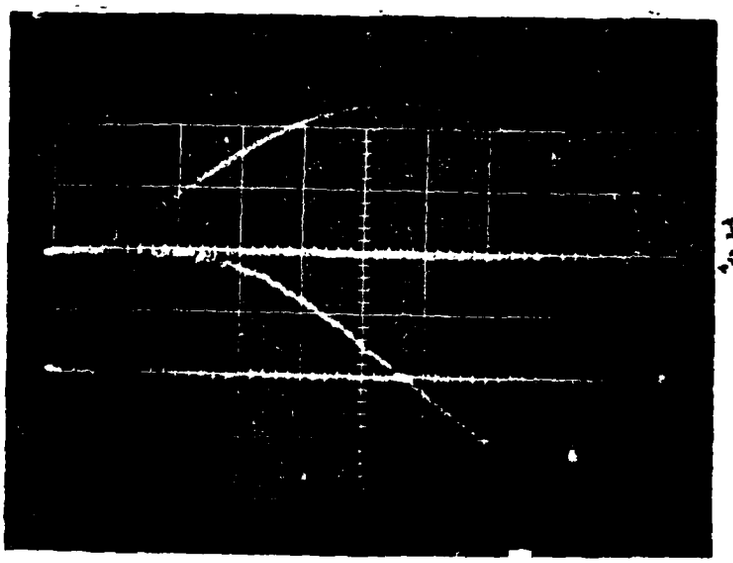

I
0.5 V/cm

$\dot{I}$
20 V/cm

9/9/83

200 ns/cm

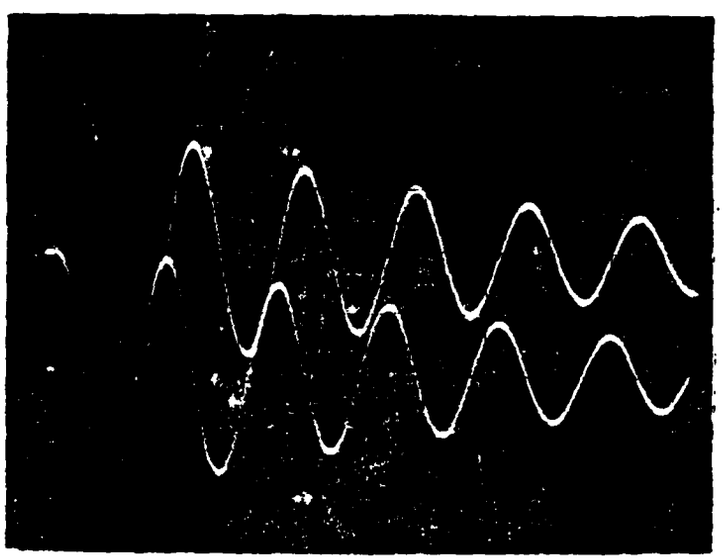

I
0.5 V/cm

$\dot{I}$
20 V/cm

9/9/83

2 μs/cm

Figure 33. Typical Short-circuit I and $\dot{I}$ Waveforms.

The analysis used here is for an underdamped LRC circuit. It was initially assumed that damping was small in the expression for current:

$$I = I_{sc}\, e^{-\alpha t} \sin(\omega' t) \qquad (31)$$

where $\omega' = (\omega^2 - \alpha^2)^{1/2}$, $\omega = (LC)^{1/2}$ and $\alpha = R/2L$. This amounts to assuming that $\omega' = \omega$, which permits an estimate of system L and $\alpha$ and, thereby, R. From this estimate for $\alpha$, the error in assuming $\omega' = \omega$ can be obtained.

The equations of interest are

$$L = \frac{1}{C}\,\frac{2}{\pi}\left(\frac{\tau}{4}\right)^2$$

$$Z_o = \left(\frac{L}{C}\right)^{1/2}$$

$$I_{sc} = \frac{V_o}{Z_o}$$

$$\dot{I}_o = \frac{V_o}{L}$$

The 50 kV shot gave $\tau/4 = 960$ ns. The C was calculated from the values on the capacitor labels: $C = 2.775$ μfd. Using these values, $L = 135$ nH, $Z_o = 200$ mΩ, $I_{sc} = 227$ kA, $\dot{I}_o = 3.7 \times 10^{11}$ A/s is obtained.

The damping was obtained by plotting logarithms of the peaks of current, normalized to the first peak. This gave $\alpha = 7.0 \times 10^4$ s, $1/\alpha = 14.3$ μs, $R = 19$ mΩ. This procedure is also slightly inaccurate since the first peak is reduced by exponential damping. This error can be reduced by iteration. With this first estimate $\alpha$, $\alpha^2/\omega^2 \sim 10^{-4}$ so $\omega' = \omega$ is valid to about 1 percent.

Next we obtain a first estimate for $e^{-\alpha(\tau/4)}$. With the first estimate of $\alpha$, $e^{-\alpha(\tau/4)} = 0.935$. We use this value to renormalize the current peaks. This gives $\alpha = 7.35 \times 10^4$ s, $1/\alpha = 13.6$ μs, $R = 20$ mΩ.

Now $e^{-\alpha(\tau/4)} = 0.918$. Further iteration would yield more accurate values but this accuracy is not justified by the basic measurements obtained from the oscilloscope traces.

Using $e^{-\alpha(\tau/4)} = 0.918$, the current peak a $\tau/4$ is 208 kA. With a passive integrator of time constant RC = 20 $\mu$s, the voltage peak was 12 V, giving a current sensitivity of 17.4 A/s•V.

The 40 kV shot gave $\tau/4$ = 1080 ms, L = 170 nH, $Z_0$ = 248 m$\Omega$, $I_{sc}$ = 161 kA, $\dot{I}_0$ = 2.4 x 10" A/s. The large increase in L is presumably due to fewer channels forming in the rail-gap switch. We anticipate that higher voltages will result in better multichanneling, though this is also affected by gas pressure. Since most operation was at 60 kV or above, we take the 50 kV results as more characteristic of device operation.

## 3. EXPERIMENTAL STUDIES PERFORMED WITH THE UNM HVDPF

In this paragrah experimental results obtained with the UNM HVDPF are discussed. Five types of diagnostics were used: gun header current and voltage measurements; time-resolved, filtered x-ray PIN measurements of the pinch region; fast framing visible light photographs of the sheath in late stages of development; B probe measurements of the current sheath; and time-integrated x-ray pinhole photographs. Each of these types of measurements are discussed separately, though some overlap inevitably occurs.

### Gun Header Current and Voltage Measurements

The current measured by the ground plate Rogowski loop is the total current flowing within the discharge vessel. Current measurements within the discharge region can determine if all current flowing in the discharge vessel flows in a single sheath. Alternate current paths are: along the insulator, secondary sheaths or restrikes. Because of the lack of extensive current measurements within the discharge vessel it is assumed that current is not diverted from a single sheath.

The voltage measured at the gun header is

$$V = IR + \frac{d}{dt}(IL) \tag{32}$$

This measured voltage consists of an inductive part and a resistive part. Reference 7 has made a nearly resistive measurement of the voltage across the sheath with a coaxial voltage probe at the end of the CE. This permits measurement of sheath resistance until the probe is destroyed by sheath arrival. This measurement allows one to know the separate contributions of resistive and inductive voltage drops in order to calculate device inductance, joule heating of the sheath and kinetic energy of the sheath, among other things. Lacking this measurement, we have resorted to various assumptions to extract as much information as possible from our two electrical measurements. A typical set of V, I, I, and X waveforms is shown in Figure 32.

## Sheath Formation Energy and Early Sheath Resistance

The gun header voltage and current waveforms can be used to estimate sheath formation energy before lift-off, assuming a low L breakdown, resulting in a forming sheath with constant inductance until lift-off. It is also assumed that this inductance can be accurately estimated from the geometry of the break-down region. More realistically, from breakdown until lift-off, the sheath undergoes inductive changes due to merging of plasma channels along the insulator or changes in plasma channel cross section due to radius changes or departures from circularity. There is also the possibility of diffuse break-down, which greatly complicates inductance estimates. But if these assumptions are approximately true, during this time most of the voltage measured at the gun header will be electrostatic, with a small $\dot{I}L$ contribution which can be calculated and subtracted from the measured voltage.

Figure 33 illustrates the use of voltage and current waveforms to estimate sheath formation energy. The voltage measured at the gun header is given by Equation 32. By assumption, $\dot{L} = 0$. The geometrically-derived constant initial inductance across the gun-header voltage probe is ~ 15 nH. We use this value and an average value of $6.2 \times 10$ in A/s for $\dot{I}$, obtained from Figure 34b, to obtain 9.4 kV for the $\dot{I}L$ contribution. The voltage correction is shown in Figure 34a. This voltage correction applies to the first 120 ns or so.

Assuming that $\bar{E}$ along the sheath is electrostatic, the kinetic energy, dW, given to an element of charge dq by $\bar{E}$ in going from the cathode to the anode is

$$dW = dq \int_c^a \bar{E} \cdot d\bar{\ell} = - dq \, \Delta V \qquad (33)$$

where $\Delta V$ is the potential difference between the electrodes. The last equality follows from the conservative property of an electrostatic field:

V
25 kV/div
$\dot{I}$
4.6x10" A/s.div

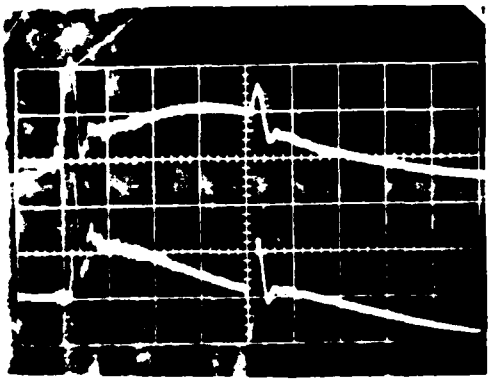

200 ns/div

a) V, $\dot{I}$

I
87 kA/div
X
10 v/div
Si PIN
2x10 $^{-3}$ cm Al foil

200ns/cm

b) I, X

Figure 34. Typical V, $\dot{I}$, I, X Waveforms.

$$\bar{E} = - \nabla V \tag{34}$$

where V has only spatial dependence. Thus the kinetic power given to charges crossing the electrode gap is

$$P = \frac{dW}{dt} = - I \Delta V \tag{35}$$

The time-independence of V is also used to obtain this equation. The kinetic power, P, is transformed into internal power by electron collisions, resulting in joule heating of the sheath plasma, which determines its temperature and conductivity.

The accelerator acts as a pure L (negligible R) after about 160 ns after break-down. Therefore, Figure 35c may be used to estimate sheath formation energy during the first 120 ns as ~ 76 J. Not all of this energy is retained as internal energy--some of it is radiated. There is also heat conduction to the insulator, to the gas surrounding the sheath, and to electrodes in contact with the sheath. During the ~ 100 ns before lift-off, these losses are expected to be small, so that ~ 76 J is a good estimate of internal energy of the sheath when it is formed. (Energy loss by heat conduction to the anode is not completely negligible, since significant CE vaporization damage by this contact has been noted.)

Finally, the derived electrostatic voltage and measured current is used to obtain sheath resistance (Fig. 33).

Rundown L(t)

Some time after the sheath forms, in this case 100-200 ns after current conduction begins, the IR drop across the sheath is negligible because sheath resistance drops to milliohms or micro-ohms. Therefore, between breakdown and sometime near pinch, the voltage measured at the gun header is mainly d/dt(IL). If sheath resistance were zero from the start of current conduction, the inductance of the accelerator would be given by

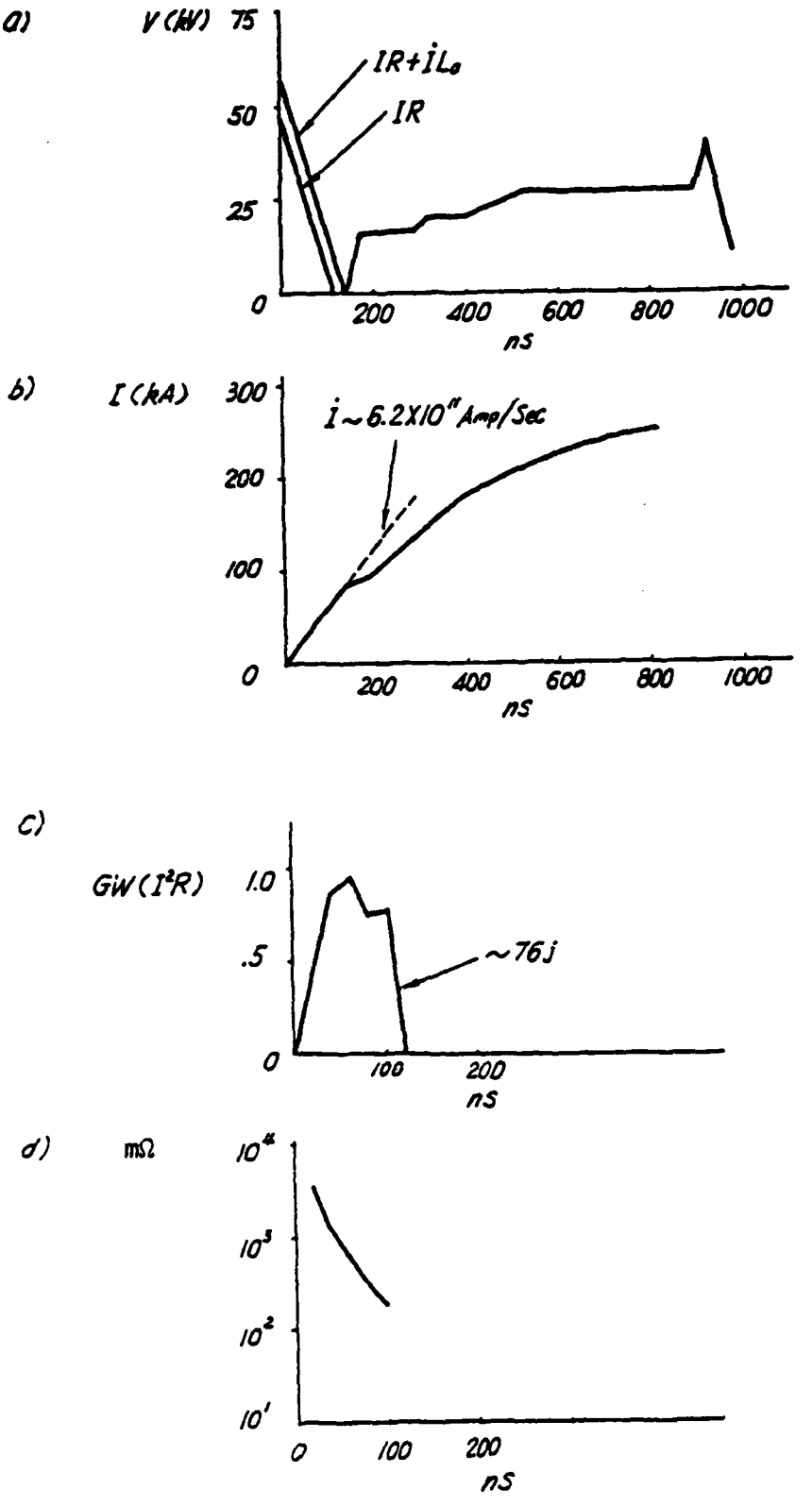


Figure 35. Quantities Used to Estimate Sheath Formation Energy.

$$L(t) = L_o + \int_0^t V(t')\, dt' \,/\, I(t) \qquad (36)$$

where $L_o$ is the low L breakdown inductance and V is the voltage measured at the gun header. In the previous subsection, an analysis was presented of early sheath resistance; Equation 36 is expected to be in error due to early IR voltage drop.

For zero IR drop across the sheath at all times and a sheath of constant profile moving--after some time, $t_\ell$, required for lift-off--at constant velocity, L(t) is expected to be as shown in Figure 36, from break-down to the start of collapse at $t_c$. The constant initial inductance is the low L break-down inductance. Upon lift-off at $t_\ell$, the sheath changes instantaneously, in this model, from a cylindrical shell to a planar piston. The slope of the curve for $t_\ell < t < t_c$ in Figure 37 is $\dot{L} = 2 \ln r_o/r_i \; v_s \; (m\Omega)$, $v_s$ in cm/$\mu$s.

Using voltage and current waveforms and Equation 36, one can evaluate L(t) in the absence of IR drop, as shown in Figure 35. Current conduction begins on the initial voltage rise, usually within $\lesssim$ 40 ns of the first voltage peak; a small error results by taking t = 0 for $\int_0^t V(t')\, dt'$ at the first voltage peak. This results in the curve shown in Figure 35b. The I(t) is taken from the waveform in Figure 35c. In Figure 35d we plot

$$\int_0^t V(t')dt' \,/I(t).$$

Due to early IR drop the break-down inductance from Figure 35d cannot be determined. It has been calculated from the geometry of the breakdown region to be 15 nH.

Figure 35d shows nearly constant $\dot{L}$ behavior between 200 and 600 ns. In this region, $\dot{L}$ ~ 56 m$\Omega$. An $\dot{L}$ of 42 m$\Omega$ was calculated from geometry, assuming a planar piston moving at 10 cm/$\mu$s. The discrepancy may be due to experimental uncertainty, nonplanar sheath

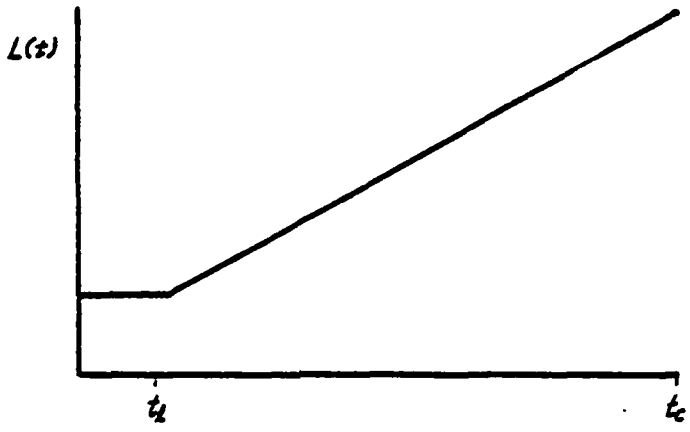


Figure 36. Idealized L(t).

motion or sheath velocity slightly above 10 cm/μs. Based on the time required for rundown, ~ 900 ns, and a rundown length of 12.3 cm, the sheath velocity would be ~ 14 cm/μs. However, there is reason to believe that this velocity is not constant, particularly near the end of rundown. The increase of slope in L(t) after 600 ns suggests that (1) collapse is beginning, or (2) the axial acceleration of the sheath due to small CE diameter is observable, or (3) the bullet shape of the sheath leads at later times to an L(t) different from that predicted by the planar piston model.

It may be possible to shift the curve in Figure 35d along the time axis using $\dot{B}$ probe or image converter lift-off time data, and along the vertical axis using initial inductance values and assumed values for $v_s$ and rundown length. This would permit a better match between the curves of Figure 34 and Figure 35d and possibly corroboration of the early sheath resistance values previously derived.

Focus

The main features of V and $\dot{I}$ collapse data are as follows. During collapse, $\dot{L}$ rapidly increases to several hundred milliohms. This rapidly decreases discharge current, producing a sharp negative $\dot{I}$ spike as shown in Figure 34b. A good focus converts a large amount of magnetic energy ($1/2\ LI^2$) to sheath kinetic energy. For a low impedance bank this results in current reduction by typically 15 to 30 percent of the current just before collapse. For this device, current reduction is small, as seen in Figure 34c. It is believed that this is due to high bank impedance current stabilization and to reduced final implosion velocity because of the use of a small CE diameter. A second consequence of high collapse $\dot{L}$ is a large pinch voltage due to $d/dt(IL)$. Generally, it is assumed that $I\dot{L} \gg \dot{I}L$.

With accurate time-correlation between V and $\dot{I}$ signals and assuming a highly conductive sheath during collapse, collapse $\dot{L}$ may be derived as has been done for rundown $\dot{L}$. These data lack sufficient time-correlation to carry out this calculation, though we anticipate obtaining good time-correlated data in the future. Other features of

the V and $\dot{I}$ data near pinch time are discussed as follows, pertaining to filtered x-ray PIN signals obtained near pinch time.

## X-Ray PIN Measurements

### Unfiltered PIN Signal

Useful x-ray signals were first obtained from $H_2$ fills with a few percent Argon added, using a silicon PIN x-ray detector with nominal 2 ns rise time, 5 ns fall time. This detector was a Quantrad 025-PIN-125 with 25 $mm^2$ of sensitive area, 125 μm active layer and 0.75 μm Si window. The spectral response of the detector is shown in Figure 38. The detector was at ~ 86 deg to the accelerator axis, viewing the end of the CE from slightly behind (towards the gun header), and the region beyond the CE where the pinch occurred. The vacuum/atmosphere interface was a piece of 2 x $10^{-3}$ cm, high-purity Al foil. The attenuation of this window is shown in Figure 39. The detector was placed 115 cm from the pinch, through 97 cm of air. Visible alignment of the detector was required so that it viewed the regions of interest. Two pieces of black photographic paper were initially placed over the detector because it is light sensitive and it was thought that light flashes from the focus or the rail-gap switch might affect the detector. It was later determined that this did not occur and the photographic paper was removed.

In calculating the x-ray emission spectrum, x-ray attenuation by air between the Al foil and the detector should be considered for soft x rays. There is also attenuation by that part of the sheath extending from the pinch back to the outer electrode, though this is probably negligible. An accurate calculation of this attenuation requires knowledge of sheath density and thickness in this region.

An electrical schematic for the PIN measurement is shown in Figure 40.

The DPF x-ray production without B-field stabilization is generally erratic in regard to total yield and temporal, spatial and energy characteristics. These data were no exception, though one characteristic of the x-ray emission frequently occurred with fillings of ~1 T $H_2$,

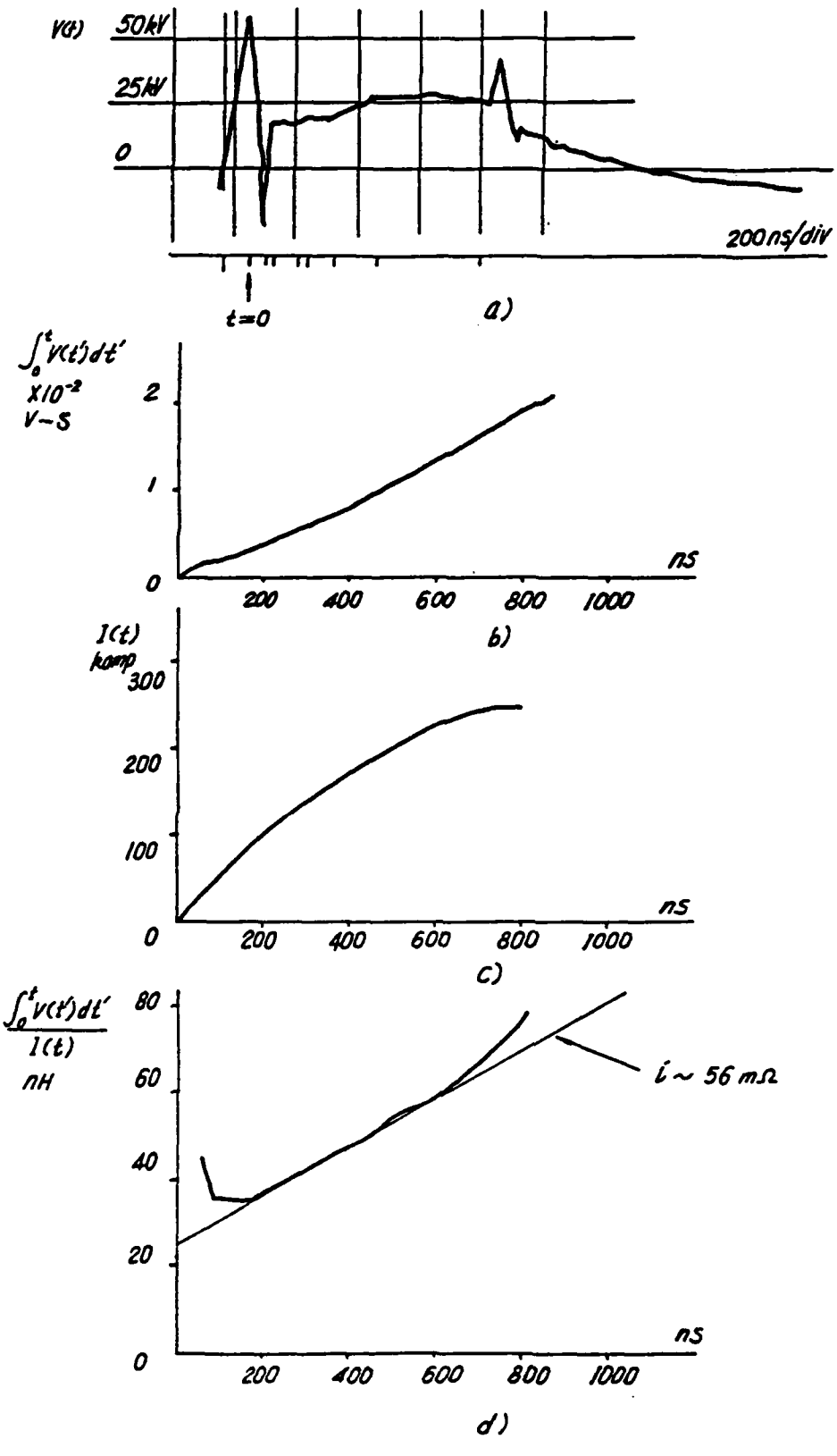


Figure 37. Quantities Used to Evaluate Experimental $\dot{L}(t)$.

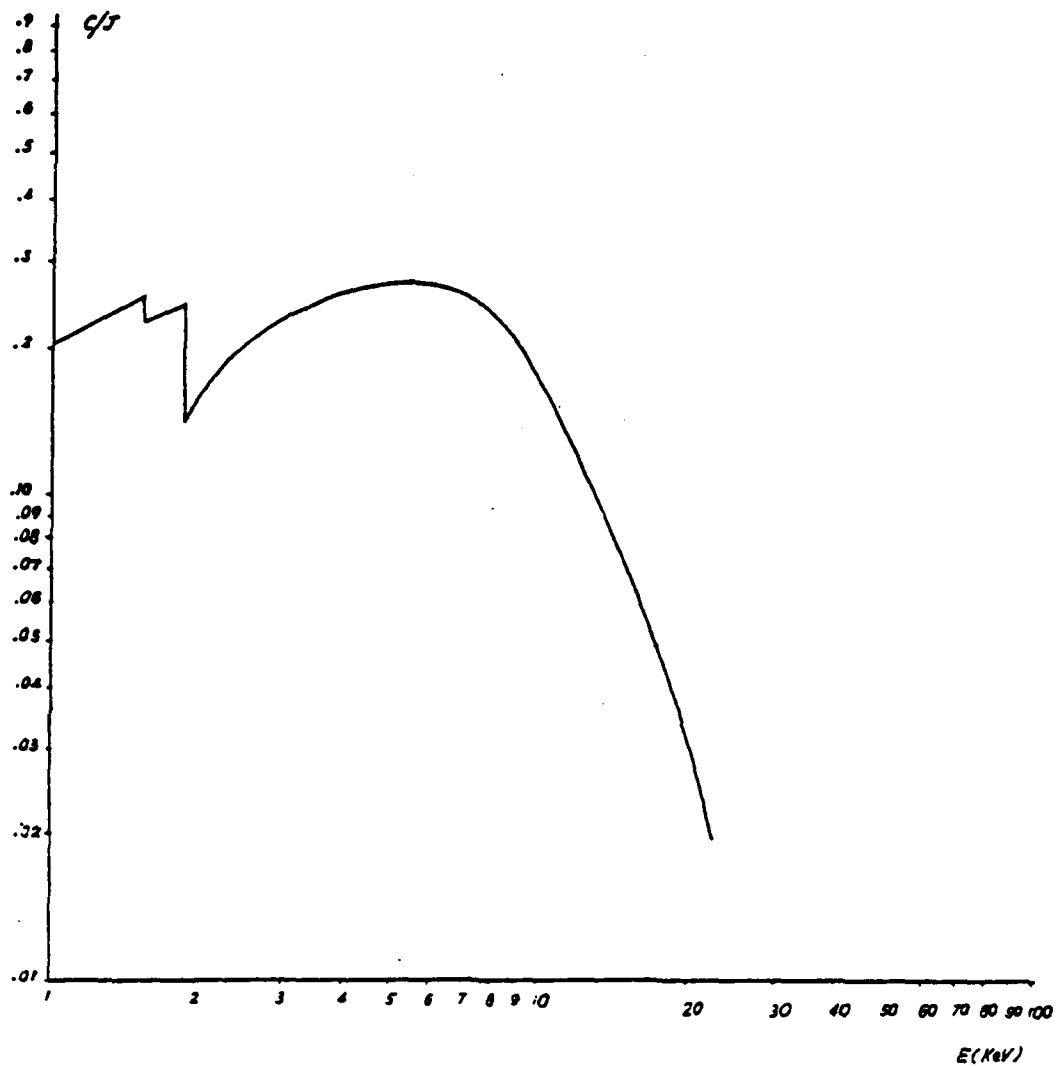


Figure 38. Si X-ray PIN Response.

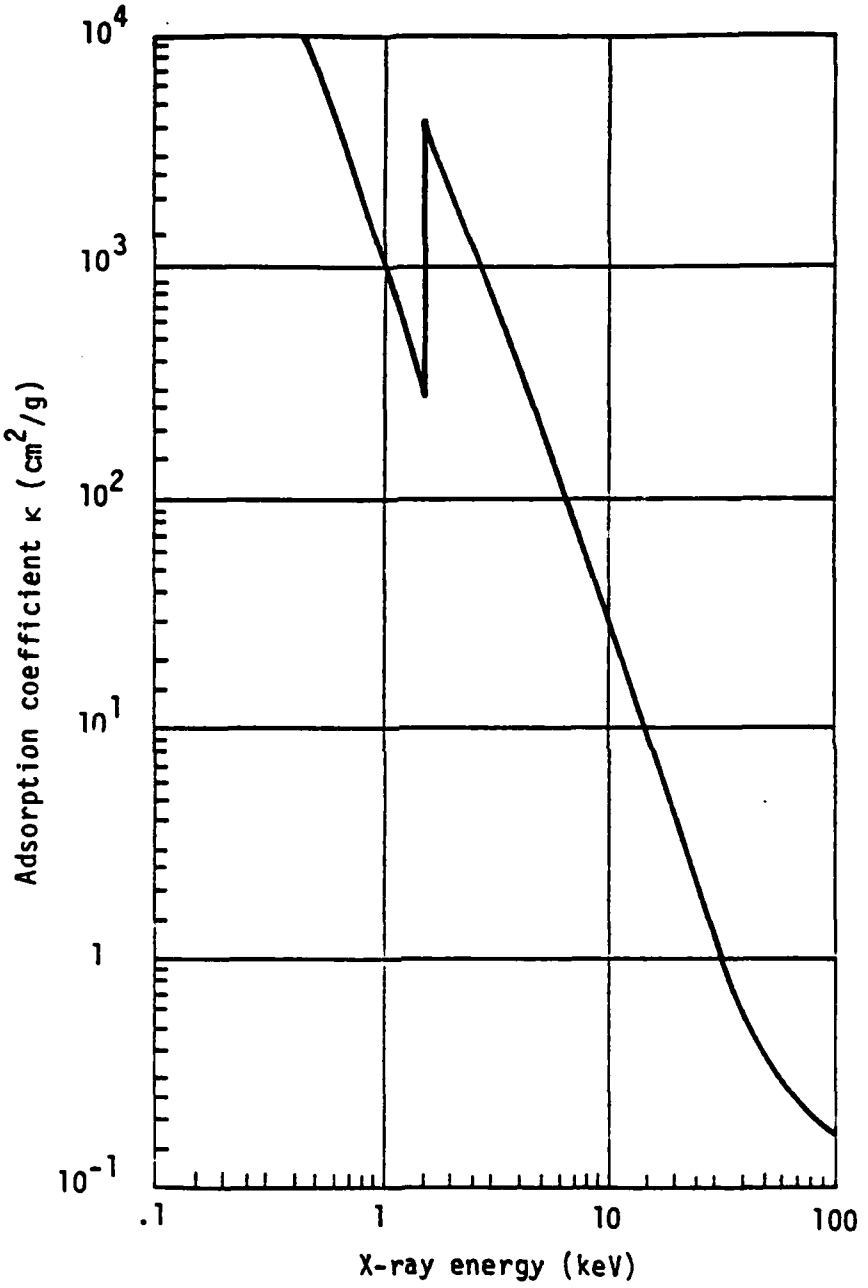


Figure 39. X-ray Absorption Coefficient of Aluminum.

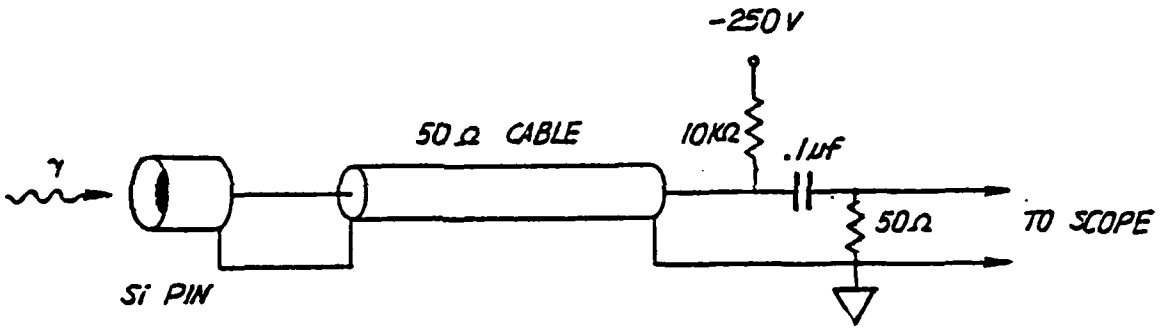


Figure 40. PIN Electrical Schematic.

3 to 5 percent A. Often a small amplitude, narrow (20 to 60 ns) pulse preceded by 40 to 80 ns a larger, broader (100 to 200 ns) pulse. Other workers have observed similar behavior in viewing the pinch region and CE tip side on (Ref. 44). Further, within the time correlation accuracy of the various scope traces, the first pulse seemed to occur near the time of the first large negative $\dot{I}$ spike, suggesting this pulse was produced by the pinch and the second pulse possibly by electron beam acceleration into the CE by large E fields created by pinch breakup. A typical unfiltered PIN signal is shown in Figure 34d.

The next stage in x-ray measurement was to use two filtered PINs to provide an estimate of the x-ray spectrum of each of the two x-ray pulses. This could clarify the x-ray production mechanism predominant in each pulse.

Filtered PIN Data and V and $\dot{I}$ Collapse Data

The traces in Figure 41 show time correlation of the two filtered PIN signals with V and $\dot{I}$ signals. These traces were obtained after using a time mark generator to align both beams near the center of each scope face.

The waveforms of Figure 41 are representative of most focussing shots at 80 kV, 1 T $H_2$, 3 to 5 percent A, but this is also the best data obtained at these parameters; these data have the highest amplitude $\dot{I}$ and V pinch spikes and first x-ray pulse. Most focussing shots have amplitudes slightly smaller than the values shown in Figure 41.

Having established that the first x-ray pulse occurs close to the negative $\dot{I}$ spike and the voltage spike, this pulse is probably produced by the pinch and is either characteristic of the electron temperature during or just after collapse or that it is produced by electrons accelerated by the pinch voltage spike. Because the second pulse starts up after the electrical signals associated with collapse, it is also reasonable to assume that the second pulse is due to electron beams created by pinch breakup. Before discussing the x-ray pulses further, some peculiarities of the V and $\dot{I}$ collapse data are discussed.

One peculiarity of the $\dot{I}$ trace is the relative amplitudes of the negative and positive $\dot{I}$ spikes. In many focussing shots the positive $\dot{I}$

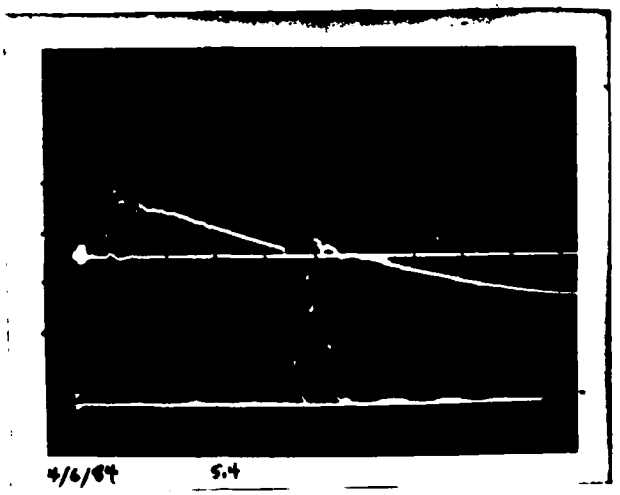


$\dot{I}$

4.6 x 10in

A/s.div

X1

20 V/div

200 ns/div

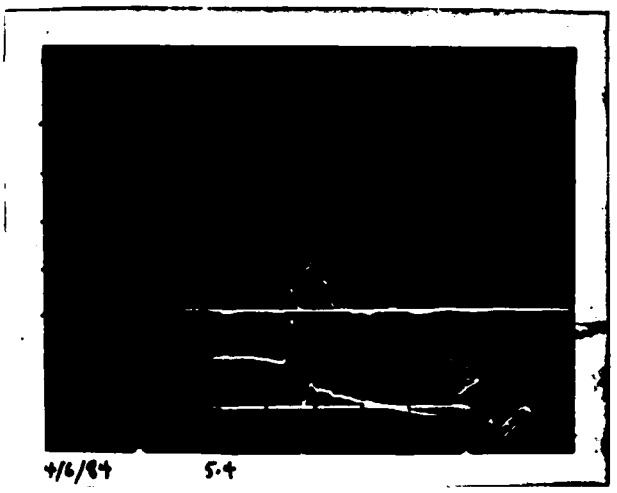


X2

20 V/div

V

25 kV/div

200 ns/div

Figure 41. Correlation Between Filtered PIN Signals and V and $\dot{I}$ Signals.

spike is larger than the negative $\dot{I}$ spike. If these spikes were due only to radial motion of a perfectly conducting plasma column, one might expect some degree of bouncing to produce a positive $\dot{I}$ spike of amplitude less than (or equal to, for a perfectly time-reversed bounce) the amplitude of the negative spike. This assumes decoupling between the current source and the pinch load. Such decoupling might be expected for the high impedance of a high voltage bank and for a primarily coaxial geometry where sheath motion occurs only in the vicinity of the pinch during collapse. Such restricted plasma motion is the case in a conventional plasma focus where plasma stagnates against the inside of the OE so that conduction is along the surface of the plasma. However, in this case the bullet shape of the sheath during rundown suggests that the sheath never reaches the OE and that during collapse and after, the current changes resulting from pinch inductance changes may affect sheath behavior behind the pinch. This could permit communication between the pinch and the sheath behind the pinch which could enhance the positive $\dot{I}$ spike. One argument against this is that the time scale of the pinch is too short, say 100 ns, for significant motion to occur in the sheath behind the pinch.

Another peculiarity of this data is in the voltage waveform. In most plasma focus devices, including those of Decker, the voltage measured at the gun header decreases just before the voltage spike. This is because near pinch, $\dot{I}L$ is nearly zero ($\dot{I}$ is nearly zero) and the header voltage is mainly $I\dot{L}$, where $\dot{L}$ is rundown $\dot{L}$ (usually 10 to 20 mΩ). Assuming 20 mΩ and 250 kA just before pinch, a voltage measurement of ~ 5 kV would be expected. Instead, ~ 25 kV was observed before collapse, which suggests that $\dot{L}$ is much higher than this, as much as 100 mΩ. This is roughly twice the 42 mΩ calculated for this device assuming a planar piston moving at 10 cm/μs. However, we have noted that an $\dot{L}$ of 42 mΩ is lower than the measured $\dot{L}$; 13 to 14 cm/μs is more likely and an increase in $\dot{L}$ just before collapse has been observed, consistent with the bullet-shape of the sheath. Another point is that with the large $\dot{L}$, small values of $\dot{I}$ near pinch time will

result in larger IL values than for devices with smaller $\dot{L}$. This is offset somewhat by the correspondingly reduced rundown length.

Finally, though the data in Figure 41 is the highest amplitude data obtained for the specified operating parameters, these data (and the bulk of the rest at smaller amplitudes) show negative $\dot{I}$ spikes and V spikes and pinch x-ray pulses significantly lower than those obtained by most plasma focus workers. This suggests that the collapse does not have enough time to impart large radial kinetic energy to the sheath to produce a higher temperature pinch. This is supported by x-ray pinhole pictures which show brightness near the CE face (due probably to beam-produced x rays), but only a faint line from the pinch. Most plasma focuses show a bright x-ray plume where the focus occurs.

More collapse time can be obtained by increasing CE diameter. This remedy may also improve the precollapse geometry so that a longer, more linear z-pinch is obtained. For this and other reasons a larger CE diameter will be used in future experiments.

For the data shown in Figure 41, the PIN detectors viewed both the pinch region and the CE face, so x rays observed near pinch time could be due both to pinch plasma thermal bremsstrahlung and possibly to electrons accelerated into the CE face by the large pinch voltages indicated by large pinch-time gun header voltages. Pinch-time beam x-ray production from CE bombardment can be excluded from measurement by limiting the detector field of view to the pinch region. However, with the present data, pinch time beam x-ray production from CE bombardment seemed unlikely for two reasons. First, there are many shots with a voltage spike but no pinch time x-ray pulse. This often occurs when too much Argon is added. Though Argon enhances thermal Bremsstrahlung for a given temperature plasma, too much Argon slows radial collapse so that the high final collapse velocity required for thermal radiation pinch x-ray yield is not obtained. Reduced radial implosion velocity will also reduce the amplitudes of the negative $\dot{I}$ spike and the voltage spike because $\dot{L}$ is reduced. This is in fact observed for high Argon content shots. However, usually the voltage

reduced, so that sufficient electron accelerating potential is present for significant CE bombardment x-ray production. But this is not observed near pinch time for high Argon shots, which suggests that the first x-ray pulse is due almost entirely to thermal bremmstrahlung of the pinch plasma.

A more convincing argument against pinch time beam x-ray production is that the electric field produced by Faraday's law in a z-pinch is radial: electrons will be accelerated towards the axis, not along it. The focus is a two-dimensional pinch, so some axial electric field will be produced, but most of the gun header voltage measured at pinch time is due to $I\dot{L}$ resulting from primarily radial compression. Note that the time-resolved data presented in Reference 44 has the same structure--two pulses, the first correlated with the negative I spike--and that those scientists observed this structure when their detectors viewed only the pinch region or both the pinch region and the CE. If the first pulse were due to pinch voltage acceleration, it would be expected to be enhanced when the CE was included in the detector's field of view. For these reasons it is assumed that the first x-ray pulse is due to thermal bremmsstrahlung.

For the second pulse we assume x-ray production by Bremsstrahlung radiation of electrons slowing down in the face of the CE. Since several electron beams of different energy, current, duration, and position have been observed by other workers, it is reasonable to suppose that the sometimes intricate structure evident in the second pulse is due to superposition of several electron beams. This makes it difficult to characterize the exact production mechanism of this second pulse because one must decide at various times during the second pulse what sort of electron beam(s) is (are) being produced--monoenergetic or power law, for example. Given the doubtful accuracy of two detector absorption spectroscopy, this sort of inference is speculative without supporting measurements such as Faraday cup and/or energy analyzer measurements. This sort of analysis seems even more speculative when one considers recent neutron production mechanism theories where non-linear phenomena such as turbulence and solitons are thought to lead to

high accelerating fields which cannot reasonably be characterized by temperatures or well-defined electron beams. To get an idea of the average behavior of the X ray producing electron beams, an attempt was made to analyze the response ratio data for the second pulse on the basis of an electron beam.

The PIN response ratios were obtained as follows. First, both unfiltered detectors viewed approximately the same region within the discharge chamber through a 1 mil Al foil window. This foil was Reynold's wrap, which is annealed and stronger than high purity foils which often could not support the vacuum-atmosphere pressure difference. Reynold's wrap has the following by weight contents: 98% + Al, 1.1-1.3% Si, 0.4% Fe, trace amounts of Cu, Zn, Mg and Mn. Presumably differences in the two unfiltered detector signals would be due to: (1) differences in detector surface orientation relative to the line of sight to the pinch region, (2) intrinsic detector differences, (3) differences between the 50 $\Omega$ termination resistors across which detector currents are measured (the circuit is shown in Figure 40), (4) differences in scope gains, and (5) differences in viewing area. About ten x-ray producing shots were taken and response deflections on the oscilloscopes were measured at peaks in the x-ray pulses and places where pulse structure was clearly evident in both signals. This permitted an estimate of 1.20 for the response of detector X2 to that of detector X1. This correction factor was applied to subsequent shots in which 4 mils of Al foil were placed in front of detector X2.

For the data of Figure 41, PIN response ratios were obtained of 1.67 for the first x-ray pulse and 1.82 for the second x-ray pulse.

Electron Temperature Measurement

As indicated previously, a complete calculation of plasma thermal Bremsstrahlung includes free-free, free-bound and bound-bound radiation, which requires knowledge of charge state populations of all ion species. These populations are temperature- and density-dependent; the calculation is difficult and ultimately requires iteration. For higher

energy plasma focus devices it is common to include copper contamination in the calculation. However, if we assume a pure, fully ionized plasma and only free-free transitions, we have the following [4,85] for emitted spectral power density (Ref. 7 and 44).:

$$\frac{dP}{d\lambda} = 6.01 \times 10^{-30} \frac{n_e}{T_e^{1/2} \lambda^2} e^{-12.40/\lambda T_e} \left[\sum g_{ff} (n_i Z^2)\right] \qquad (37)$$

P is in $W/cm^3$, $T_e$ in keV, $\lambda$ in Å, $g_{ff}$ is the free-free Gaunt factor, $n_e$ is the electron density in $cm^{-3}$ and the summation is over each ion species.

For $T_e$ determinations, only PIN response ratios are required, so these scaling factors can be ignored, but dP/dE dependence is required on photon energy, E. Also, a single ion species is assumed. For constant $n_e$, $n_i$,

$$\frac{dP}{dE} \propto \frac{e^{-E/T_e}}{T_e^{1/2}} \qquad (38)$$

This gives dP/dE dependence on photon energy for various electron temperatures. This dependence is plotted for several electron temperatures in Figure 42.

A pinch electron temperature determination was attempted using filtered PIN response ratios. This gave an electron temperature well over 10 keV. Typical DPF electron temperature measurements are in the 1 to 2 keV range. It was decided that 10 keV was unreasonably high, particularly with the reduced compression dynamics expected with the small CE diameter. To get an idea of the energy of the x rays emitted by this device, response ratio was calculated for the two filtered PINs as a function of incident photon energy. This ratio is shown in Figure 43. From this figure it can be seen that monoenergetic x-rays in the 10 to 12 keV range would give response ratios of 1.6 to 1.8. Without better energy resolution afforded by additional filtered PINs or a

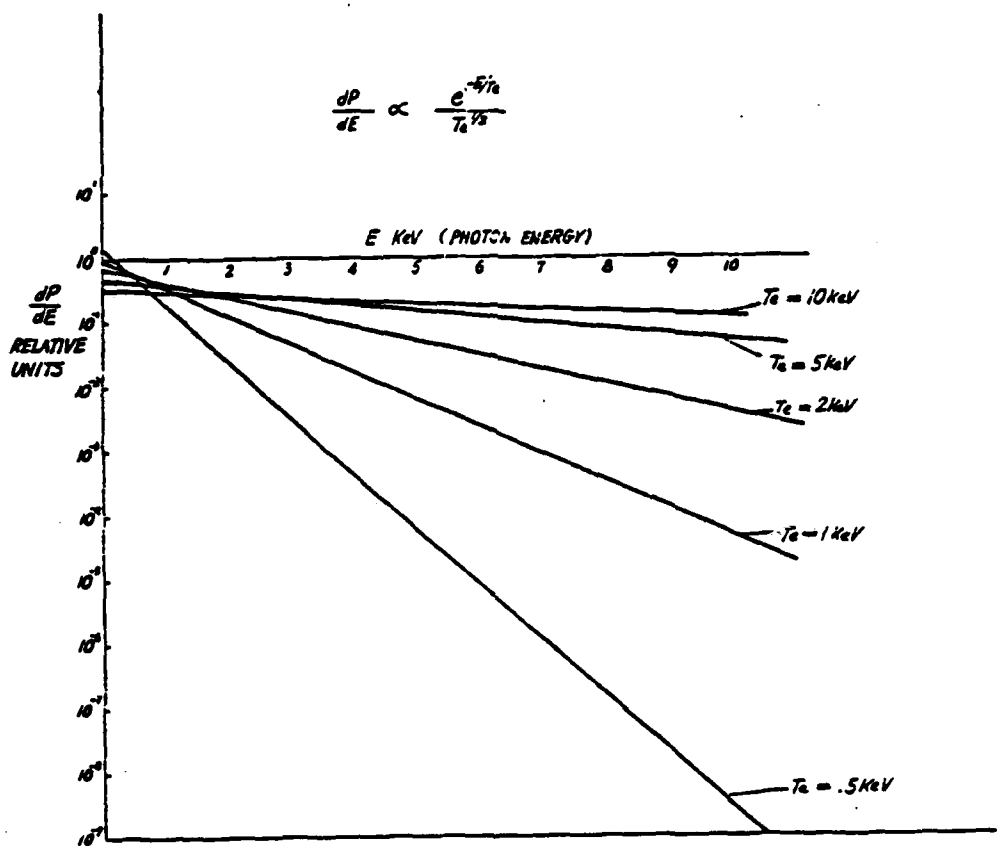


Figure 42. Thermal Bremsstrahlung Spectra for Pure, Constant Density, Fully Ionized Plasma with No Recombination Radiation.

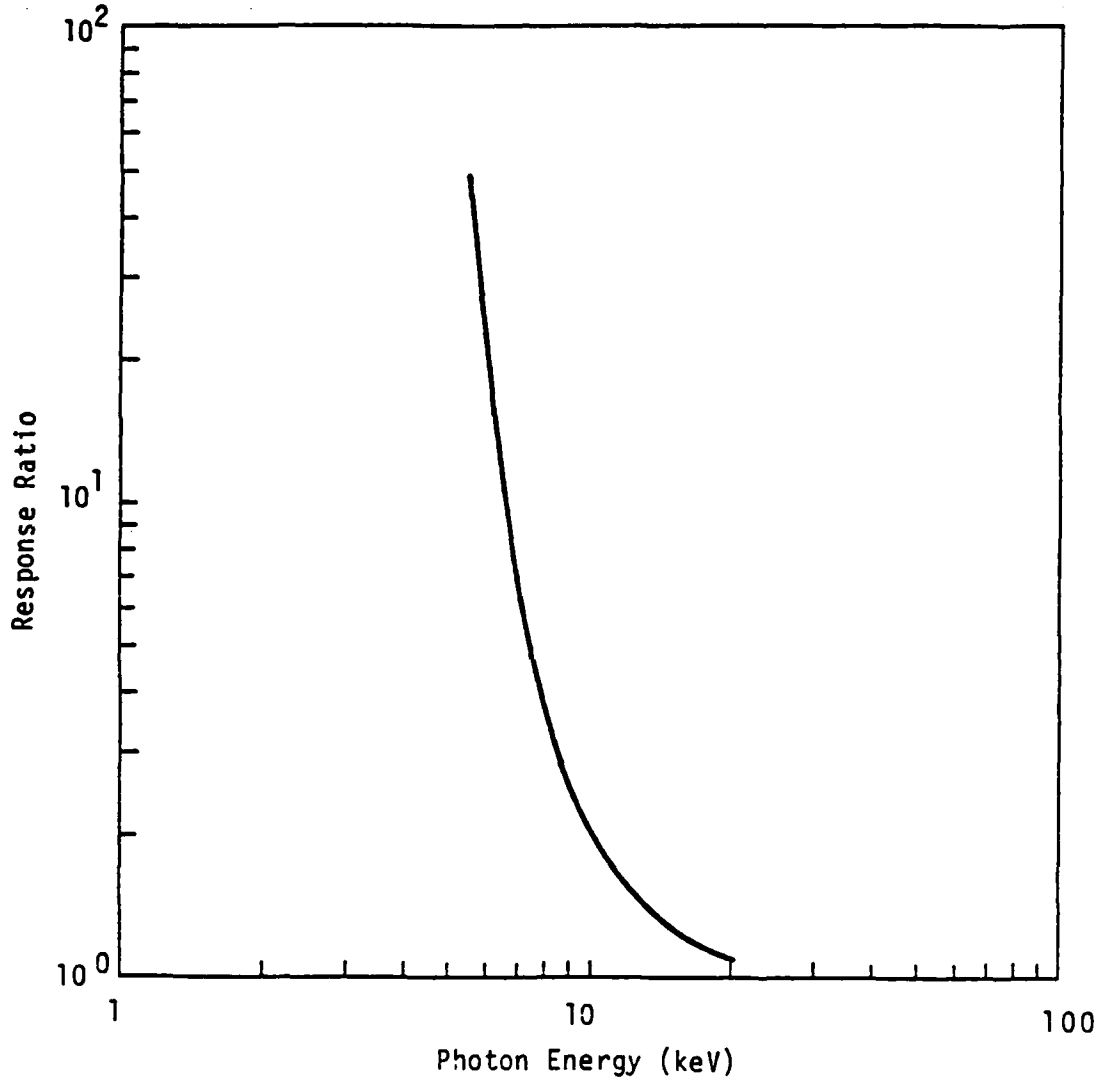


Figure 43. PIN Response Ratios for 1 mil Al Filter and 5 mil Al Filter.

diffraction x-ray spectrometer, we can only speculate on the origin of x-rays which have some mean in the 10 to 12 keV range.

First, it is surprising that the first x-ray pulse does not appear to be predominantly thermal in origin. However, a full stripped, thermalized hydrogen plasma spectrum could be masked by Argon line emission. This effect has not been calculated. It would be instructive to rule out this possibility by examining x rays produced in a pure $H_2$ plasma.

The first x-ray pulse may also be due to an electron beam. There may be insufficient axial inductive electric field due to collapse to accelerate electrons into the CE. However, accelerating electric fields may arise stochastically (Ref. 21). In this case, an x-ray spectrum typical of electron beams incident on Cu, would be expected, i.e., continuum Bremsstrahlung with Cu lines superimposed. The copper $K_\alpha$ line is at ~ 9 keV, close to the 10 to 12 keV range of these data. Others have shown significant x-ray emission up to 100 keV and above (Ref. 20 and 54). The copper $K_\alpha$ line could easily be weighted towards the hard end of the spectrum.

$\dot{B}$ Probe Measurements

The main purpose of a $\dot{B}$ probe measurement was to roughly determine the thickness of the current layer. It is claimed that high voltage plasma focus sheaths are much thinner than those of lower voltage devices, due to increased sheath formation energy, due to higher break down voltage and $\dot{I}_0$ (Ref. 12). This results in a hotter, more highly conductive, thinner sheath. Sheath thickness has been measured with 100 ps exposure time Schlieren photographs which show sheath thickness, from electron density gradients, of ~ 1 mm. Measurements of current layer thickness in conventional devices gives $\gtrsim$ 1 cm. However, it is well known that density gradients and current gradients do not necessarily coincide in a shock of this type. Therefore, it is of interest to compare a current sheath thickness measurement of a high voltage plasma focus with previous current sheath thickness measurement of conventional devices.

Ideally, one can measure sheath thickness by measuring the spatial gradient of magnetic field with several $\dot{B}$ probes placed at constant distance from the accelerator axis but different axial positions. A quick measurement was wanted and, therefore, a single $\dot{B}$ probe measurement was chosen. With a rough estimate of sheath rundown velocity of 14 cm/ s, sheath thickness from the width of the time gradient of the B field measured at a single position can be estimated, assuming most of the motion past the probe is axial.

For a 1 cm thick sheath moving at 10 cm/ s, we expect a B field time gradient width of 100 ns can be expected. For a 1 mm thick sheath, the width would be 10 ns. Thus, a rough, quick determination of the current layer thickness can be made to prove or disprove the order of magnitude difference in current layer thicknesses between high voltage plasma focuses and conventional devices.

There are two basic problems with this measurement: the rise time of the $\dot{B}$ probe due to its inductance, and possible shielding of fast magnetic signals from the probe by ionized material ablated from the probe outer jacket by contact with the hot sheath.

The $\dot{B}$ measurements were obtained with a probe consisting of two loops of No. 32 enameled copper wire. The loop radius was 1 mm. The loop was epoxied into one end of a length of 0.025 cm wall, 0.317 cm OD brass tubing with two 0.036 cm wide, 2 mm long slots at the ends of a tube diameter over the loop to permit magnetic field penetration into the loop. The brass tube was then epoxied into a 5 mm OD high-purity alumina tube with a heat-fused tip. The center of the loop was 4 mm from the end of the alumina tube. The other end of the brass tube was soft-soldered to a brass adapter, which was in turn soft-soldered to a BNC connector. The sensitivity of a two loop probe is

$$V = 4 \quad \times 10^{-7} \frac{\dot{I} r^2}{R} \qquad \text{(SI)} \qquad (39)$$

This assumes purely axial azimuthally symmetric current in the CE. Here $\dot{I}$ is due to the current layer passing the probe; r is the loop radius and R is the radial distance from the accelerator axis. For r = 1 mm, a current of 250 kA, sheath thickness of 1 cm and sheath velocity of 10 cm/μs, we expect $\dot{I} \sim 2.5 \times 10^{12}$ A/s. For a probe located at 2 cm from the axis we would then expect a $\dot{B}$ voltage during sheath passage of ~ 150 V.

The $\dot{B}$ probe was placed as shown in Figure 44 at the two locations shown. Both locations were 2.15 cm from the end of the CE. For a sheath velocity of 10 cm/μs, this means that $\dot{B}$ signals should start $\lesssim$ 200 ns before collapse. The first radial position was at 1.9 cm from the axis, the second at 1.6 cm from the axis. Because the main purpose of the measurement was to obtain an estimate of sheath current layer thickness, the alignment of the loop plane normal to field lines was not done as carefully as possible. Data obtained from $\dot{B}$ probe measurements at 1.6 cm of off axis are shown in Figure 45. Because the sheath has largest axial velocity at the CE, $\dot{B}$ probe measurements farther from the axis reflect radial expansion of the sheath, a slow process resulting in a slower rise time in the measured B field. We conclude from data at various radial positions that the current layer is ~ 1 cm thick.

Fast-Frame Visible Light Photographs

Fast-frame visible light photography was attempted with a camera built at the University of New Mexico (UNM). This camera consists of an f2.5 lens imaging on a pair of proximity-focused photodiodes in series. There is a fiber optic plate on the output of the second diode permitting direct film exposure. Usually, very fast photography uses an image intensifier, such as a microchannel plate, to permit photography when the short exposure times (< 10 ns) required for plasma focus diagnostics allow limited amounts of light to reach the camera. However, it was hoped that with increased sheath brightness due to argon addition and possibly due to increased sheath temperature, an image could be obtained with this camera.

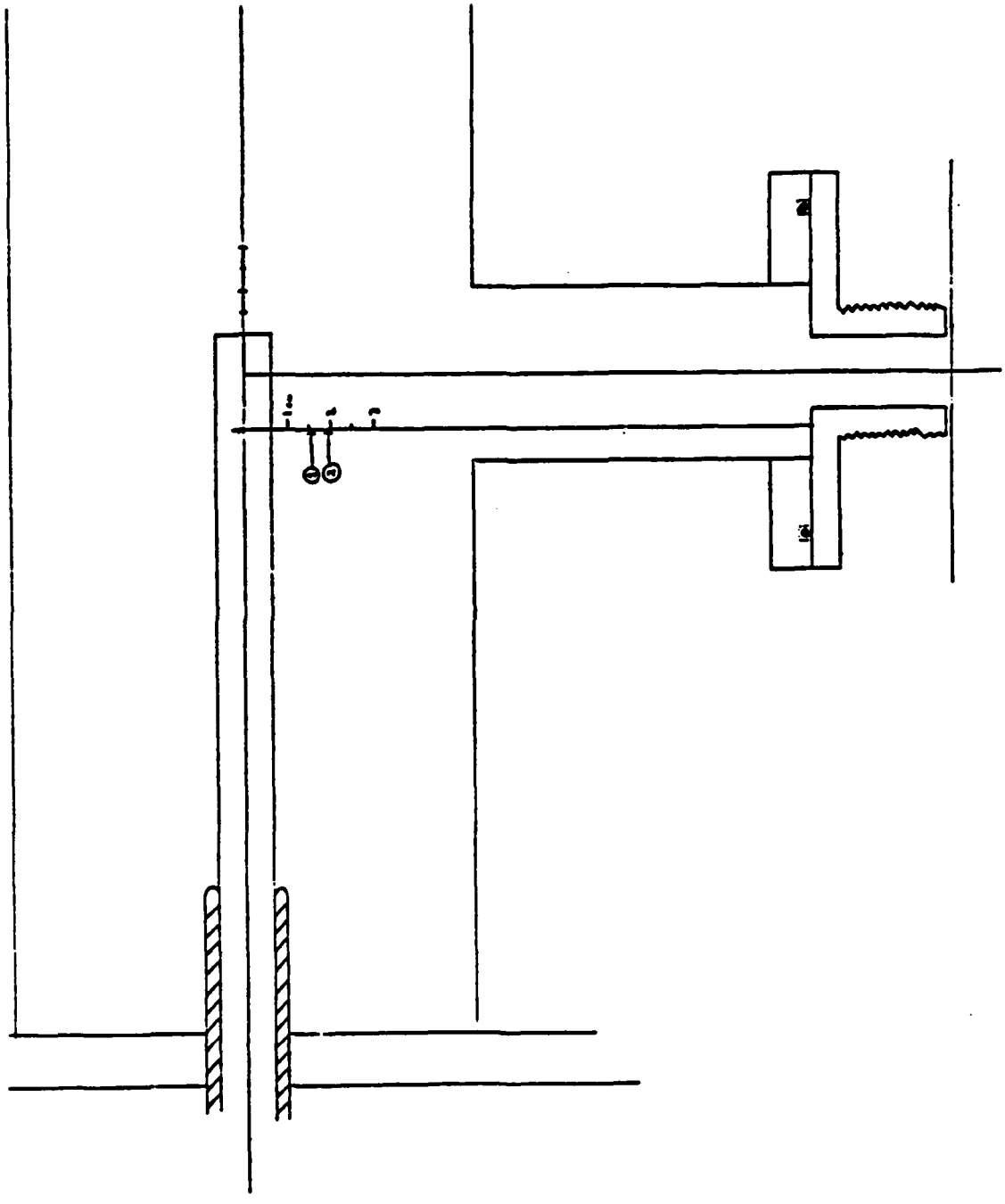

Figure 44. Locations of $\dot{B}$ Probe Measurements.

1.6 cm from axis

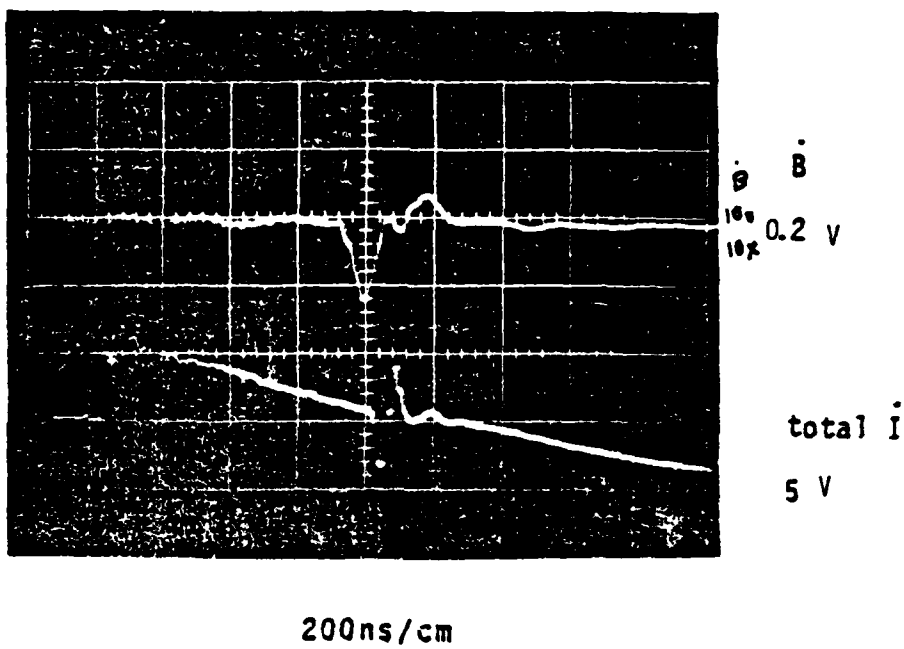


Figure 45. $\dot{B}$ Probe Measurement Obtained at 1 T $H_2$, 5% A, 80 kV.

Figure 46 is a reference photograph. The circle is the perimeter of the fiber optic plate. The CE is visible, more or less centered in the field. A flashlight illuminated the end of the CE, seen as a bright oval-shape at the right.

Figure 47 was obtained by pulsing the camera with a ~ 3 kV, ~ 40 ns pulse obtained from a Krytron pulser. This photograph was obtained with full lens aperture, maximum applied voltage on the photodiodes and Type 57 Polaroid film, ASA 3000.

The blurring to be expected in a 40 ns exposure of an infinitely thin (luminosity-wise) sheath moving at 10 cm/$\mu$s is 0.4 cm. The width of the bright region at the CE in Figure 47 is roughly 0.4 cm. From this it may be concluded that the luminous part of the sheath is much less than 1 cm.

It is possible that, as Decker suggests, higher voltage DPF operation produces a thinner sheath initially, but that the high current densities due to our smaller CE diamter draw electrode material into the discharge and thicken the sheath.

Another item of interest is the very faint part of the sheath visible away from the CE. Though the field of view is limited by the diagnostics port shown in Figure 29, some canting of the sheath profile near the CE is evident.

X-ray Pinhole Photographs

An indication of where x rays originate in the DPF may be obtained with x-ray pinhole photographs. These are made by imaging x rays through a small hole in a piece of lead. With a fast x-ray sensitive camera, framing or streak pictures are possible. In this case the results are time-integrated.

Examples are shown in Figures 48 and 49. These were made on Polaroid Type 57 film (ASA 3000). The magnification of the image is approximately 1:1. Pinhole diameters were 1.5 mm for Figure 48 and 0.5 mm for Figure 49. The distance from the pinhole to the film was ~ 25 cm in air, highly attenuating soft x rays.

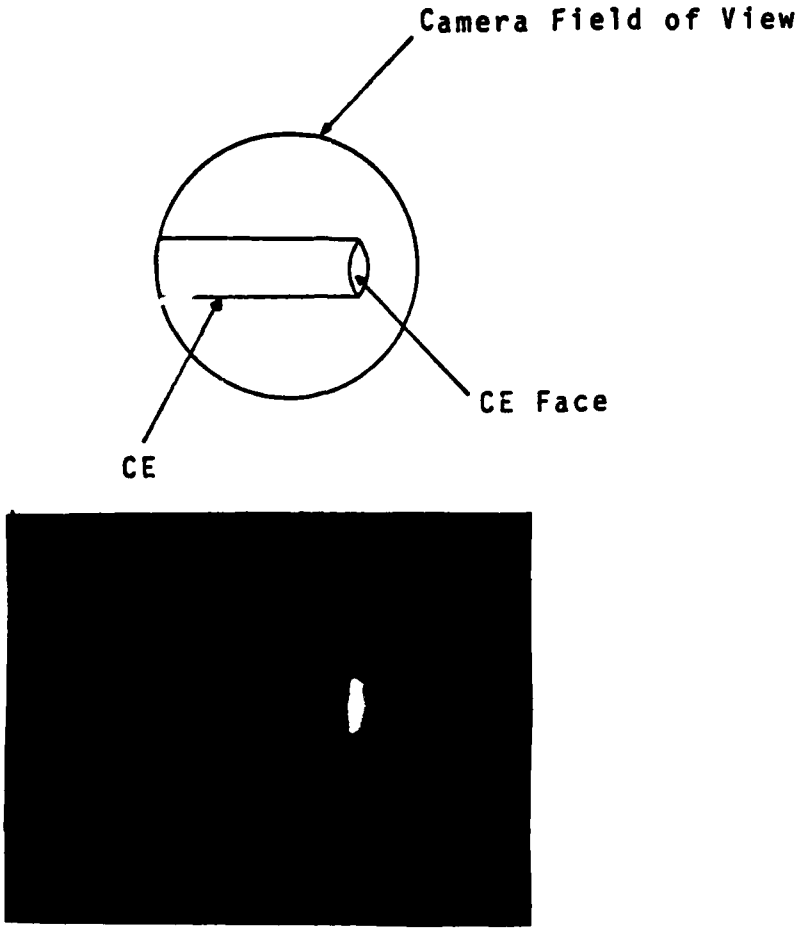


Figure 46. Reference Photograph for Fast-Frame Visible Light Photography of the Sheath. CE Face is Illuminated from the Right by a Flashlight.

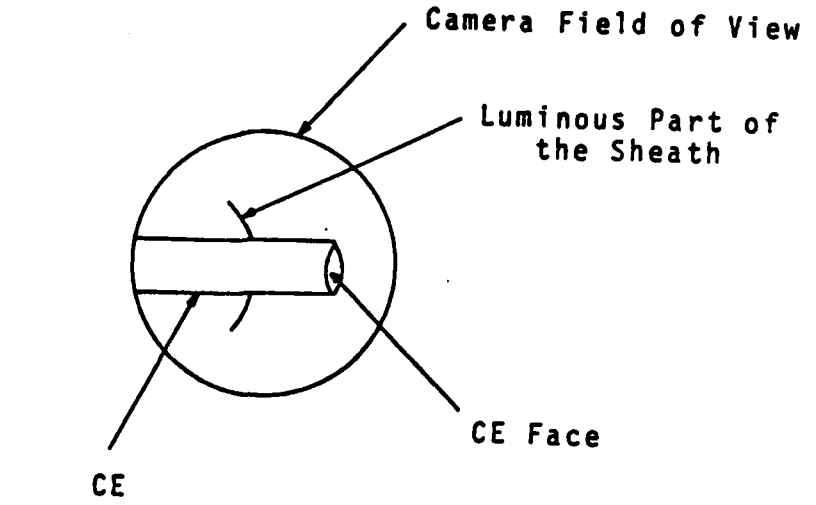


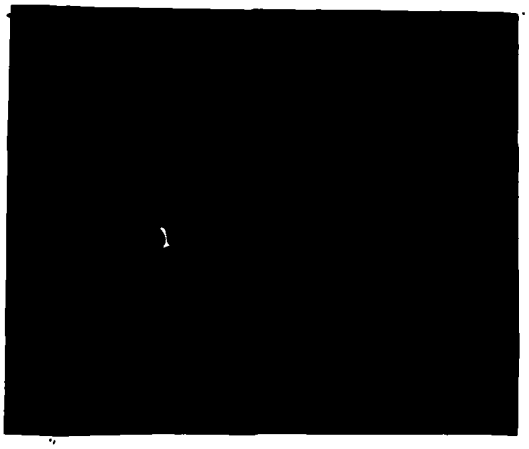

Figure 47. ns Exposure Photograph of 1 T $H_2$, 5% A, 80 kV Sheath.

The emission from the end of the CE is most prominent. Also visible in Figure 48 are several faint rings along the CE. This suggests that sheath electrons attain significant energies during rundown. In static gas discharges electrons usually suffer such frequent collisions that they reach the anode with energies much too low for x-ray production much above 100 eV. During DPF rundown, however, the induced electric field, d/dt (IL), dominates the electrostatic field (IR is negligible). That field may be large enough to produce electrons in the several kiloelectronvolt range near the CE by high field acceleration from the time of electron final collisions before striking the CE. This field is larger for small diameter CEs. The spacing of the rings suggests radial oscillation of the accelerating electric field, possibly due to sheath instability.

Figure 49 was obtained with the smallest pinhole, permitting excellent spatial resolution at the cost of image brightness. The focus is visible here as a thin, faint line. The thinness may be due to a small focus, perhaps a consequence of reduced sheath thickness during sheath formation and rundown. The relative dimness of the pinch compared to the brightness near the CE face suggests that the focus is not as good as it could be, probably a result of poor compression dynamics due to the use of a small diameter CE. Similar pictures taken with conventional devices often show a very large, plumelike focus, comparable in brightness to the region near the CE face.

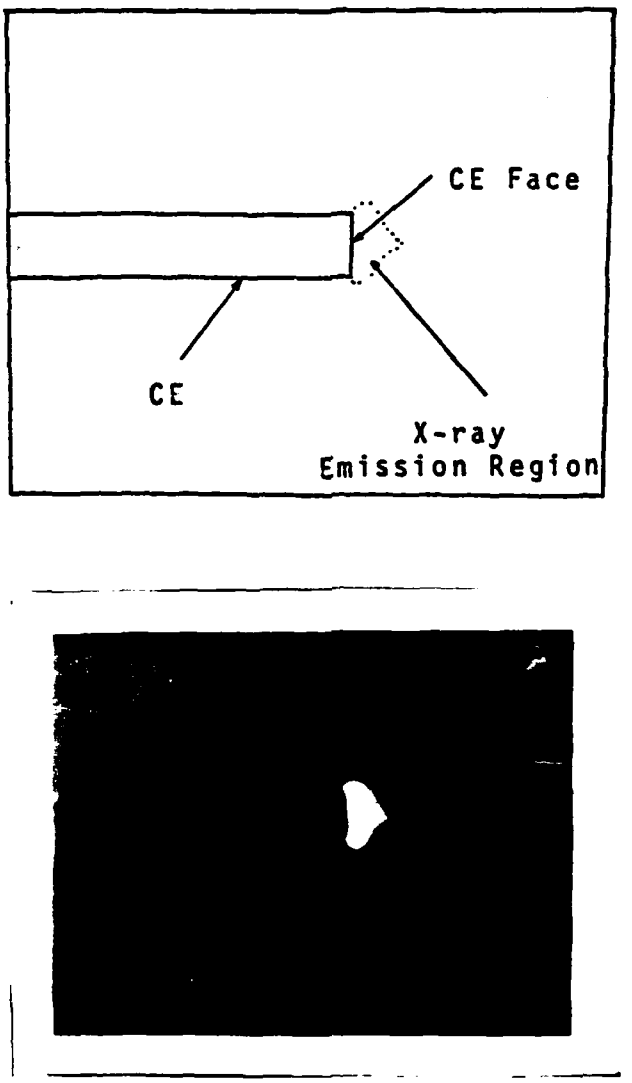


Figure 48. Typical X-ray Pinhole Photo of Pinch Region.

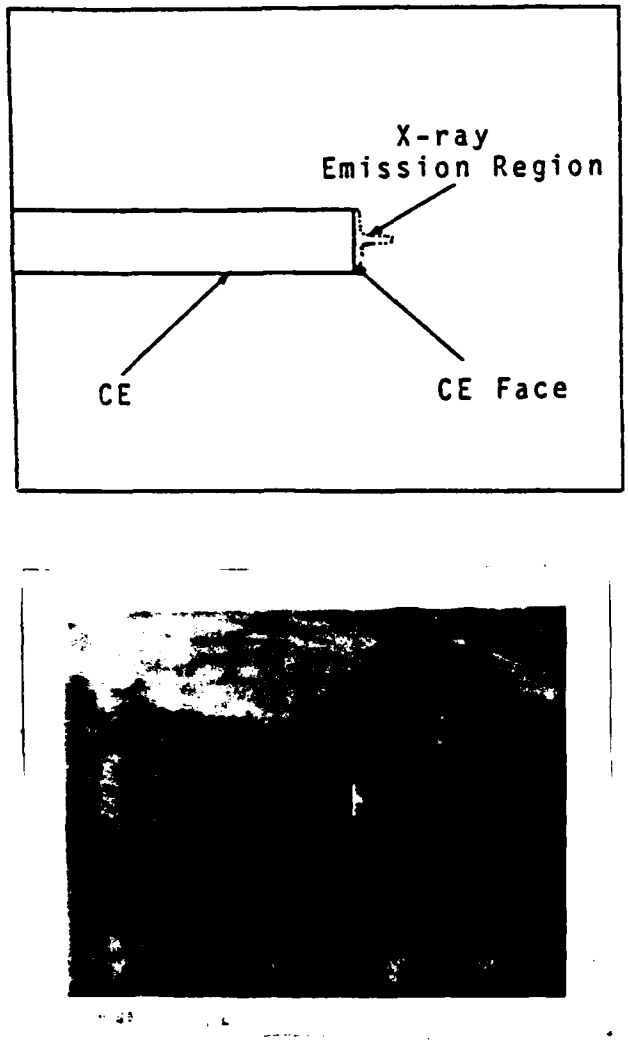


Figure 49. High Spatial Resolution X-ray Pinhole Photo.

## 4. CONCLUSIONS

The UNM HVDPF experiment incorporates several unusual features, including (1) high voltage operation, (2) short rundown length, (3) small CE diameter, and (4) single switch operation.

### High Voltage Operation

It has been verified that plasma focus devices will operate properly (with typical V, $\dot{I}$ and X spikes) at higher voltages with improved current efficiency, though the neutron yield of this device has yet to be measured. Based on experience, it is not generally recommended that plasma focus investigators pursue high voltage operation for current efficiency benefits alone. Devices of comparable current can be built far more simply and inexpensively, two of the many virtues of the plasma focus. And, as previously mentioned, higher energy banks require much higher operating voltages to achieve these current efficiency benefits. But in addition to proving current efficiency at the present operating voltages, other interesting questions associated with high voltage operation have been explored, such as sheath structure and short rundown behavior.

For lower voltage plasma focus devices, sheath rundown starts at about 1 $\mu$s. If this were true for higher voltage devices, the sheath would not run down and focus in the sh t $\tau/4$ of higher voltage devices. This was initially a concern for this device. It was believed that the high $\dot{I}_0$ of higher voltage devices and the possibility of increased sheath formation energy, would permit a sheath to be formed and have it run down and focus in the time required by lower voltage devices for just lift off and inverse pinch phases. This was based on the findings in Reference 55.

This question was favorably resolved. This device does focus, though with less regularity than lower voltage devices. A determination as to why focussing is not more reliable has yet to be made. There may be several possible reasons.

First, it is possible that for the geometry and gas pressures and mixes that have been operated thus far, the voltage is too low for reliable focussing. At lower voltages (50 to 70 kV), a tendency for multiple (2-3) sheath formation has been observed, as indicated by multiple voltage spikes corresponding, presumably, to multiple pinches. This behavior goes away as voltage is increased, with rare multiple sheath formation at 80 kV. Multiple sheath formation is believed to be due to a combination of prefill gas pressure and mix and insufficient bank energy at lower voltages. If bank energy is too low, there is not enough energy to create a single high quality sheath. Such a sheath may be a poor snowplow which leaves enough gas behind it in the vicinity of the insulator for subsequent sheaths to form. Also at higher pressures it is believed that a sheath may peel off from the bulk of the gas near the insulator, permitting the development of subsequent sheaths from the gas remaining in this region.*

A more likely cause of unreliable focussing is insufficient cleanliness of vacuum vessel and electrode surfaces and possibly a vacuum system that is not leak tight. This conclusion is reached because focussing can be accomplished on a 50 percent basis for 6 to 10 shots per gas fill after 5 to 20 warm-up shots. It is believed that the main function of warm-up shots, which include evacuating and refilling the discharge vessel every 3 to 5 shots, is to evolve and remove contaminants from improperly cleaned surfaces. After several repetitions of this procedure, the system appears clean enough to assure 50 percent focussing.

It is somewhat common in plasma physics experiments to clean plasma containment vessels with inert gas glow discharges. This is sometimes referred to as atomic cleaning. In this process, ions, such as Argon ions, dislodge surface impurities by impacting surfaces with the (relatively) high energies acquired in the glow discharge field. It has been found that Argon atomic cleaning of a DPF resulted in very high first shot neutron yields.* This was done with no warm-up shots,

*Mather, J. W., Private communication.

an unheard-of event. At some point it might be worthwhile to consider glow discharge cleaning of this apparatus as routine procedure to save the time and expense of many warm-up shots.

Another possible way to increase the focussing percentage may be to improve the power flow situation. It is clear from the geometry of the switch header and the cable distribution that power is not distributed as uniformly as possible. It is common in DPF experiments to mix up cable feeds from various banks or capacitors to the load. This has not been done as yet because it would require longer cables (thereby increasing system inductance) and a significant effort of manual labor. Another possible solution to the power flow problem is to use two of the present switches, side by side, or a different switch, either a longer one to reduce the fan problem or possibly one consisting of two concentric rails, thus more closely conforming to the circular feed at the gun header.

It is uncertain if the rail-gap switch is functioning properly. The Micro-Marx is barely adequate as a trigger pulse source when its output cable is terminated, without a peaking gap. It would be preferable to replace it with one of Maxwell's planar triode trigger units. A sure test of rail-gap multichanneling is a streak camera record of firing. The total system inductance, as measured in (40- and 50-kV) short-circuit tests, gives some indication that proper multichanneling is not occurring. For total system inductance, 135 nH has been measured instead of the calculated 100 nH. However, error in the calculation of the inductance of other system components is also possible. If, in fact, the rail-gap is firing with very few channels, this would constitute a power flow problem. It could result in current asymmetry at the gun header, which might lead to the formation of bad sheaths.

Despite only 50 percent focussing, when focuses occur, they are fairly reproducible. How good a focus is forming remains a matter of conjecture. Rough estimates of x-ray yield and temperature are available indicating that a fairly high temperature, high density pinch plasma is obtained, suitable for significant thermonuclear neutron yields. However, experimental demonstration of fusion neutron yield

requires prefilling with deuterium. This has not been done because of the safety hazard involved. Neutron yields of the order of $10^9$ at 2.5 MeV are expected. This sort of flux can be a biological hazard if proper neutron attenuation precautions are not taken.

Short Rundown

Concurrent with the fear that a fast bank might not allow sufficient time for sheath formation and lift-off is the fear that a sheath required to run down and focus in less than a microsecond might not have time to stabilize. This means that time is needed to develop a uniform, azimuthally symmetric sheath suitable for good focus. But by the same argument, such a sheath might not have time to develop hydromagnetic instabilities. Analysis of this sort of problem is complex. Conventional plasma focus devices have been around for 20 years or so and a great deal of analysis and measurement has been performed on them. For such devices, sheath temperatures, densities and thicknesses have been measured and calculated both analytically and computationally. Stability analysis of, for example, thermal equilibration times between various species, can be estimated with some degree of confidence. In the case of higher voltage plasma focus sheaths, we have only a few pieces of data and the present work. It cannot be determined with confidence that stability criteria or thermal equilibration times in order to assert that the higher voltage sheath does require more rundown time to stablize or that a longer rundown would permit instabilities time to develop.

The situation is less nebulous in considering the collapse process. As noted in Reference 56 (using the Spitzer equilibration time, even for lower voltage devices) the pinch temperatures and densities are such that equilibration times are longer than observed pinch times. This provides some basis for the temporal fluctuations of pinch electron temperatures which are inferred from time-resolved pinch x-ray measurements. It is possible with temperature and density measurements of high voltage plasma focus pinches and image converter records of pinch lifetime to perform similar analysis for higher voltage plasma focus devices.

Small CE Diameter

The present CE diameter of 1/2-in is the smallest CE diameter used in any plasma focus. It appears that only Sandia National Laboratories (SNL) and UNM use such small diameter CEs based on CE diameter cited in the open literature.

These small diameter CEs were originally used by SNL in magnetic reconnection experiments which sought to enhance neutron yield by beam-target processes of reconnection-produced electric fields. In those experiments two or more DPFs were operated simultaneously within a common discharge vessel. Adjacent sheaths were allowed to collide and rearrange themselves to increase system mutual inductance. To enhance this process, it was desired to store as much magnetic energy as possible behind each sheath before reconnection; therefore, individual gun inductance was increased with small CE diameter. The initial funding for the UNM HVDPF was from SNL. It was hoped that neutron yield could be further enhanced by high-voltage current optimization. Thus, the small CE diameter was inherited with its various pros and cons, including the large $\dot{L}$ load during rundown and increased magnetic energy storage behind the sheath.

A related set of measurements were used for experimental and computational investigations varying CE diameter for high voltage plasma focuses. It was found that the smallest CE diameter tested (1-in) gave the highest neutron yield, whereas larger diameter CEs gave no yield at all, in some instances (Ref. 11).

Reference 11 gave the opinion that radial collapse from too large a CE diameter would expend too much of the short $\tau/4$ typical of higher voltage plasma focuses. Another opinion is that during collapse the sheath requires time for thermal equilibration and that too short a collapse will not impart enough kinetic energy to the imploding sheath to lead to the high temperatures required of fusion.* It is also believed that too small a CE may not lead to the classical geometry of the focus. Rather, the sheath will simply drop off the end of the CE

*Ibid.

without sufficient momentum to form the bulged, umbrella shape required for the z-pinch to occur.

There is another aspect of using a small CE diameter: the magnitudes of current densities and magnetic fields are greater at small CE diameters. (This is true only if current and sheath thickness remain constant as CE diameter is changed. This is not necessarily so in general but a more careful analysis may not be required. Note two experimentally observed effects on this device which result from high current density and high magnetic field at the CE surface. Because others have not noted these effects on devices of similar current but larger CE diameter, it is suspected that smaller CE diameter does produce larger current densities and magnetic fields at the CE surface for comparable device currents, and that sheath thickness is of secondary importance in these effects.) Increased current densities and magnetic fields will decrease lift-off times. However, experience has shown that current densities are too high before lift-off as indicated by a shiny copper ring and indentation on the CE at the point where the insulator ends (and breakdown occurs). This damage is shown in Figure 50. This means significant vaporization of the CE occurs in this region. Aside from eroding the CE, this effect may degrade or halt plasma focus operation. The evaporated copper may condense on the insulator, causing breakdown to occur along a single, mainly axial path, thereby, thwarting the preferred condition of azimuthally-symmetric breakdown and sheath formation. Evidence of this has been seen. In some cases the insulator is permanently damaged by a current path that has melted the insulator to such a depth that the path cannot be removed by bead-blasting. Probably breakdown occurs along this melted path, spoiling azimuthal symmetry as the sheath is formed. In these cases no focussing occurs at all and the gun header voltage waveform indicates that the sheath, if it is formed at all, fails to lift off the insulator.

Damage to the CE, due to small diameter and presumably high voltage operation as well, also results from the pinch itself. At 70 to 80 kV, small radius was noted, ~ 0.5-1.0 mm deep, ~ 2 mm, hole erosion

(a) Damage due to High Breakdown Current Densities.

(b) Tip Showing Flaring due to Pinch Impulse Forces.

Figure 50. Photographs of CE.

in the face of the CE. Such CE erosion is common in DPFs and results from electron beam bombardment, plasma electrode vaporization, impulsive magnetic pressure and axial gas jetting--toothpaste squeezing--from the pinch region. Small radius, deep erosion was not observed by SNL using similar electrodes operating DPFs at comparable currents and lower voltages, ~ 30 kV. The erosion seen there was more broad and shallow. This suggests that the thinner sheath of the HVDPF is responsible.

In addition, the HVDPF CE tip soon becomes radially flared, as shown in Figure 50b. This effect is also not evident in the SNL guns. This flaring is presumably also due to more energetic, more concentrated impulsive forces acting on the CE face. It is believed that this flaring is ultimately bad for subsequent focus formation because it is a surface discontinuity, a sharp bump, which the sheath encounters just before collapse.

A final effect of small CE diameter is that mentioned previously, dealing with snowplow theory. For small CE diameter, due to the (postulated) increased magnetic fields and current densities near the CE, the sheath will more resemble a bullet shape than a planar piston. This has been suggested by the fast-frame rundown photograph. Also, the increase of L over that calculated from geometry and the suggestion of sheath acceleration near the end of rundown indicate enhanced magnetic field and current density.

Single Switch Operation

As mentioned, proper sheath formation requires simultaneous application of current to the plasma focus within ~ 10 ns. This number was arrived at by investigators using several switches to transfer energy from capacitors to the DPF, and reflects the problems they had in obtaining good switch simultaneity (Ref. 7). At first glance it might seem that using a single switch, would avoid this difficulty. But the same problem exists in essence because the rail-gap switch is actually many switches--many plasma channels--contained in the same envelope. To achieve multichanneling a high amplitude, fast-rising

trigger pulse must be applied, the same remedy for achieving good simultaneity with several switches in separate envelopes.

The use of a centrally-located single switch does simplify maintenance problems, but open exposure also creates EM noise problems. Where investigators have used multiple switches, often the switches are contained within capacitor housings or capacitor module housings so that they are electromagnetically shielded to some degree. In view of the persistent noise problems experienced, the idea of shielded switches is appealing.

## Appendix A

### Gas Breakdown

Electron avalanching is referred to as the primary process in gas breakdown. It is usually required to initiate breakdown, but one of two secondary processes completes it. Secondary processes are (1) secondary avalanching and (2) streamers. A planar geometry with an electrode spacing of d is assumed, as follows.

The electron drift velocity in an avalanche is typically 100 times greater than the ion drift velocity. In most cases the ions can be considered stationary during avalanche and for some time thereafter. Also, as avalanche electrons are accelerated along the applied field lines, they collide with neutrals and gain transverse momenta which spread them perpendicular to the applied field lines. The result is a charge distribution such as shown in Figures A-1a and 1b.

The number of electrons in a primary avalanche due to one electron starting at the cathode is $e^{\alpha x}$, where x is the distance from the cathode and $\alpha$ is the first Townscend coefficient, the mean number of ionizing collisions per centimeter for one electron: $\alpha \sim 1/\lambda_e$. A single avalanche is usually not enough to cause breakdown, but it can produce secondary avalanches which may.

A primary avalanche produces secondary avalanches by three main processes in which additional electrons are produced at the cathode. These processes are: (1) primary avalanche positive ions strike the cathode, ejecting electrons from the cathode, (2) de-excitation of molecules in the avalanche produces photons which release cathode photoelectrons, and (3) metastable (excited) molecules from the primary avalanche thermally diffuse back to the cathode and emit electrons on striking the cathode. An avalanche breakdown will consist of a cluster of secondary avalanches, as shown in Figure A-1c, centered near the primary avalanche.

For a primary avalanche with one generation of secondary processes, the total number of electrons produced by one electron starting

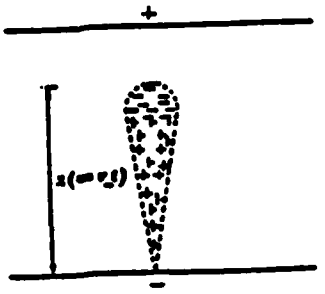

(a.) Distribution of Carriers in Avalanche

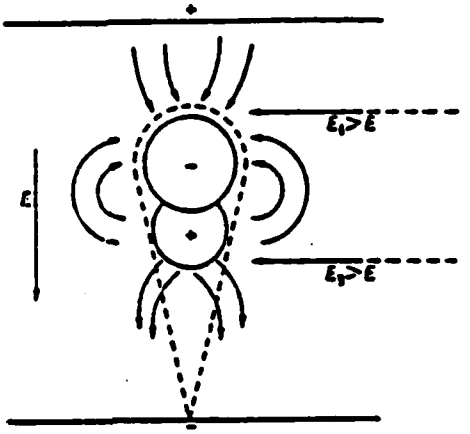


( b.) Effect of Space Charge Produced by an Avalanche on the Applied Electric Field

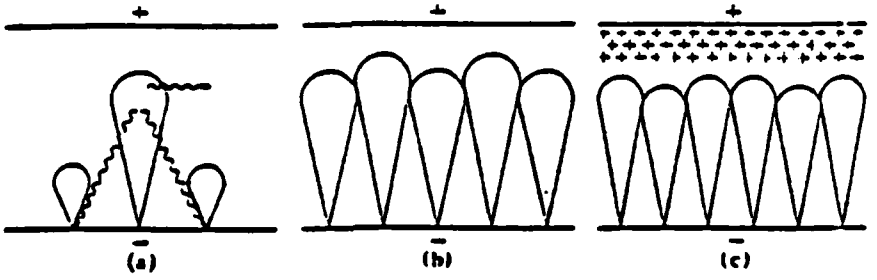


(c.) Townsend Mechanism-breakdown by Series of Avalanches.

Figure A-1. Evolution of Breakdown by Townsend Avalanche. (After Reference 31)

at the cathode and avalanching across the gap is $\gamma e^{\alpha d}$ where $\gamma$ is the second Townscend avalanche coefficient, the number of electrons produced by one electron through secondary avalanche processes. The criterion for a self-sustaining avalanche breakdown is thus

$$1 = \gamma e^{\alpha d} \qquad \text{(A-1)}$$

The breakdown voltage can be established for this process for given gap spacing and values of $\alpha$ and $\gamma$ which depend on gas type, pressure and temperature.

As mentioned, in addition to avalanche breakdown, breakdown may occur by the streamer process. There are two kinds of streamers: anode-directed and cathode-directed. In both types, photoionization and space-charge ionization are essential. The anode-directed streamer develops directly from an electron avalanche and proceeds much more rapidly than an electron avalanche. The cathode-directed streamer forms after an electron avalanche has reached the anode, and proceeds at roughly the speed of an electron avalanche. A discharge channel may result from a single avalanche developing into both an anode-directed streamer and a cathode-directed streamer which together close the gap.

The anode-directed streamer occurs when the electron space charge at the head of an avalanche is large enough to produce an electric field comparable to or larger than the field initially applied to the gap. Figure A-2b depicts the development of an anode-directed streamer. Subsidiary avalanches form in front of the primary avalanche where the electron space charge field is strongest and enhances the applied field. The subsidiary avalanches are initiated by photoionization in the gas from radiation produced in the primary avalanche. The negative head of the primary avalanche is attracted to the positive tails of the subsidiary avalanches, creating a plasma of width greater than that of the original negative head of the primary avalanche. At the same time the negative heads of the subsidiary avalanches collectively form an even larger negative streamer head, and

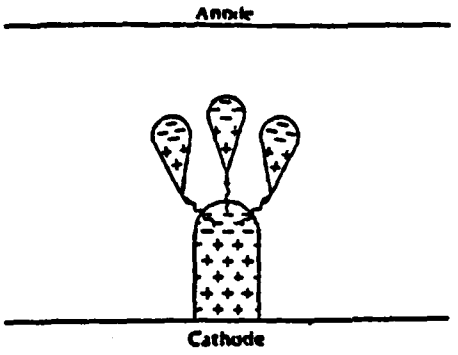


(2a.) Propagation of Anode-Directed Streamer.

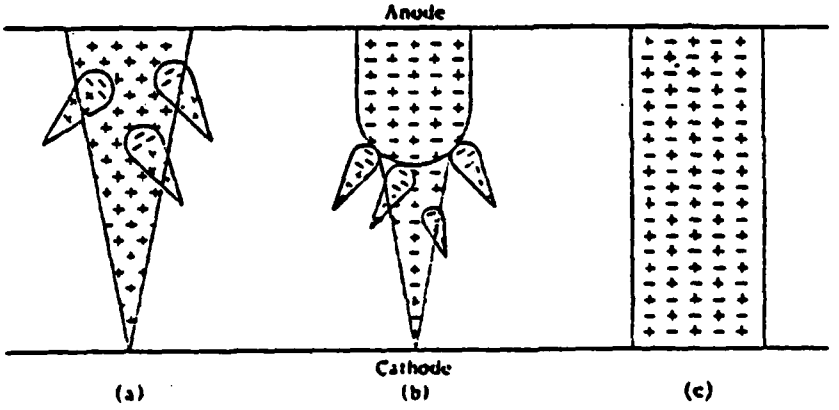


(2b.) Propagation of Cathode-Directed Streamer.

Figure A-2. Propagation of Streamer.

the process continues. Streamer propagation is enhanced by photoionization and the large electric fields of the streamer electron space charge head. When the streamer reaches the anode, it leaves behind it a quasi-neutral conducting plasma channel.

The cathode-directed streamer begins after an ordinary avalanche has crossed the gap and all electrons from the avalanche have entered the anode, leaving a cone of positive ions, a positive avalanche stem. When positive space charge at the top of the stem (near the anode) creates an electric field comparable to or greater than the applied field, subsidiary avalanches initiated by avalanche stem photoionization form, initially at the anode, where the space-charge field is largest. They will be formed preferentially along the stem axis where the space charge field most strongly enhances the applied field. As the negative heads of the subsidiary avalanches neutralize the high positive space charge near the anode, subsidiary avalanches form closer and closer to the bottom of the stem, propagating towards the cathode. When all the positive space charge of the original stem is neutralized, the streamer will have closed the gap, leaving a conducting plasma column in its wake. Figure A-2b depicts the development of a cathode-directed streamer.

A typical Paschen curve is shown in Figure A-3 for planar geometry, where d is the separation between the plane electrodes. Such a curve is modified for nonplanar geometry, which also exhibits polarity effects, and for gas temperature and type. Electrode type and surface preparation also have effect. The region to the right of the Paschen minimum is where spark gaps usually operate. Higher gap hold-off voltages are obtained by increasing gas pressure.

## Appendix B

### Shock Theory of the Sheath

Shock waves are classified according to their pre- and post-shock electrical conductivity, $\sigma_1$ and $\sigma_2$, respectively. Three situations are defined.

$\sigma_1 = \sigma_2 = 0$ fluid dynamic shocks

$\sigma_1, \sigma_2 > 0$ plasma (or MHD) shocks

$\sigma_1 = 0, \sigma_2 > 0$ ionizing shocks

As indicated in earlier consideration of the validity of snowplow assumptions, the sheath effectively ionizes gas in its path; the temptation is to treat the sheath as an ionizing shock. However, experimental results indicate that the fill gas is ionized long before the sheath reaches it. A possible explanation for this is photopreionization of the fill gas.

To consider the importance of photoionization, a rough estimate of the sheath Bremsstrahlung radiation during rundown is made. Blackbody radiation is negligible because of the large plasma required for radiative thermodynamic equilibrium at typical sheath densities and temperatures. Reference 45 gives the following equation for Bremsstrahlung radiation power density of a hydrogenic plasma:

$$u_b = 5.35 \times 10^{-24}\ n^2\ T^{1/2} \quad \text{erg/cm}^3\text{-s} \qquad \text{(II-1)}$$

where T is in keV and n is particle number density in particles/$cm^3$.

For density and temperature, we use typical sheath values of $n = 10^{17}\ cm^{-3}$ and T = 30 eV. We then obtain

$$u_b \sim 10^{10}\ \frac{\text{erg}}{\text{cm}^3\text{-s}}$$

Assuming sheath thickness of 1 cm, and area of 100 $cm^2$, the radiated power is $P_b \sim 10^{12}$ erg/s.

For 1 $\mu$s rundown, the total radiated energy is $E_b = 10^6$ erg = 0.1 J. This is a very small fraction of the energy required to ionize the gas that the snowplow will later sweep up. Thus most of the ionization is due not to photoionization, but to shock heating. However, to consider whether plasma shock or ionizing shock theory is appropriate, an upper limit estimate of $\sigma$ due to photoionization is made.

## REFERENCES


1. Mather, J. W., "Formation of a High-Density Deuterium-Plasma Focus in a Coaxial-Gun Device," Bull. APS, 9, 339 (1964)).

2. Mather, J. W., "Investigation of the High-Energy Acceleration Mode in the Coaxial Gun," Phys. Fluids Supplement, 7, S28 (1964).

3. Mather, J. W., "Observations on the Modes of Acceleration in a Coaxial Gun, Bull APS, 8, 177 (1963).

4. Filippov, N. V.,"Plasma Focus Research at the Kurchatov Institute of Atomic Energy. Review of the Main Experiments," p. 1, Proceedings of the Second International Workshop on Plasma Focus, Tenth European Conference on Controlled Fusion and Plasma Physics, Moscow, September 1981.

5. Gourlan, C., et al, "Recent Progress in 1-MJ Plasma Focus Dynamics and Scaling for Neutron Production," p. 123, IAEA-CN-37/U-3-1.

6. Bostick, W. H., V. Nardi, W. Prior, C. Cortese, "Pulsed Radiation from Focused Plasmas," Proc. 3rd Topical Conference on Pulsed High $\beta$ Plasma, edited by D. E.Evans, 1976.

7. Mather, J. W., "Dense Plasma Focus,"Chpt. 15 in Methods of Experimental Physics, Academic Press, New York, London, Vol. 9B, 187 (1971).

8. Peacock, N. J., X-Ray and Neutron Production Optimization in the Dense Plasma Focus, AFWL-TR-73-47, Air Force Weapons Laboratory, Kirtland AFB, NM, 1973.

9. Rhee, M. J., R. F. Schneider, "Compact Pulsed Accelerator," 1983 Particle Accelerator Conference.

10. Schoenbach, K. H., et al., "Opening Switches," Proceedings of 3rd International Pulsed Power Conference, Albuquerque, New Mexico, 1981, p. 74.

11. Decker, G., et al, "Current and Neutron Yield Scaling of Fast High Voltage Plasma Focus," Plasma Phys., 22, 245 (1980).

12. Decker, G., W. Kies, G. Pross, "The First and the Final Fifty Nanoseconds of a Fast Focus Discharge,"Phys. Fluids, 26, 571 (1983).

13. Decker, G., W. Kies, W. Maysenholder, G. Pross, "Fast 200 kV Capacitor Bank as a Current Source for a Dense Plasma Focus," IEEE Pulse Power Conf., Albuquerque, 1981, p. 392.

14. Decker, G., W. Kies, G. Pross, "SPEED 1: A High Impedance, High Voltage Driven Fast Plasma Focus of Improved Performance," Institute I of Physics, University of Dusseldorf.

15. Decker, G., W. Kies, G. Pross, J.Rybach, "Pinch Dynamics vs. Driver Characteristics. Plasma Focus SPEED 1," Institute I of Physics, University of Dusseldorf.

16. Decker, G., et al, "Dynamics of 120 and 20 kV Plasma Focus Devices with Respect to Density and Current Distribution and Neutron and X-Ray Emission," IAEA Berchtesgaden 1976.

17. Decker, G., et al, "Dynamics of 120 and 20 kV Focus Devices with Respect to Density and Current Distribution and Neutron and X-Ray Emission," IAEA-CN-35/E18-1.

18. Garwin, R., A. Rosenbluth, M.Rosenbluth, Infinite Conductivity Theory of the Pinch, LA-1850, Los Alamos National Laboratory, Los Alamos, New Mexico, 1954.

19. Bernard, A., et al, "Structure of Current Sheath and Fast-Particle Beams in the Focus Experiment," Plasma Phys. and Con. Fus. Res., IAEA Berchtesgaden, 1976.

20. Newman, C. E., V. Petrosian, "Production of Hard X-Rays in a Plasma Plasma Focus," Phys. Fluids, 18, 547 (1975).

21. Hayd, A., H. J. Kaeppeler, M. Maurer, P. Meinke, "The Calculation of Turbulence Phenomena in Plasma Focus Dynamics Using REDUCE," Stuttgart Report IPF-82-7, May 1982.

22. Baker, D., Unpublished work, Los Alamos Scientific Laboratory, Los Alamos, New Mexico, 1967.

23. Anderson, O. A., et al, "Neutron Production in Linear Deuterium Pinches," Phys. Rev., 109, 612 (1958).

24. Anderson, O. A., et al, "Neutron Production in Linear Deuterium Pinches," Phys. Rev., 110, 1375 (1958).

25. Burkhardt, L. C., et al, "Pinch Effect," J. Appl. Phys, 28, 519 (1957).

26. Luntz, J.D., "From Perhapsatron to Columbus," Nucleonics, December 1955, p. 23.

27. "Thermonuclear Power...The Search for Ideas," Nulcleonics, February 1956, p. 42.

28. Bennett, W. H., "Magnetically Self-Focussing Streams," Phys. Rev., 45, 890 (1934).

29. Ware, A. A., "A Study of a High-Current Toroidal Ring Discharge," Phil. Trans. Roy. Soc. a, 243, 197 (1951).

30. Post, R. F., "Controlled Fusion Research--an Application of the Physics of High Temperature Plasmas," Rev. Mod. Phys., 28, 338 (1956).

31. High Voltage Technology, L. L. Alston, ed., Oxford University Press, 1968.

32. Vanyukov, M. P., E. V. Daniel, "Spark Discharge over the Surface of Films of Different Composition," Sov. Phys.--Tech. Phys. 12, 1416 (1968).

33. Beverly, R. E., III, "Channel Spreading and Substrate Vaporization in Surface-Spark Discharges," J. Appl. Phys., 48, 3609 (1977).

34. Beverly, R. E., III, R. H. Barnes, C. E. Moeller, M. C. Wang, "Ultraviolet Sectral Efficiencies of Surface-Spark Discharges with Emphasis on the Iodine Photodissociation Laser Pumpband," Appl. Optics, 16, 1572 (1977).

35. Gourlan, C., H. Kroegler, C. Maisonnier, J. P. Rager, B. V. Robouch, A. Gentilini, "Recent Progress in 1-MJ Plasma Focus Dynamics and Scaling for Neutron Production," Plasma Phys. and Con. Fus. Res., 1978.

36. Rohwein, G. J.,"An Improved Surface Discharge Air-Gap Switch," SCL-DR-710050, Sandia National Laboratories, Albuquerque, New Mexico, Nov. 1971, p. 39, p. 41.

37. Mawardi, O. K., "Bounded Current Sheets,' Phys. Fluids Supplement, 7, S9 (1964).

38. Basque, G., A. Jolas, J. P. Watteau, "Comparison of a Two-Dimensional Snowplow Model with Experiment," Phys. Fluids, 11, 1384 (1968).

39. Vargas, M., F. Gratton, J. Gratton, H. Bruzzone, H. Kelly, "Experimental Verification of a Theory of the Current Sheath in the Plasma Focus," Plasma Phys. and Con. Fus. Res., IAEA Berchtesgaden, 1976.

40. Herziger, G., H. Krompholz, W. Schneider, K. Schonbach, "A Steady-State Fluid Model of the Coaxial Plasma Gun," Phys. Lett., 71A, 54 (1979).

41. Butler, T. D., I. Henins, F. C. Jahoda, J. Marshall, R. L. Morse, "Coaxial Snowplow Discharge," Phys. Fluids, 12, 1904 (1969).

42. Potter, D. E., "Numerical Studies of the Plasma Focus," Phys. Fluids, 14, 1911 (1971).

43. Eltgroth, P. G., "Comparison of Plasma Focus Calculations," Phys. Fluids, 25, 2408 (1982).

44. Beckner, E. H., "Production and Diagnostic Measurements of Kilovolt High-Density Deuterium, Helium, and Neon Plasmas" J. Appl. Phys., 37, 4944 (1966).

45. Krall, N. A. and A. W. Trivelpiece, Principles of Plasma Physics, McGraw-Hill, 1973.

46. Fischer, H. and K. H. Haering, "Plasma Development in the Accelerator of a 2-kj Focus Discharge: Addendum," Applied Optics, 18, 3733.

47. Bertalot, L., et al, "Experiments on Plasma Focus Dynamics, Neutron Production and Ion Emission," 8th Int. Conf. on Plas. Phys. Letts, 79A, 389 (1980).

48. Herold, H., et al, "Investigation of the Neutron Production Phases of a Large Plasma Focus Device," 9th Int. Conf. on Plasma Phys. and Con. Nuc. Fus. Res., Baltimore, 1982, IAEA-CN-41/N-6-1.

49. Bernard, A., J. P. Garconnet, A. Jolas, J. P. le Breton, J. de Mascureau, "Turbulence Caused by the Interaction between Plasma and Electric Current in the Focus Experiment," Plasma Phys. and Con. Fus. Res., 1978.

50. Beckner, E. H., E. J. Clothiaux, D. R. Smith, "Dominant Source of Soft X-Radiation from Coaxial Discharge Tubes," Phys. Fluids, 12, 253 (1969).

51. Bernard, A., et al, "The Dense Plasma Focus--A High Intensity Neutron Source," Nucl. Inst. and Methods, 145, 191 (1977).

52. Robinson, J. W., "Self-Crowbarring, Load-isolating Triggered Spark Gap," Rev. Sci. Instrum., 51, 1532 (1980).

53. Nunnally, W. C., Simple, 200-kV, 10-ns Risetime Pulse Generator, LA-UR-78-2150, Los Alamos National Laboratory, Los Alamos, N Mex, 1978.

54. Lee, J. H., D. S. Loebbaka, C. E. Roos, "Hard X-Ray Spectrum of a Plasma Focus,"Plasma Phys. 13, 347 (1971).

55. Decker, G., H. Herold, H. J. Kaeppler, W. Kies, W. Maysenholder, B. Nahrath, T. Oppenlander, G. Pross, B. Ruckle, A. Sauserbrunn, P. Schilling, H. Schmidt, M. Shakhatre, M. Trunk, "Neutron Emission Parameters in Plasma Focus Devices," Plasma Phys. and Con. Fus. Res., 1978.

56. Mather, J. W., "Formation of a High-Density Deuterium Plasma Focus," Phys. Fluids, 8, 366 (1965).

## Glossary

Collapse--After the sheath reaches the end of the accelerator center electrode, it changes from nearly constant velocity and profile to a shape conducive to radial collapse very similar to that of the conventional z-pinch. Collapse is sometimes referred to as compression.

Focus--The z-pinch formed in a coaxial plasma accelerator after the sheath runs to the end of the accelerator center electrode. Focus is the final phase of collapse.

Lift-off--The time when the sheath formed on the plasma focus insulator after breakdown begins to move away from the insulator due to current in the sheath interacting with the magnetic field created by that current.

Quarter-Period--One fourth the capacitor bank resonant period. In an LC circuit current is a maximum at the quarter-period. Most plasma focus yields scale with current so that the focus is usually timed to occur at the quarter-period.

Restrike--The occurrence of a second breakdown within the coaxial plasma accelerator before the sheath formed by the initial breakdown has a chance to focus. Restrike impairs or prevents focus.

Rundown--The period of time between lift-off and collapse when the sheath has a nearly constant velocity and very low resistance. During rundown the coaxial accelerator is electrically a nearly constant load whose impedance is given by the time rate of change of accelerator inductance. This rate is determined almost entirely by sheath velocity and the ratio of outer to inner electrode diameters.

Sheath--A localized region of relatively high density, high temperature, high conductivity plasma in which current flows between the electrodes of the coaxial plasma accelerator. In normal operation the sheath has good symmetry about the accelerator axis.

Z-pinch--A cylindrical ($r,\theta,z$) plasma configuration in which current flows in the axial ($z$) direction with no azimuthal ($\theta$) variation. The resulting azimuthal magnetic field interacts with the axial current to radially constrict (pinch) the plasma column.

END

FILMED

3 -86

DTIC